Reaction Path Search and Kinetic Analysis for Chemical Reactions Including Dynamical Bifurcations

（動的経路分岐を含む化学反応に対する反応経路探索と速度論解析）

Takuma Ito

Graduate School of Chemical Sciences and Engineering
Hokkaido University

March 2024

Contents

1. General Introduction

1.1 Theoretical analysis of chemical reactions

1.1.1 Schrödinger equation

Chemical reactions are ubiquitous in our surroundings, such as combustion, biological phenomena, and so on. Chemical reactions are phenomena where one or more chemical substances are transformed into others (1). Understanding and controlling chemical reactions are important to design new chemical reactions for drug discovery and the development of functional materials. Reaction mechanisms were conventionally elucidated by experimental studies. In recent years, the importance of theoretical calculations has increased, since they can deal with the microscopic motions of atoms (2-5).

In quantum mechanics, chemical reactions are described as the motion of nuclei and electrons governed by the following Schrödinger equation shown in **Equation (1.1)** and **(1.2)** (6,7)

$$i\hbar\frac{\partial}{\partial t}\Psi(\mathbf{r},\mathbf{R},t) = \hat{H}\Psi(\mathbf{r},\mathbf{R},t) \tag{1.1}$$

$$\hat{H} = -\sum_{i=1}^{n}\frac{1}{2}\nabla_i^2 - \sum_{I=1}^{N}\frac{1}{2M_I}\nabla_I^2 - \sum_{i=1}^{n}\sum_{I=1}^{N}\frac{Z_I}{r_{iI}} + \sum_{i=1}^{n}\sum_{j>i}^{n}\frac{1}{r_{ij}} + \sum_{I=1}^{N}\sum_{J>I}^{N}\frac{Z_I Z_J}{r_{IJ}}. \tag{1.2}$$

In the equations, $\hbar$ is Planck constant and equal to 1 in atomic unit. t is time. n and N are the number of electrons and the number of nuclei. i and j are the indices of electrons, and I and J are indices of nucleus, respectively. Z_I and Z_J are atomic number of I-th and J-th nuclei, respectively. r_{ij}, r_{iI}, and

r_{IJ} represent the distances between the i-th electron and j-th electron, that between the i-th electron and I-th nuclei, and that between the I-th nuclei and J-th nuclei, respectively. $\mathbf{r} = (x_1, y_1, z_1, \cdots, x_n, y_n, z_n)^{\mathrm{T}}$ and $\mathbf{R} = (\mathrm{X}_1, \mathrm{Y}_1, \mathrm{Z}_1, \cdots, \mathrm{X}_\mathrm{N}, \mathrm{Y}_\mathrm{N}, \mathrm{Z}_\mathrm{N})^{\mathrm{T}}$ are the positions of the electrons and nucleus, respectively. $\Psi(\mathbf{r}, \mathbf{R}, t)$ is the wave function of the electrons and nucleus. ∇_i and ∇_I correspond to the differential operator for the i-th electron and I-th nuclei, and are equal to $\left(\frac{\partial}{\partial x_i}, \frac{\partial}{\partial y_i}, \frac{\partial}{\partial z_i}\right)^{\mathrm{T}}$ and $\left(\frac{\partial}{\partial X_I}, \frac{\partial}{\partial Y_I}, \frac{\partial}{\partial Z_I}\right)^{\mathrm{T}}$, respectively. $\widehat{H}$ is the Hamiltonian, where the first term represents kinetic energy of the electrons, the second term represents the kinetic energy of the nucleus, the third term represents the interaction energy between the electrons and nuclei, the fourth term represents the repulsion energy between two electrons, and the fifth term represents the repulsion energy between two nuclei, respectively.

If one can solve this equation, the mechanisms of chemical reactions can be understood completely. However, the equations for actual molecular systems are too complex to solve analytically. Therefore, various theories and computational methods have been developed to obtain approximate solutions.

1.1.2 Born-Oppenheimer approximation

The Born-Oppenheimer approximation (8) is one of the most important approximations underlying various computational methods. Let's start with the following equations about the time-independent Schrödinger equation for electrons

$$\widehat{H}_e \psi_m(\mathbf{r}; \mathbf{R}) = E_m(\mathbf{R}) \psi_m(\mathbf{r}; \mathbf{R}) \tag{1.3}$$

$$\widehat{H}_e = -\sum_{i=1}^{n}\frac{1}{2}\nabla_i^2 - \sum_{i=1}^{n}\sum_{I=1}^{N}\frac{Z_I}{r_{iI}} + \sum_{i=1}^{n}\sum_{j>i}^{n}\frac{1}{r_{ij}} + \sum_{I=1}^{N}\sum_{J>I}^{N}\frac{Z_I Z_J}{r_{IJ}}. \tag{1.4}$$

In the equations, $\widehat{H}_e$ is the Hamiltonian for electrons, m is the index for the eigenstate, and $\psi_m(\mathbf{r};\mathbf{R})$ and $E_m(\mathbf{R})$ correspond to the m-th eigenfunction and eigenenergy of the $\widehat{H}_e$. $\psi_m(\mathbf{r};\mathbf{R})$ satisfies the orthonormality condition shown in the following equation,

$$\int_{-\infty}^{\infty}\cdots\int_{-\infty}^{\infty} d\mathbf{r}\ \psi_l^*(\mathbf{r};\mathbf{R})\psi_m(\mathbf{r};\mathbf{R}) = \delta_{lm}, \tag{1.5}$$

where δ_{lm} is Kronecker delta. If a set of eigenfunctions is complete, the wave functions for electrons and nucleus $\Psi(\mathbf{r},\mathbf{R})$ can be expressed as a linear combination of eigenfunctions $\psi_m(\mathbf{r};\mathbf{R})$ as follows,

$$\Psi(\mathbf{r},\mathbf{R},t) = \sum_{m=0}^{\infty}\psi_m(\mathbf{r};\mathbf{R})\,\chi_m(\mathbf{R},t), \tag{1.6}$$

where $\chi_m(\mathbf{R},t)$ is the coefficient of the linear combination and correspond to the wave function of the nucleus. Substituting **Equation (1.6)** into **Equation (1.1)**, multiplying $\psi_l^*(\mathbf{r};\mathbf{R})$ from the left and integrating over $\mathbf{r}$, the following equation is obtained.

$$\begin{aligned} i\hbar\frac{\partial\chi_l}{\partial t}(\mathbf{R},t) &= \left(-\sum_{I=1}^{N}\frac{1}{2M_I}\nabla_I^2 + E_l(\mathbf{R})\right)\chi_l(\mathbf{R},t) \\ &- \sum_{m=0}^{\infty}\left(\sum_{I=1}^{N}\frac{1}{2M_I}\int d\mathbf{r}\,\psi_l^*(\mathbf{r},\mathbf{R})\nabla_I^2\psi_m(\mathbf{r},\mathbf{R})\right)\chi_m(\mathbf{R},t) \\ &- \sum_{m=0}^{\infty}\left(\sum_{I=1}^{N}\frac{1}{M_I}\int d\mathbf{r}\,\psi_l^*(\mathbf{r},\mathbf{R})\nabla_{\mathrm{I}}\psi_m(\mathbf{r},\mathbf{R})\nabla_{\mathrm{I}}\right)\chi_m(\mathbf{R},t). \end{aligned} \tag{1.7}$$

When neglecting the second term of the right-hand side in **Equation (1.7)**, the equation represents the Schrödinger equation for the dynamics of nuclear wave packet $\chi_l(\mathbf{R},t)$ in which $E_l(\mathbf{R})$ is regarded as the potential energy. In this sense, $E_l(\mathbf{R})$ is called potential energy surface (PES) with the coordinates of nuclei as parameters (9). The PES for the lowest eigenenergy (l = 0) is called the PES

for the ground state. In fact, however, the nuclear wave packet on one PES can move to another PES due to the existence of the second term. The effect of the second term is important only when multiple PESs get close and can be ignored in the ground state dynamics. This approximation is called the Born-Oppenheimer (BO) approximation (8). Under the BO approximation, a chemical reaction is represented as the dynamics of a nuclear wave packet on the single PES as described above. There are mainly two theories to solve **Equation (1.3)**, the wave function theory based on the Hartree-Fock approximation (10), and the density functional theory based on the Kohn-Sham equation (11,12).

1.1.3 Classical limit

Since the mass of nuclei is usually large than electron, the quantum effect of nucleus can be ignored. By applying classical limit to the Schrödinger equation, (7) the following equations of motion are obtained.

$$\begin{cases} \dfrac{dQ_I}{dt} = \dfrac{\partial H_{cl}}{\partial P_{X_I}} \\ \dfrac{dP_{Q_I}}{dt} = -\dfrac{\partial H_{cl}}{\partial Q_I} \end{cases} (Q = X, Y, Z, I = 1 - N) \tag{1.8}$$

$$H_{cl} = \sum_{I=1}^{N} \frac{P_{Q_I}^2}{2M_I} + E_l(\mathbf{R}). \tag{1.9}$$

These equations are called Hamilton's canonical equations of motion (13). In the equations, Q_I $(Q = X, Y, Z)$ is the position of I-th nucleus and P_{Q_I} is the momentum corresponding to Q_I. H_{cl} is the classical Hamiltonian. These equations represent a classical motion of nuclei on the PES. Ab initio molecular dynamics (AIMD) (14,15) is one of the most popular methods to simulate classical motions of nuclei on the PES. In the AIMD calculations, gradient calculations based on quantum chemical

calculations and the update of the velocity and geometries are repeated. As a result, a series of geometries called a trajectory is obtained.

1.1.4 Transition State Theory

In contrast to the above-mentioned picture that treats the dynamics of nuclei on the PES explicitly, reaction kinetics is a picture that treats chemical reactions as the time evolution of the concentration of each chemical species, ignoring the detailed motion of nuclei (16,17). In the picture of reaction kinetics, the reaction rate is very useful concept, which is defined as the change in concentration per unit time. When the reaction rate is proportional to the concentration of power to d, it is called the d-th order reaction, and the coefficient is called the rate constant. Rate constants are often computed from the experiment. To simulate chemical reactions kinetically, one needs a theory to estimate rate constants based on quantum chemical calculations. Transition state theory (TST) (18) has enabled the computation of the rate constant without using any experimental parameters. TST treats the dynamics of chemical reactions statistically, rather than explicitly to estimate the rate constant from the PES information alone.

In TST, two assumptions are introduced. One is non-recrossing assumption. In this assumption, a concept termed a transition state (TS) is defined. TS is a hyperplane that divides phase space into reactant region and product region. The non-recrossing assumption assumes that once trajectories from the reactant region cross TS to the product region, they never return to the reactant region. The other is the quasi-equilibrium assumption, which assumes that the thermal equilibrium

between is satisfied in the reactant region. Based on these two assumptions, a rate constant is estimated based on the following equation.

$$k = \frac{k_B T}{h} \frac{Q_{TS}}{Q_R} \exp\left(-\frac{\Delta\Delta E}{k_B T}\right). \quad (1.10)$$

In **Equation (1.10)**, k is the rate constant, k_B is Boltzmann's constant, T is temperature, h is Planck constant, and Q_{TS} and Q_R are the distribution functions for TS and reactants, respectively. $\Delta\Delta E$ is the potential energy difference between the reactant region and TS. Reactant region and TS are usually characterized by minimum (MIN) on the PES and first-order saddle point on the PES. Q_{TS} and Q_R are also estimated based on the harmonic approximation for those points. Once the rate constants are obtained, chemical reactions can be simulated by solving the resulting rate equations.

1.1.5 Geometry Optimization

As mentioned above, a reactant MIN and TS is necessary to evaluate rate constants by TST. Geometry optimization is a numerical calculation method to optimize these stationary points (19). The most of the optimization methods solve the following equation numerically.

$$\nabla \mathrm{V}(\mathbf{R}) = \mathbf{0}, \quad (1.11)$$

where $\mathrm{V}(\mathbf{R})$ represents the PES and corresponds to $E_0(\mathbf{R})$ for the ground state case. This equation indicates the gradient is zero vector, which should be satisfied at stationary points. One of the most basic optimization methods is Newton method (19). Newton method applies harmonic approximation at each optimization step and repeats to move to the stationary point on the approximate harmonic potential based on the following equation.

$$\mathbf{R}_{i+1} = \mathbf{R}_i - \mathbf{H}^{-1}\nabla \mathrm{V}(\mathbf{R}_i), \tag{1.12}$$

Here, **H** is Hessian. The optimization can be performed by repeating above step until the norm of gradient falls below a certain threshold. To reduce the computational cost of Hessian calculations, there are so-called quasi-Newton methods such as BFGS method (20-23), in which Hessian at one step is approximated using the gradient and potential energy at previous steps. In addition, Other methods such as the Rational function optimization (24) method and the Trust Radius (25) method are also effective.

1.1.6 Normal mode analysis

Normal mode analysis is (26) an operation to characterize MINs or TSs obtained by geometry optimizations. Normal mode analysis starts with the following Schrödinger equation under the harmonic approximation.

$$\mathbf{H}^{mw} = \mathbf{M}^{-\frac{1}{2}}\mathbf{H}\mathbf{M}^{-\frac{1}{2}} \tag{1.14}$$

$$\mathbf{M}^{-\frac{1}{2}} = \begin{pmatrix} M_1^{-\frac{1}{2}} & & & & & & \\ & M_1^{-\frac{1}{2}} & & & O & & \\ & & M_1^{-\frac{1}{2}} & & & & \\ & & & \ddots & & & \\ & & & & M_N^{-\frac{1}{2}} & & \\ & O & & & & M_N^{-\frac{1}{2}} & \\ & & & & & & M_N^{-\frac{1}{2}} \end{pmatrix} \tag{1.15}$$

$$\mathbf{P}^{-1}\mathbf{H}^{mw}\mathbf{P} = \begin{pmatrix} 0 & & & & & & & & & \\ & 0 & & & & & & & & \\ & & 0 & & & & & & & \\ & & & 0 & & & & & & \\ & & & & 0 & & & & & \\ & & & & & 0 & & & & \\ & & & & & & \lambda_1 & & & \\ & & & & & & & \lambda_2 & & \\ & & O & & & & & & \ddots & \\ & & & & & & & & & \lambda_{3N-7} \\ & & & & & & & & & & \lambda_{3N-6} \end{pmatrix} \tag{1.16}$$

$$\mathbf{P} = (\mathbf{l}_1, \cdots, \mathbf{l}_6, \mathbf{v}_1, \cdots, \mathbf{v}_{3N-6}) \tag{1.17}$$

In the equations, **P** is an orthogonal matrix which diagonalize the mass-weighted Hessian $\mathbf{H}^{mw}$. $\mathbf{l}_1, \cdots, \mathbf{l}_6$ are eigenvectors corresponding to the six translational and rotational modes, and $\mathbf{v}_1, \cdots, \mathbf{v}_{3N-6}$ are the other eigenvectors and usually called normal modes. Next, the following coordinate transformation

$$\mathbf{X} = \mathbf{P}^{-1}\mathbf{M}^{\frac{1}{2}}\mathbf{R} \tag{1.18}$$

$$\mathbf{M}^{\frac{1}{2}} = \begin{pmatrix} M_1^{\frac{1}{2}} & & & & & & & & \\ & M_1^{\frac{1}{2}} & & & & & & & \\ & & M_1^{\frac{1}{2}} & & & & & & \\ & & & \ddots & & & & & \\ & & & & M_N^{\frac{1}{2}} & & & & \\ & & & & & M_N^{\frac{1}{2}} & & & \\ & & & & & & M_N^{\frac{1}{2}} & & \\ & & & & & & & M_N^{\frac{1}{2}} & \end{pmatrix}. \tag{1.19}$$

These equations are substituted into **equation (1.13)** to give the following equations.

$$\left(\sum_{v=1}^{3N-6} \hat{h}_v(X_v)\right)\phi_u(\mathbf{X}) = E_u^{vib}\phi_u(\mathbf{X}) \tag{1.20}$$

$$\hat{h}_v(X_v) = -\frac{1}{2}\frac{\partial^2}{\partial X_v^2} + \frac{1}{2}\lambda_v X_v^2. \tag{1.21}$$

These equations indicate that the nuclear dynamics can be represented as $3N-6$ independent harmonic

oscillators. Here, $\hat{h}_v$ indicates the Hamiltonian for the v-th normal mode. The eigenenergy for the following equation

$$\hat{h}_v f_{s_v}(X_v) = \epsilon_{s_v} f_{s_v}(X_v) \tag{1.22}$$

is represented by the following equations.

$$\epsilon_{s_v} = \left(s_v + \frac{1}{2}\right)\hbar\omega_v \tag{1.23}$$

$$\omega_v = \sqrt{\lambda_i} \tag{1.24}$$

Here, s_v is the index for the vibrational eigenstate for $\hat{h}_v$, $f_{s_v}(X_v)$ and ϵ_{s_v} are the wavefunction and eigenenergy for the s_v-th vibrational eigen state, and ω_v is the angular frequency for the v-th normal mode. By using ϵ_{s_v} and $f_{s_v}(X_v)$, E_u^{vib} and $\phi_u(\mathbf{X})$ are represented as follows.

$$E_u^{vib} = \sum_{v=1}^{3N-6} \epsilon_{s_v} \tag{1.25}$$

$$\phi_u(\mathbf{X}) = \prod_{v=1}^{3N-6} f_{s_v}(X_v)\,. \tag{1.26}$$

By using E_u^{vib} the vibrational partition function (26) can be computed as follows.

$$Q_{vib} = \sum_{u=0} \exp\left(-\frac{E_u^{vib}}{k_B T}\right). \tag{1.27}$$

The partition function can be used to estimate the rate constants based on TST. Once the partition function is obtained, various thermodynamical properties such as free energy can be obtained (26).

In addition, the normal mode analysis is used to judge whether the optimized stationary point is MIN, TS or the others by checking the number of negative eigenvalues (the number of imaginary frequencies). MIN has no negative eigenvalues (no imaginary frequencies), TS has one negative eigenvalue (one imaginary frequencies). The stationary points with more than two negative

eigenvalues correspond to higher order saddle points.

1.1.7 Reaction Path

As mentioned above, chemical reactions can be described as classical motions of nuclei on the PES, and there are innumerable possibilities of classical trajectories from reactants to products. The concept of a reaction path is introduced as a single pathway on the PES connecting reactants (intermediates) and products (intermediates) representing ensemble of trajectories. There are various definitions exist, and the most widely used definition is the intrinsic reaction coordinate (IRC) (27-29). An IRC path is defined as the steepest descent path from TS in the mass-weighted coordinate and satisfies the following equation

$$\frac{d\mathbf{Q}}{ds} = \begin{cases} -\dfrac{\mathbf{g}}{|\mathbf{g}|}\,(s > 0) \\ \mathbf{v}_1\,(s = 0) \\ \dfrac{\mathbf{g}}{|\mathbf{g}|}\,(s < 0) \end{cases} . \tag{1.28}$$

Here, $\mathbf{Q}$ is mass-weighted cartesian coordinate of nuclei, and s represents the reaction coordinate along the IRC path. $\mathbf{g}$ is the mass-weighted gradient vector, and $\mathbf{v}_1$ is the normal mode vector corresponding to the negative eigenvalue. Numerical methods such as LQA method (30), give an IRC path that connects two MINs via a TS (**Figure 1.1**). The IRC path has played an important role in the theoretical analysis of chemical reactions to investigate the structural and energy changes associated with elementary processes (29).

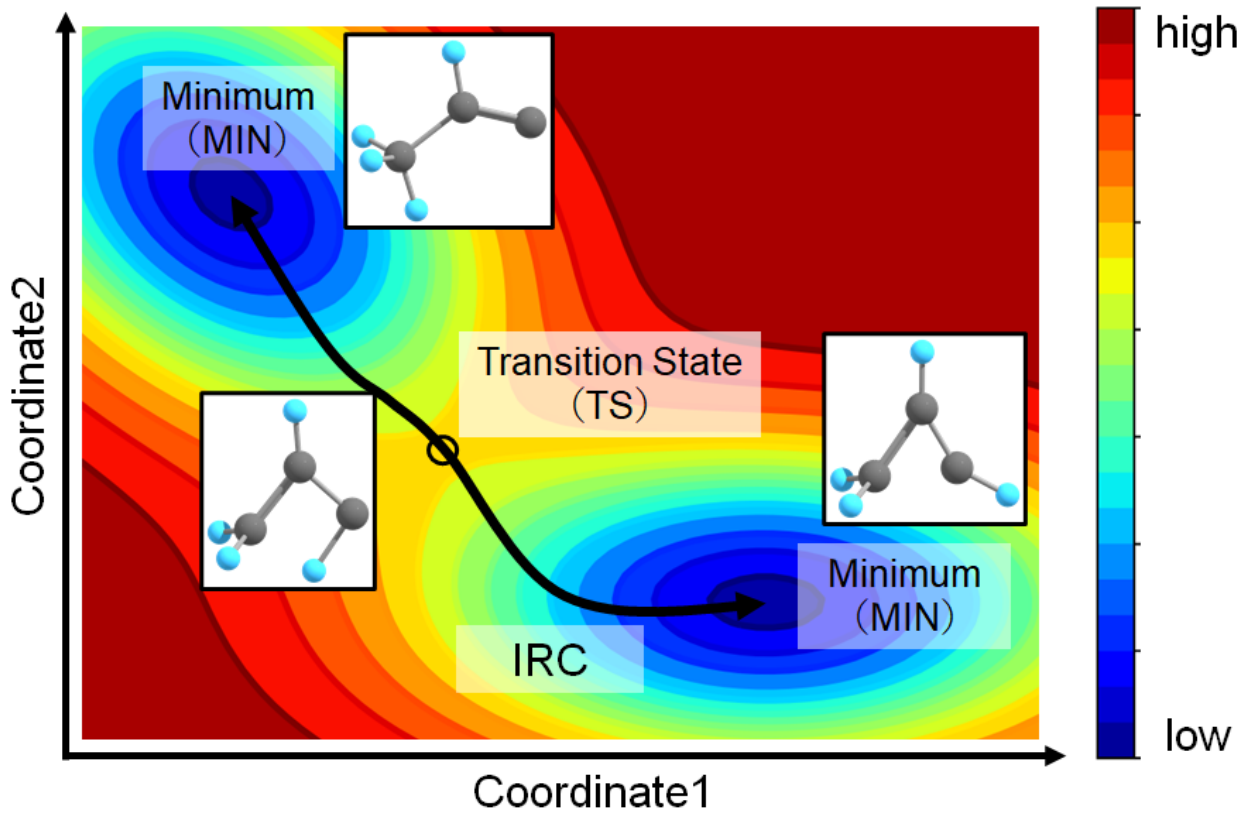

Figure 1.1. A schematic picture of an intrinsic reaction coordinate path on the potential energy surface.

1.1.8 Reaction Path Network

In the TST and IRC-based picture described above, chemical reactions are described as transitions from a MIN to another MIN. Usually, there are a lot of MINs on the PES corresponding to reactants, products, and intermediates, which are connected by the IRC paths. To understand the whole chemical reaction, all MINs and IRC paths on the PES should be considered. A reaction path network (31) is introduced to understand chemical reactions based on the network theory. In a reaction path network, the MINs on the PES are represented as nodes and IRC paths as edges (**Figure 1.2**). A reaction path network can be constructed if all MINs and TSs on the PES is obtained. By computing rate constants for IRC paths in the network based on TST, the following rate equations are obtained.

$$\frac{d\mathbf{p}}{dt} = \mathbf{K}\mathbf{p} \tag{1.29}$$

$$\mathbf{p} = ([0], [1], \cdots [N_{\mathrm{MIN}}])^{\mathrm{T}} \tag{1.30}$$

$$(\mathbf{K})_{ab} = \begin{cases} -\sum_{c}^{N_{\mathrm{MIN}}} k_{ac} \, (a = b) \\ k_{ba} (a \neq b) \end{cases}, \tag{1.31}$$

where N_{MIN} is the number of MINs on the PES, $\mathbf{p}$ is a vector with the concentration of each MIN $[0], [1], \cdots [N_{\mathrm{MIN}}]$ as elements, $\mathbf{K}$ is the rate constant matrix and a, b, and c represent the index of MIN. k_{ac} and k_{ba} are the rate constant for the elementary process from the a-th MIN to the c-th MIN and that for the elementary process from the b-th MIN to the a-th MIN. The chemical reaction can be simulated by integrating **Equation (1.29)** and investigating the time evolution of $[0], [1], \cdots [N_{\mathrm{MIN}}]$. Numerical integration algorithms, such as the Runge-Kutta method, are available to solve this equation. However, in general, reaction path networks include both fast processes such as conformational changes, and slow processes such as bond cleavages which make the equation difficult to solve numerically. To solve this problem, a method called the rate constant matrix contraction (RCMC) method was developed (32).

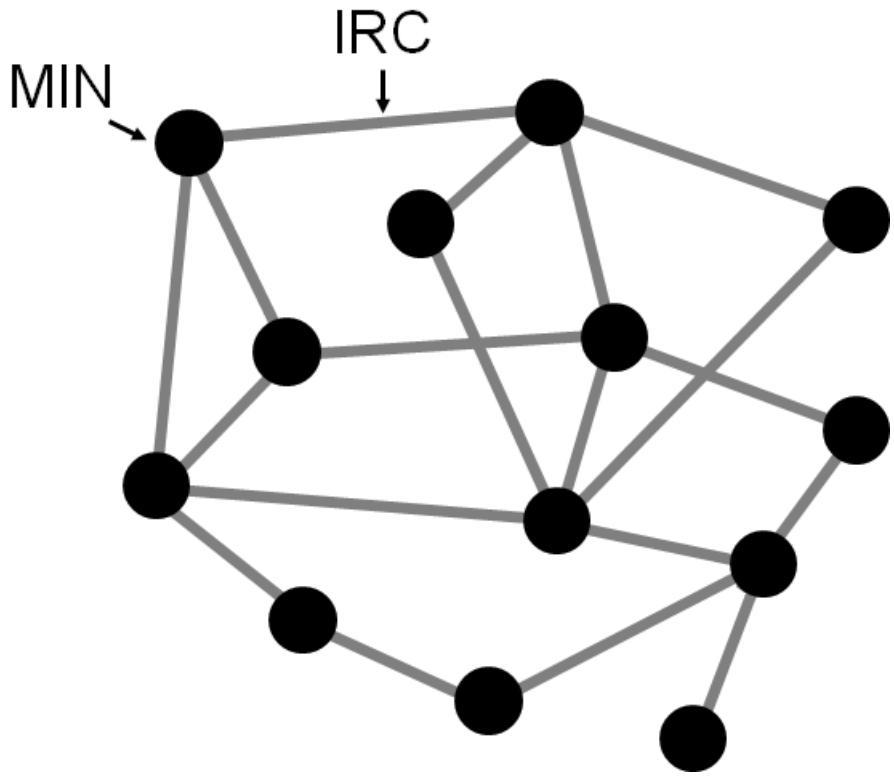

Figure 1.2. A schematic picture of a reaction path network. Nodes and edges represent minima and intrinsic reaction coordinate paths.

1.1.7 Automated reaction path search

To predict chemical reactions based on theoretical calculations accurately, exhaustive search of all the MINs and TSs on the PES is necessary. However, this is extremely difficult to achieve. The simplest approach is constructing the full-dimensional PES by solving **Equation (1.3)** for all possible **R** to obtain $E_m(\mathbf{R})$. But its computational cost increases exponentially as N increases, and this approach is not practical for actual molecular systems. Another approach is geometry optimizations from randomly generated structures (33), which has no guarantee of exhaustiveness. One solution to this problem is to develop a method to find all reaction paths starting from a given

MIN. Repeating this method to newly obtained MINs finally gives a reaction path network automatically. This concept is called the automated reaction path search (34). The anharmonic downward distortion following (ADDF) method (35-37) was the first method to achieve this. The ADDF method traces the point where the difference between the approximate harmonic potential and the actual PES is maximum. Currently, there are several automated reaction path search methods exist, such as the growing string method (38), AutoMeKin2021 (39), the artificial force induced reaction (AFIR) method (40,41), and so on.

Here, the detail of the AFIR method which is mainly used through this thesis is explained. The AFIR method was developed by Maeda and Morokuma in 2010 (40) and is applicable to larger molecular systems compared to the ADDF method. The concept of the AFIR method is inducing chemical reactions by applying pushing or pulling force to a molecule. In the actual AFIR calculations, the following function called the AFIR function is minimized to trace a reaction path.

$$F(\mathbf{R}) = V(\mathbf{R}) + \rho\alpha\frac{\sum_{I\in A}\sum_{J\in B}\omega_{IJ}r_{IJ}}{\sum_{I\in A}\sum_{J\in B}\omega_{IJ}}. \tag{1.32}$$

Here, A and B are the fragments to which the artificial force is applied. The second term represents the force that pulls apart or pushes together A and B. ρ is the sign of the force and is set to either 1 (push) or -1 (pull). ω_{IJ} is a weight function defined by

$$\omega_{IJ} = \left[\frac{D_I + D_J}{r_{IJ}}\right]^6, \tag{1.33}$$

where D_I and D_J are the covalent radii of the I-th and J-th atoms, respectively. α is a parameter representing the strength of the force, defined by

$$\alpha = \frac{\gamma}{\left[2^{-\frac{1}{6}} - \left(1 + \sqrt{1 + \frac{\gamma}{\epsilon}}\right)^{-\frac{1}{6}}\right] R_0}, \tag{1.34}$$

where R_0 and ε are the Leonard–Jones parameters for Ar–Ar, which are 3.8164 Å and 1.0061 kJ mol^{-1}, respectively. In the standard procedure of the AFIR method, the minimization of $F(\mathbf{R})$ from the initial structure is performed to obtained so-called the AFIR path. Next, TS optimization from the energy maximum of the obtained AFIR path is performed, and the IRC path is calculated from the obtained TS.

The single component (SC)-AFIR method (42) is a method to yield a reaction path network based on the AFIR method. In order to search for reaction paths around the input molecule, the SC-AFIR method enumerates all combinations of atom pairs in the molecule, defines fragments A and B for the obtained atom pairs automatically, and applies the AFIR method. By repeating this operation the newly obtained MINs, the SC-AFIR method yields a reaction path network. The SC-AFIR method has been applied to various systems to construct reaction path networks (43-46).

In summary, ab initio prediction of chemical reactions has become possible by combining various approximations such as BO approximation, the classical limit, and TST, and various computational methods such as geometry optimization techniques, the normal mode analysis, and automated reaction path search and the kinetic analysis of reaction path networks (**Figure 1.3**).

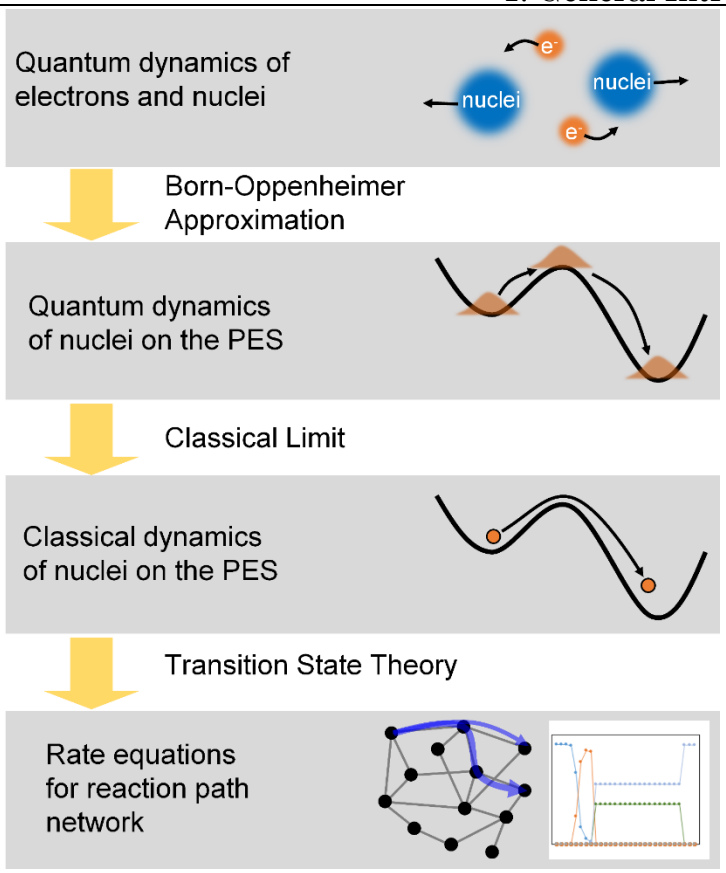

Figure 1.3. An overview for theoretical analysis of chemical reactions.

1.2 Dynamical Bifurcations

1.2.1 Dynamic effects of nuclei

As mentioned above, analyses based on reaction path networks are based on various approximations. Therefore, various effects are ignored, and it is sometimes important to incorporate these effects in some cases. For example, the BO approximation neglects the effect of nonadiabatic transitions through multiple PESs, which is important for the non-radiative decay processes after photoexcitation (47). The quantum effect of nuclei is also neglected in the picture of classical mechanics, which becomes important for light atoms such as hydrogen (48).

The main focus of this thesis is the effect of nuclear momentum (49, 50), which is ignored

in the kinetics based on TST and IRC. This effect is important when the two assumptions of TST are not satisfied, or when the IRC path does not represent actual molecular motion. For example, there is a report that the quasi-equilibrium assumption is not satisfied in a hydroboration reaction and TST fails to estimate the reaction selectivity quantitatively (51). There is also another report for an S_N2 reaction that actual molecular dynamics trajectories deviate from the IRC path at the highly curved region (52).

1.2.2 Dynamical bifurcations

Dynamic bifurcation is a phenomenon in which nuclear dynamic effects have the greatest impact on reaction selectivity (53,54). In dynamical bifurcations, an ensemble of trajectories passing through a single TS bifurcates to multiple product MINs. **Figure 1.4** shows two PESs in which dynamical bifurcations occur, and a PES in which a dynamical bifurcation does not occur. **Figure 1.4a** shows a symmetrical PES in which a dynamical bifurcation occurs from TS1. In this case, it is obvious that an ensemble of trajectories passing through TS1 bifurcates to P1 and P2 at a ratio of 0.5:0.5. **Figure 1.4b** shows a slightly asymmetrical PES. In this case, an ensemble of trajectories still bifurcates to P1 and P2, though the branching ratio is no longer 0.5:0.5. **Figure 1.4c** shows a case for a highly asymmetrical PES. In this case, dynamical bifurcations do not occur on the PES and trajectories only reach P1. In asymmetrical cases like **Figure 1.4b**, dynamical bifurcations cannot be discussed based on the IRC approach since an IRC path is a single reaction path via a TS and does not bifurcate. In addition, TST does not compute rate constants for dynamical bifurcations, in which

multiple elementary processes occur via a TS since TST gives one rate constant for one TS. Therefore, current theoretical analyses based on the IRC path and reaction path networks give incorrect reaction mechanisms for chemical reactions including dynamical bifurcations.

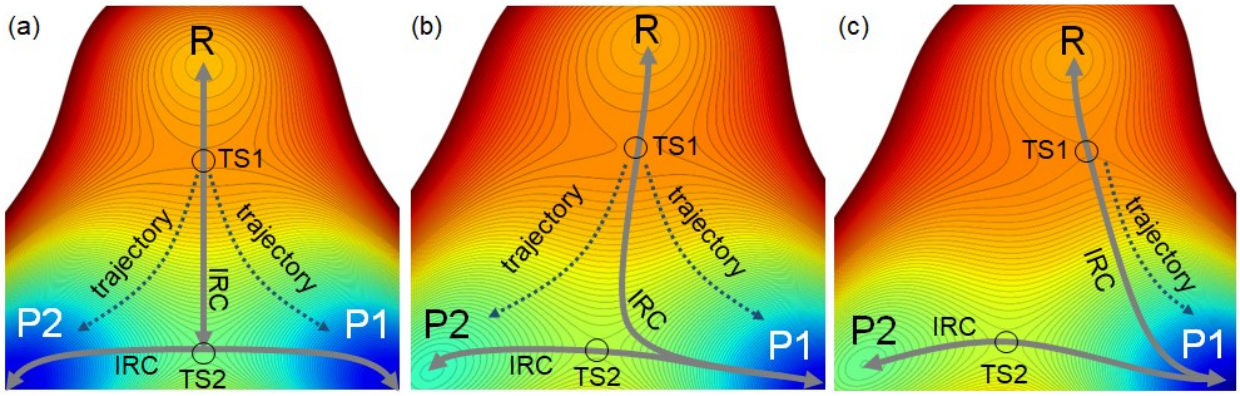

Figure 1.4 A schematic pictures of two potential energy surfaces (PESs) in which dynamical bifurcations occur and a PES in which a dynamical bifurcation does not occur. (a) shows a symmetrical PES in which a dynamical bifurcation occurs, (b) shows an asymmetrical PES in which a dynamical bifurcation occurs, and (c) shows an asymmetrical PES in which a dynamical bifurcation does not occur.

1.2.3 Valley-ridge transition

When a dynamical bifurcation occurs, it is known that the shape of PES perpendicular to the reaction path should change from a valley to a ridge (**Figure 1.5**) (29). Ruedenberg et al. defined the valley-ridge inflection (VRI) point to discuss such phenomena (55). The VRI point needs to satisfy the following two conditions: one of the eigenvalues of Hessian is zero, and the eigenvector

corresponding to the zero eigenvalue is orthogonal to the gradient vector. Gill proposed a method to locate the VRI point based on the following equation (56),

$$\mathbf{H}^p = \left(1 - \sum_{v=1}^{7} \mathbf{l}_v^T \mathbf{l}_v\right) \mathbf{H} \left(1 - \sum_{v=1}^{7} \mathbf{l}_v^T \mathbf{l}_v\right), \tag{1.35}$$

where $\mathbf{H}^p$ is the Hessian from which the gradient vector is projected out, and $\mathbf{l}_v$ is the unit vector. $\mathbf{l}_v (v = 1-6)$ corresponds to the 3 translational and 3 rotational vectors, and $\mathbf{l}_7$ corresponds to the tangent vector of the IRC path. The normal mode analysis using $\mathbf{H}^p$ yields $3N-7$ non-zero eigenvalues. The sign of eigenvalues indicates the shape of PES: a positive eigenvalue corresponds to a valley, while a negative eigenvalue corresponds to a ridge. The proposed method locates the VRI point on the IRC path by locating the point at which one of the eigenvalues change its sign from positive to negative. It is known that the obtained point on the IRC path satisfies the two conditions for the VRI point only for dynamical bifurcations giving two symmetrical products (termed as non-totally symmetric bifurcations), and in general, the obtained point is not the VRI point for the non-symmetrical cases (termed as totally symmetric bifurcations) (57). Then, a concept called a valley-ridge transition (VRT) point was introduced, which is a point on the IRC path where the sign of one eigenvalue of $\mathbf{H}^p$ changes from positive to negative (58). This VRT-based analysis was applied to non-totally symmetric bifurcations and totally symmetric bifurcations to discuss the occurrence of dynamical bifurcations. However, the VRT-based analysis does not provide information about bifurcation products different from the IRC product. In addition, the VRT discusses dynamical bifurcations based on the shape of the PES, and there are cases of dynamic bifurcation even in the

case without the VRT point on the IRC path (57). Therefore, a method to search for dynamical bifurcations and its products is necessary.

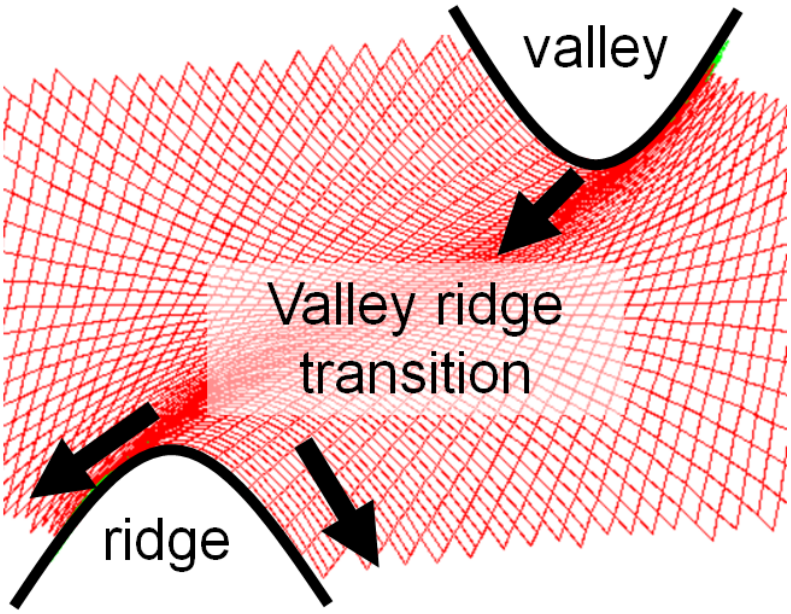

Figure 1.5 A schematic picture representing a potential energy surface including valley-ridge transition.

1.2.4 Ab initio molecular dynamics

AIMD is one of the most promising ways to simulate dynamical bifurcations, which can deal with classical motions of nuclei after passing through a TS explicitly (50). By sampling initial positions and initial velocities around the TS based on the thermal distribution and calculating AIMD trajectories from them, the bifurcating products and branching ratio can be investigated. However, the computational cost of AIMD calculations is expensive because hundreds of trajectories are necessary to estimate the branching ratio for a dynamical bifurcation. Therefore, it is difficult to apply the AIMD calculations directly to the search for dynamical bifurcations on the reaction path network.

In addition, AIMD calculations cannot simulate chemical reactions for a long time such as seconds, minutes or days. The selectivity of chemical reactions including dynamical bifurcations is decided by not only short-time dynamics after passing through a TS, but also long-time kinetics for the interconversion of products. Therefore, a method to simulate chemical reactions considering both short-time dynamics and long-time kinetics is desired.

1.2.5 Dynamical bifurcations in organic reactions

In early studies, dynamical bifurcations have been studied for some basic reactions, such as the isomerization of methoxyradical (59-61), the ring-opening reaction of cyclopropylidene (62,63), and so on. In recent decades, dynamical bifurcations have been reported in actual organic reactions. In 2002, Caramella et al. discussed a dimerization of cyclopentadiene based on the secondary orbital interaction and reported that two Diels-Alder reactions occur via a single TS (64). They termed this TS a bispericyclic TS because the TS included two pericyclic reactions. Houk proposed a more general concept called an ambimodal TS (65,66). An ambimodal TS is a TS through which two or more elementary reactions occur simultaneously. In other words, a dynamical bifurcation occurs in an ambimodal TS. Houk and Singleton have studied ambimodal TSs for various pericyclic reactions (67-82). Tantillo have reported the occurrence of dynamical bifurcations of terpene biosynthesis (83,84). Yamataka et al. have reported dynamical bifurcations in Schmidt reactions (85) and Beckmann reactions (86,87). In addition, it has been reported that organometallic reactions (88-92) and enzyme reactions (93-95) also include dynamical bifurcations.

Although a variety of chemical reactions have been reported to include dynamical bifurcations as shown above, they are part of numerous chemical reactions, and the generality of dynamical bifurcations is unknown. Most mechanistic studies ignore the effect of dynamical bifurcations, considering it to have little effect on the reaction mechanism. To reveal the importance of dynamical bifurcations, a method to investigate the possibility of dynamical bifurcations for a given system is necessary.

1.3 Overview of this thesis

In this thesis, I aim to establish a method to analyze chemical reactions including dynamical bifurcations theoretically by developing a method to search for dynamical bifurcations on the PES, a method to perform a kinetic analysis on a reaction path network including dynamical bifurcations, and a method to investigate the possibility of dynamical bifurcations for a given system.

This doctoral thesis consists of six chapters. **Chapter 1** summarizes the background of my research about dynamical bifurcations.

In **Chapter 2**, a method to search for dynamical bifurcations based on the AFIR method is developed. The method finds dynamical bifurcations based on paths traced by the AFIR method. The automated search method was applied to a Diels-Alder reaction between 2-vinylfuran and 3-methoxycarbonylcyclopentadiene, and it was found that six dynamical bifurcations including the reported one were explored using my method.

In **Chapter 3**, a method to perform a kinetic analysis for a reaction path network including

dynamical bifurcations is proposed. The proposed method consists of three methods; the automated search method introduced in **Chapter 2**, the AIMD calculations to estimate the branching ratio, and a method to compute rate constants for dynamical bifurcations. The method is applied to an intramolecular Diels-Alder reaction and it was found that the experimental selectivity can be reproduced qualitatively only by including dynamical bifurcations to the kinetic simulation.

In **Chapter 4**, a machine learning model to predict branching ratio without AIMD calculations is introduced to accelerate the kinetic analysis proposed in **Chapter 2**. The method was found to reproduce the result of kinetic analysis based on the AIMD method. In addition, the machine learning-assisted kinetic analysis is applied to a larger reaction path network for a retrosynthesis of difluoroglycine.

In **Chapter 5**, I propose a computational method to systematically detect the dynamical bifurcations induced by perturbations, such as mechanical forces or substitutions, which has been overlooked in the previous method introduced in **Chapter 1**. The method was applied to three pericyclic reactions and it was found that dynamical bifurcations can be induced by perturbations in two out of three reactions.

Chapter 6 summarizes this thesis and describes about future perspective.

1.4 Reference

1. Muller, P. Glossary of terms used in physical organic chemistry (IUPAC Recommendations 1994). *Pure & Appl. Chem.* **1994**, 66, 1077−1184. https://doi.org/10.1351/pac199466051077.

2. Grimme, S.; Schreiner, P. R. Computational Chemistry: The Fate of Current Methods and Future Challenges. Angew. Chem. Int. Ed. **2017**, 57, 4170−4176. https://doi.org/10.1002/anie.201709943.

3. Houk, K. N.; Liu, F. Holy Grails for Computational Organic Chemistry and Biochemistry. *Acc. Chem. Res.* **2017**. 50. 539−543. https://doi.org/10.1021/acs.accounts.6b00532.

4. Houk, K. N.; Cheong, P. H. Computational prediction of small-molecule catalysts. Nature **2008** 455, 309−313. https://www.nature.com/articles/nature07368.

5. Hayashi, H.; Maeda, S.; Mita, T. Quantum chemical calculations for reaction prediction in the development of synthetic methodologies. *Chem. Sci.* **2023**, 14, 11601−11616. https://doi.org/10.1039/d3sc03319h.

6. Schrödinger, E. Quantisierung als Eigenwertproblem. *Ann. Phys. (Berl.)* **1926**, 384, 361−376. https://doi.org/10.1002/andp.19263840404.

7. Sakurai, J. J.; Napolitano, J. MODERN QUANTUM MECHANICS, 2nd Edition, Addison Wesley, USA, 2010.

8. Born, M.; Oppenheimer, R. Zur Quantentheorie der Molekeln. *Ann. Phys. (Berl.)* **1927**, 389, 457−484. https://doi.org/10.1002/andp.19273892002.

9. Schlegel, H. B. Exploring potential energy surfaces for chemical reactions: An overview of some practical methods. *J. Comput. Chem.* **2003**, 24, 1514−1527. https://doi.org/10.1002/jcc.10231.

10. Szabo, A.; Ostlund, N. S.; Modern Quantum Chemistry: Introduction to Advanced Electronic Structure Theory. Dover, New York, 1996.

11. Hohenberg, P.; Kohn, W. Inhomogeneous Electron Gas. *Phys. Rev.* **1964**, 136, B864−B871. http://dx.doi.org/10.1103/physrev.136.b864.

12. Kohn, W.; Sham, L. J. Self-Consistent Equations Including Exchange and Correlation Effects. *Phys. Rev.* **1965**, *140*, A1133– A1138. https://doi.org/10.1103/PhysRev.140.A1133.

13. Goldstein, H.; Poole, C.; Safko, J. Classical Mechanics. Pearson Education Limited, UK, 2014.

14. Gordon, M. S.; Chaban, G.; Taketsugu, T. Interfacing electronic structure theory with dynamics. J. Phys. Chem. **1996**, 100, 11512−11525. https://doi.org/10.1021/jp953371o.

15. Pratihar, S.; Ma, X.; Homayoon, Z.; Barnes, G. L.; Hase, W. L. Direct Chemical Dynamics Simulations. *J. Am. Chem. Soc.* **2017**, 139, 3570−3590. https://doi.org/10.1021/jacs.6b12017.

16. Fernández-Ramos, A.; Miller, J. A.; Klippenstein, S. J.; Truhlar, D. G. Modeling the Kinetics of Bimolecular Reactions. *Chem. Rev.* **2006**, *106* (11), 4518–4584. https://doi.org/10.1021/cr050205w.

17. Klippenstein, S. J.; Pande, V. S.; Truhlar, D. G. Chemical Kinetics and Mechanisms of Complex Systems: A Perspective on Recent Theoretical Advances. *J. Am. Chem. Soc.* **2014**, *136* (2), 528–546. https://doi.org/10.1021/ja408723a.

18. Eyring, H. The Active Complex in Chemical Reactions. J. Chem. Phys. **1935**, 3, 107–115. https://doi.org/10.1063/1.1749604.

19. Schlegel, H. B. Geometry optimization. *WIREs Comput Mol Sci.* **2011**, 1, 790–809. https://doi.org/10.1002/wcms.34.

20. Broyden, C. G. The Convergence of a Class of Double-rank Minimization Algorithms 1. General Considerations. *IMA J. Appl. Math* **1970**, 6, 76–90. https://doi.org/10.1093/imamat/6.1.76.

21. Fletcher, R. A new approach to variable metric algorithms. *Comput. J.* **1970**, 13, 317–322. https://doi.org/10.1093/comjnl/13.3.317.

22. Goldfarb D. A family of variable metric methods derived by variational means. *Math Comput.* **1970**, 24, 23–26. https://doi.org/10.1090/S0025-5718-1970-0258249-6.

23. Shanno D. F. Conditioning of quasi-Newton methods for functional minimization. *Math Comput.* **1970**, 24, 647–657. https://doi.org/10.1090/S0025-5718-1970-0274029-X.

24. Banerjee, A.; Adams, N.; Simons, J.; Shepard R. Search for stationary points on surfaces. *J. Phys. Chem.* **1985**, 89, 52–57. https://doi.org/10.1021/j100247a015.

25. Sorensen, D. C. Newton's Method with a Model Trust Region Modification. *SIAM J. Math. Anal.* **1982**, 19, 409–426. https://doi.org/10.1137/0719026.

26. Hal Tasaki Toukei Rikigaku I. Baifukan, Japan, 2008.

27. Fukui, K. Formulation of the Reaction Coordinate. *J. Phys. Chem.* **1970**, *74* (23), 4161–4163. https://doi.org/10.1021/j100717a029.

28. Fukui, K. The Path of Chemical Reactions - The IRC Approach. *Acc. Chem. Res.* **1981**, *14* (12), 363–368. https://doi.org/10.1021/ar00072a001.

29. Maeda, S.; Harabuchi, Y.; Ono, Y.; Taketsugu, T.; Morokuma, K. Intrinsic Reaction Coordinate: Calculation, Bifurcation, and Automated Search. *Int. J. Quantum Chem.* **2015**, 115 (5), 258−269. https://doi.org/10.1002/qua.24757.

30. Page. M.; Doubleday, C.; Mclver Jr, J. W. Following steepest descent reaction paths. The use of higher energy derivatives with *ab initio* electronic structure methods. *J. Phys. Chem.* 1990, 93, 5634–5642. https://doi.org/10.1063/1.459634.

31. Maeda, S.; Harabuchi, Y.; Hayashi, H.; Mita, T. Toward Ab Initio Reaction Discovery Using the Artificial Force Induced Reaction Method. *Annu. Rev. Phys. Chem.* **2023**, 74, 287–311. https://doi.org/10.1146/annurev-physchem-102822-101025.

32. Sumiya, Y.; Maeda, S. Rate Constant Matrix Contraction Method for Systematic Analysis of Reaction Path Networks. *Chem. Lett.* **2020**, *49* (5), 553–564. https://doi.org/10.1246/cl.200092.

33. Bera, P. P.; Sattelmeyer, K. W.; Saunders, M.; Schaefer, H. F.; Schleyer, P. v. R. Mindless Chemistry. *J. Phys. Chem. A* **2006**, 110 (13), 4287–4290. https://doi.org/10.1021/jp057107z.

34. Maeda, S.; Ohno, K.; Morokuma K. Systematic exploration of the mechanism of chemical reactions: the global reaction route mapping (GRRM) strategy using the ADDF and AFIR methods. *Phys. Chem. Chem. Phys.* **2013**, 15, 3683–3701. https://doi.org/10.1039/C3CP44063J.

35. Maeda, S.; Ohno, K. A New Method for Constructing Multidimensional Potential Energy Surfaces by a Polar Coordinate Interpolation Technique. *Chem. Phys. Lett.* **2003**, *381* (1–2), 177–186. https://doi.org/10.1016/j.cplett.2003.08.129.

36. Ohno, K.; Maeda, S. A Scaled Hypersphere Search Method for the Topography of Reaction Pathways on the Potential Energy Surface. *Chem. Phys. Lett.* **2004**, *384* (4–6), 277–282. https://doi.org/10.1016/j.cplett.2003.12.030.

37. Maeda, S.; Ohno, K. Global Mapping of Equilibrium and Transition Structures on Potential Energy Surfaces by the Scaled Hypersphere Search Method: Applications to Ab Initio Surfaces of Formaldehyde and Propyne Molecules. *J. Phys. Chem. A* **2005**, *109* (25), 5742–5753. https://doi.org/10.1021/jp0513162.

38. Zimmerman, P. M. Single-ended transition state finding with the growing string method. *J. Comput. Chem.* **2015**, 36, 601–611. **https://doi.org/10.1002/jcc.23833.**

39. Martínez-Núñez, E.; Barnes, G. L.; Glowacki, D. R.; Kopec, S.; Peláez, D.; Rodríguez, A.; Rodríguez-Fernández, R.; Shannon, R. J.; Stewar, J. J. P.; Tahoces, P. G.; Vazquez, S. A. AutoMeKin2021: An open-source program for automated reaction discovery. *J. Comput. Chem.*, **2021**, 42, 2036–2048. https://doi.org/10.1002/jcc.26734.

40. Maeda, S.; Morokuma, K. Communications: A systematic method for locating transition structures of A+B→X type reactions. *J. Chem. Phys.* **2010**, 132, 241102. https://doi.org/10.1063/1.3457903.

41. Maeda, S.; Harabuchi, Y. Exploring paths of chemical transformations in molecular and periodic systems: An approach utilizing force. *Wiley Interdiscip. Rev. Comput. Mol. Sci.* **2021**, 11 (6), e1538. https://doi.org/10.1002/wcms.1538.

42. Maeda, S.; Taketsugu, T.; Morokuma, K. Exploring transition state structures for intramolecular pathways by the artificial force induced reaction method. *J. Comput. Chem.* **2013**, 35, 166–173. https://doi.org/10.1002/jcc.23481.

43. Sumiya, Y.; Maeda, S. A Reaction Path Network for Wöhler's Urea Synthesis. *Chem. Lett.* **2019**, 48, 47–50. https://doi.org/10.1246/cl.180850.

44. Sugiyama, K.; Sumiya, Y.; Takagi, M.; Saita, K.; Maeda, S.; Understanding CO oxidation on the Pt(111) surface based on a reaction route network. *Phys. Chem. Chem. Phys.* 2019, 21, 14366–14375. https://doi.org/10.1039/C8CP06856A.

45. Nabata, H.; Maeda, S. Systematic Search for Thermal Decomposition Pathways of Formic Acid on Anatase TiO_2 (101) Surface. *ChemCatChem* **2023**, 15, e2023007. https://doi.org/10.1002/cctc.202300752.

46. Hayashi, H.; Katsuyama, H.; Takano, H.; Harabuchi, Y.; Maeda, S.; Mita, T. In silico reaction screening with difluorocarbene for N-difluoroalkylative dearomatization of pyridines. *Nat. Synth.* **2022**, 1, 804–814. https://doi.org/10.1038/s44160-022-00128-y.

47. Bernardi, F.; Olivucci, Robb, M. M. A. Potential energy surface crossings in organic photochemistry. *Chem. Soc. Rev.* **1996**, 25, 321–328. https://doi.org/10.1039/cs9962500321.

48. Shiga, M.; Tachikawa, M.; Muira, S. A unified scheme for ab initio molecular orbital theory and path integral molecular dynamics. *J. Chem. Phys.* **2001**, 115, 9149–9159. https://doi.org/10.1063/1.1407289.

49. Carpenter, B.K. NONSTATISTICAL DYNAMICS IN THERMAL REACTIONS OF

POLYATOMIC MOLECULES. *Annu. Rev. Phys. Chem.* **2005**. 57–89. https://doi.org/10.1146/annurev.physchem.56.092503.141240.

50. Rehbein, J.; Carpenter, B. K. Do We Fully Understand What Controls Chemical Selectivity? *Phys. Chem. Chem. Phys.* **2011**, *13* (47), 20906–20922. https://doi.org/10.1039/c1cp22565k.

51. Oyola, Y.; Singleton, D. A. Dynamics and the Failure of Transition State Theory in Alkene Hydroboration. *J. Am. Chem. Soc.* **2009**, 131, 3130–3131. https://doi.org/10.1021/ja807666d.

52. Sun, L.; Song, K.; Hase, W. L. *Science* **2002**, 296, 875−878. https://doi.org/10.1126/science.1068053.

53. Ess, D. H.; Wheeler, S. E.; Iafe, R. G.; Xu, L.; Çelebi-Ölçüm, N.; Houk, K. N. Bifurcations on Potential Energy Surfaces of Organic Reactions. *Angew. Chem. Int. Ed. Engl.* **2008**, *47* (40), 7592–7601. https://doi.org/10.1002/anie.200800918.

54. Hare, S. R.; Tantillo, D. J. Post-Transition State Bifurcations Gain Momentum – Current State of the Field, *J. Pure Appl. Chem.* **2017**, *89* (6), 679-698. https://doi.org/10.1515/pac-2017-0104.

55. Valtazanos, P.; Ruedenberg, K. Bifurcations and Transition States. *Theoret Chim. Acta* **1986**, *69* (4), 281–307. https://doi.org/10.1007/BF00527705.

56. Baker, J.; Gill, P. M. W. An Algorithm for the Location of Branching Points on Reaction Paths. *J. Comput. Chem.* **1988**, *9* (5), 465–475. https://doi.org/10.1002/jcc.540090505.

57. Harabuchi, Y.; Taketsugu, T. A significant role of the totally symmetric valley-ridge inflection point in the bifurcating reaction pathway. *Theor. Chem. Acc.* **2011**, 130, 305−315.

https://doi.org/10.1007/s00214-011-0977-x.

58. Harabuchi, Y.; Ono, Y.; Maeda, S.; Taketsugu, T. Analyses of Bifurcation of Reaction Pathways on a Global Reaction Route Map: A Case Study of Gold Cluster Au_5. *J. Chem. Phys.* **2015**, *143* (1), 014301. https://doi.org/10.1063/1.4923163.

59. Taketsugu, T.; Tajima, N.; Hirao, K. Approaches to Bifurcating Reaction Path. *J. Chem. Phys.* **1996**, *105* (5), 1933–1939. https://doi.org/10.1063/1.472063.

60. Kumeda, Y.; Taketsugu, T. Isotope Effect on Bifurcating Reaction Path: Valley–Ridge Inflection Point in Totally Symmetric Coordinate. *J. Chem. Phys.* **2000**, *113* (2), 477–484. https://doi.org/10.1063/1.481826.

61. Taketsugu, T.; Kumeda, Y. An *Ab Initio* Direct-Trajectory Study of the Kinetic Isotope Effect on the Bifurcating Reaction. *J. Chem. Phys.* **2001**, *114* (16), 6973–6982. https://doi.org/10.1063/1.1358864.

62. Valtazanos, P.; Elbert, S. T.; Xantheas, S.; Ruedenberg, K. The Ring Opening of Cyclopropylidene to Allene: Global Features of the Reaction Surface. *Theoret Chim. Acta* **1991**, *78* (5–6), 287–326. https://doi.org/10.1007/BF01112344.

63. Yanai, T.; Taketsugu, T.; Hirao, K. Theoretical Study of Bifurcating Reaction Paths. *J. Chem. Phys.* **1997**, *107* (4), 1137–1146. https://doi.org/10.1063/1.474459.

64. Caramella, P.; Quadrelli, P.; Toma, L. An Unexpected Bispericyclic Transition Structure Leading to 4+2 and 2+4 Cycloadducts in the Endo Dimerization of Cyclopentadiene. *J. Am. Chem. Soc.* **2002**, *124* (7), 1130–1131. https://doi.org/10.1021/ja016622h.

65. Pham, H. V.; Houk, K. N. Diels–Alder Reactions of Allene with Benzene and Butadiene: Concerted, Stepwise, and Ambimodal Transition States. *J. Org. Chem.* **2014**, *79* (19), 8968–8976. https://doi.org/10.1021/jo502041f.

66. Houk, K. N.; Xue, X.-S.; Liu, F.; Chen, Y.; Chen, X.; Jamieson, C. Computations on Pericyclic Reactions Reveal the Richness of Ambimodal Transition States and Pericyclases. *Isr. J. Chem.* **2021**, *61*. https://doi.org/10.1002/ijch.202100071.

67. Limanto, J.; Khuong, K. S.; Houk, K. N.; Snapper, M. L. Intramolecular Cycloadditions of Cyclobutadiene with Dienes: Experimental and Computational Studies of the Competing (2 + 2) and (4 + 2) Modes of Reaction. *J. Am. Chem. Soc.* **2003**, *125* (52), 16310–16321. https://doi.org/10.1021/ja0380547.

68. Celebi-Olçüm, N.; Ess, D. H.; Aviyente, V.; Houk, K. N. Lewis Acid Catalysis Alters the Shapes and Products of Bis-Pericyclic Diels-Alder Transition States. *J. Am. Chem. Soc.* **2007**, *129* (15), 4528–4529. https://doi.org/10.1021/ja070686w.

69. Yu, P.; Chen, T. Q.; Yang, Z.; He, C. Q.; Patel, A.; Lam, Y. H.; Liu, C. Y.; Houk, K. N. Mechanisms and Origins of Periselectivity of the Ambimodal [6 + 4] Cycloadditions of Tropone

to Dimethylfulvene. *J. Am. Chem. Soc.* **2017**, *139* (24), 8251–8258. https://doi.org/10.1021/jacs.7b02966.

70. Chen, S.; Yu, P.; Houk, K. N. Ambimodal Dipolar/Diels–Alder Cycloaddition Transition States Involving Proton Transfers. *J. Am. Chem. Soc.* **2018**, *140* (51), 18124–18131. https://doi.org/10.1021/jacs.8b11080.

71. Xue, X.; Jamieson, C. S.; Garcia-Borràs, M.; Dong, X.; Yang, X.; Houk, K. N. Ambimodal Trispericyclic Transition State and Dynamic Control of Periselectivity. *J. Am. Chem. Soc.* **2019**, *141* (3), 1217–1221. https://pubs.acs.org/doi/10.1021/jacs.8b12674.

72. Liu, F.; Chen, Y.; Houk, K. N. Huisgen's 1,3-Dipolar Cycloadditions to Fulvenes Proceed via Ambimodal [6+4]/[4+2] Transition States. *Angew. Chem. Int. Ed. Engl.* **2020**, *59* (30), 12412–12416. https://doi.org/10.1002/anie.202005265.

73. Jamieson, C. S.; Sengupta, A.; Houk, K. N. Cycloadditions of Cyclopentadiene and Cycloheptatriene with Tropones: All *Endo*-[6+4] Cycloadditions Are Ambimodal. *J. Am. Chem. Soc.* **2021**, 143, 3918–3926. https://doi.org/10.1021/jacs.0c13401.

74. Zhang, H.; Novak, A. J. E.; Jamieson, C. S.; Xue, X. S.; Chen, S.; Trauner, D.; Houk, K. N. Computational Exploration of the Mechanism of Critical Steps in the Biomimetic Synthesis of Preuisolactone A, and Discovery of New Ambimodal (5 + 2)/(4 + 2) Cycloadditions. *J. Am. Chem. Soc.* **2021**, *143* (17), 6601–6608. https://doi.org/10.1021/jacs.1c01856.

75. Zhang, H.; Thøgersen, M. K.; Jamieson, C. S.; Xue, X.; Jørgensen, K. A.; Houk, K. N. Ambimoda lTransition States in Diels–Alder Cycloadditions of Tropolone and Tropolonate with *N*-Methylmaleimide. *Angew. Chem. Int. Ed.* **2021**, 60, 24991–24996. https://doi.org/10.1002/ange.202109608.

76. Martin-Somer, Ana.; Xue, X.; Jamieson, C. S.; Zou, Y.; Houk, K. N. Computational Design of a Tetrapericyclic Cycloaddition and the Nature of Potential Energy Surfaces with Multiple Bifurcations. *J. Am. Chem. Soc.* **2023**, *145* (7), 4221–4230. https://doi.org/10.1021/jacs.2c12871.

77. Sengupta, A.; Houk, K. N. Origins of Periselectivity and Regioselectivity in Ambimodal Tripericyclic [8+6]/[6+4]/[4+2] Intramolecular Cycloadditions of a Heptafulvenyl-Fulvene. J. Am. Chem. Soc. **2023**, 127, 7976–7983. https://doi.org/10.1021/acs.jpca.3c05656.

78. Ussing, B. R.; Hang, C.; Singleton, D. A. Dynamic Effects on the Periselectivity, Rate, Isotope Effects, and Mechanism of Cycloadditions of Ketenes with Cyclopentadiene. *J. Am. Chem. Soc.* **2006**, *128* (23), 7594–7607. https://doi.org/10.1021/ja0606024.

79. Thomas, J. B.; Waas, J. R.; Harmata, M.; Singleton, D. A. Control Elements in Dynamically Determined Selectivity on a Bifurcating Surface. *J. Am. Chem. Soc.* **2008**, *130* (44), 14544–14555. https://doi.org/10.1021/ja802577v.

80. Wang, Z.; Hirschi, J. S.; Singleton, D. A. Recrossing and Dynamic Matching Effects on Selectivity in a Diels-Alder Reaction. *Angew. Chem. Int. Ed. Engl.* **2009**, *48* (48), 9156–9159. https://doi.org/10.1002/anie.200903293.

81. Biswas, B.; Collins, S. C.; Singleton, D. A. Dynamics and a Unified Understanding of Competitive [2,3]- and [1,2]-Sigmatropic Rearrangements Based on a Study of Ammonium Ylides. *J. Am. Chem. Soc.* **2014**, 136, 3740–3743. https://doi.org/10.1021/ja4128289.

82. Biswas, B.; Singleton, D. A. Controlling Selectivity by Controlling the Path of Trajectories. *J. Am. Chem. Soc.* **2015**, 137, 14244–14247. https://doi.org/10.1021/jacs.5b08635.

83. Hong, Y. J.; Tantillo, D. J. A Potential Energy Surface Bifurcation in Terpene Biosynthesis. *Nat. Chem.* **2009**, *1* (5), 384–389. https://doi.org/10.1038/nchem.287.

84. Hong, Y. J.; Tantillo, D. J. Biosynthetic Consequences of Multiple Sequential Post-Transition-State Bifurcations. *Nat. Chem.* **2014**, *6* (2), 104–111. https://doi.org/10.1038/nchem.1843.

85. Katori, T.; Itoh, S.; Sato, M.; Yamataka, H. Reaction Pathways and Possible Path Bifurcation for the Schmidt Reaction, J. Am. Chem. Soc. **2010**, 132, 3413–3422. https://doi.org/10.1021/ja908899u.

86. Yamataka, H.; Sato, M.; Hasegawa, H.; Ammal, S. C. Dynamic path bifurcation for the Beckmann reaction: observation and implication. *Faraday Discuss.* **2010**, 145, 327–340. https://doi.org/10.1039/B906159B.

87. Yamamoto, Y.; Hasegawa, H.; Yamataka, H. Dynamic Path Bifurcation in the Beckmann

Reaction: Support from Kinetic Analyses. *J. Org. Chem.* **2011**, 76, 4652–4660. https://doi.org/10.1021/jo200728t.

88. Noey, E. L.; Wang, X.; Houk, K. N. Selective Gold(I)-Catalyzed Formation of Tetracyclic Indolines: A Single Transition Structure and Bifurcations Lead to Multiple Products. *J. Org. Chem.* **2011**, *76* (9), 3477–3483. https://doi.org/10.1021/jo200556f.

89. Wang, Z. J.; Benitez, D.; Tkatchouk, E.; Goddard, W. A.; Toste, F. D. Mechanistic Study of Gold(I)-Catalyzed Intermolecular Hydroamination of Allenes. *J. Am. Chem. Soc.* **2010**, 132, 13064–13071. https://doi.org/10.1021/ja105530q.

90. Li, B.; Li, Y.; Dang, Y.; Houk, K. N. Post-Transition State Bifurcation in Iron-Catalyzed Arene Aminations. *ACS Catal.* **2021**, 11, 6816–6824. https://doi.org/10.1021/acscatal.1c01291.

91. Kpante, M.; Wolf, L. M.; Pathway Bifurcations in the Activation of Allylic Halides by Palladium and Their Influence on the Dynamics of η^1 and η^3 Allyl Intermediates. *J. Org. Chem.* **2021**, 86, 9637–9650. https://doi.org/10.1021/acs.joc.1c00891.

92. Hare, S. R.; Tantillo, D. J. Cryptic post-transition state bifurcations that reduce the efficiency of lactone-forming Rh-carbenoid C–H insertions. *Chem. Sci.* **2017**, 8, 1442–1449. https://doi.org/10.1039/C6SC03745C.

93. Yu, P.; Patel, A.; Houk, K. N. Transannular [6 + 4] and Ambimodal Cycloaddition in the Biosynthesis of Heronamide A. *J. Am. Chem. Soc.* **2015**, 137, 13518–13523. https://doi.org/10.1021/jacs.5b06656.

94. Patel, A.; Chen, Z.; Yang, Z.; Gutiérrez, O.; Liu, H. W.; Houk, K. N.; Singleton, D. A. Dynamically Complex [6+4] and [4+2] Cycloadditions in the Biosynthesis of Spinosyn A. *J. Am. Chem. Soc.* **2016**, *138* (11), 3631–3634. https://doi.org/10.1021/jacs.6b00017.

95. Zou, Y.; Houk, K. N. Mechanisms and Dynamics of Synthetic and Biosynthetic Formation of Delitschiapyrones: Solvent Control of Ambimodal Periselectivity. *J. Am. Chem. Soc.* **2021**, *143* (30), 11734–11740. https://doi.org/10.1021/jacs.1c05293.

2. AFIR explorations of transition states of extended unsaturated systems: automatic location of ambimodal transition states

2.1 Introduction

The Diels-Alder reaction is one of the most important synthesis methods and has been utilized in vast chemical syntheses (1,2). Its transition state (TS) has also been studied extensively based on quantum chemical calculations (3). On the other hand, several groups have reported Diels-Alder reactions in which a phenomenon so-called dynamical bifurcation takes place (4,5). The dynamical bifurcation in the Diels-Alder reaction is the focus of this paper.

Theoretically, an elementary reaction step is defined as a path that connects a pair of two local minima via a single transition state (TS). These paths are commonly defined by the steepest descent path starting from a TS in the mass-weighted coordinates and called intrinsic reaction coordinate (IRC) (6,7). By calculating an IRC path, energetic and geometrical variations that occur in the corresponding reaction step can be elucidated.

2. Automated search for dynamical bifurcations

In most reactions, the IRC path well represents the mechanism of corresponding reaction. However, actual molecular motions deviate from the IRC path due to the kinetic energy, and there are known cases where the neglect of kinetic energy misleads an incorrect mechanism (8-10). The dynamical bifurcation is one of such cases (11-28). In a bifurcation reaction, a single TS relates to two products. In other words, a set of reactive trajectories passing the corresponding TS region branches into two components giving two different products. Such a TS is called an ambimodal TS.[5] Since an IRC calculation from a TS gives only a single product, the IRC calculation misses one of two products in bifurcation reactions (29).

Occurrence of bifurcation can be recognized by running *ab initio* molecular dynamics (AIMD) simulations starting from the corresponding TS region (30-53). Therefore, AIMD simulations have been performed to reveal bifurcations in reactions of various types such as organic reactions (30-35,37,38,43-45,47,49-57), organometallic reactions (41,58), and biosynthesis reactions (36,39,59-64). Occurrence of bifurcation can also be discussed through a static analysis of the potential energy surface (PES) by locating a valley-ridge transition (VRT) point along the IRC path. On a VRT point, the shape of PES perpendicular to the IRC path changes from the valley to the ridge (11,12,15,16,20,21,23,24,26,27). To find a VRT point, the curvature of PES needs to be computed at many points along the IRC path.

My purpose in this paper is to systematically explore TSs from which a dynamical bifurcation takes place. In the pioneering work by Hong and Tantillo (64), they applied AIMD simulations to various TSs in a reaction path network of terpene and discussed bifurcation reactions

on the network. To avoid running AIMD simulations from many TSs, Harabuchi et al. systematically explored VRT points by applying the curvature analysis along all IRC paths on a reaction path network of Au_5 cluster (65). Then, they applied AIMD simulations to only TSs from which a VRT point was obtained to identify products of corresponding bifurcation reactions. Although this approach allowed them to avoid AIMD simulations from many TSs, the curvature analysis done in their VRT search needs to compute Hessian matrix and is still demanding computationally.

My approach proposed here was inspired by results in early studies where two different products were obtained for the same TS depending on the choice of coordinate systems (22). Subsequent AIMD studies revealed that a dynamical bifurcation took place from the TS (50-52). In this discovery, use of paths of two different mathematical nature was the key. In other words, both of the two products were identified by computing two static paths with different mathematical nature. Maeda and Morokuma have developed an automated reaction path search method called artificial force induced reaction (AFIR) (66,67). The AFIR method traces a path so-called AFIR path because AFIR paths can be computed easily from a local minimum to the other local minimum. In the standard AFIR procedure, all obtained AFIR paths are further processed to obtain actual TSs. Therefore, my idea here is that two bifurcation products could be identified from differences between connections of AFIR paths and IRC paths. It is thus expected that this approach could suggest both occurrence and products of bifurcation reactions without any additional efforts after an automated reaction path search.

In this study, I explored paths of reactions between 2-vinylfuran and 3-

methoxycarbonylcyclopentadienone (see **scheme 2.1**) systematically by the multicomponent version of the AFIR method (MC-AFIR) (66). These two reactants are known to react to each other affording two Diels-Alder products. Furthermore, paths leading these two products are known to share a single TS and thus correspond to a bifurcation reaction. Moreover, this system has many reactive sites at which different competing Diels-Alder reactions can take place. Actually, the MC-AFIR search generated paths to sixty-five unique products, where these products were unique in terms of their SMILES representation. Among the sixty-five, sixteen corresponded to Diels-Alder products. As expected, I found many cases in which the reactants were linked to a product via only an AFIR path. In these cases, through a careful analysis of search logs of obtaining actual TSs, it was found that two AFIR paths shared a single TS region as the bottleneck. The further curvature analysis of IRC paths from these TSs identified six cases in which VRT points existed along the corresponding IRC paths. Finally, I proposed six bifurcation cases for this single reaction system.

Scheme 2.1. Diels-Alder cycloaddition reaction (33) between 2-vinylfuran and 3-methoxycarbonylcyclopentadienone.

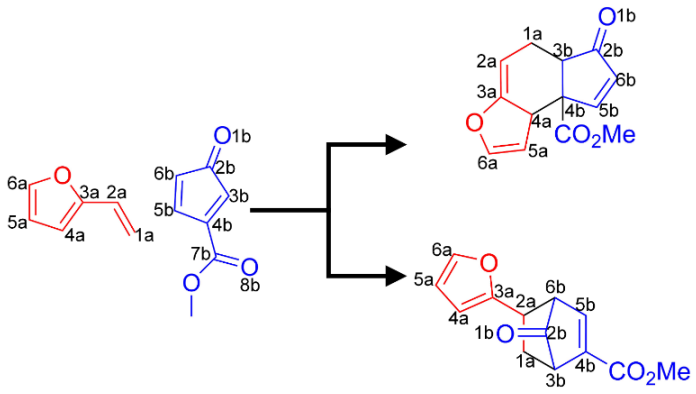

2.2 Theory

The AFIR method induces a structural deformation in a system by an artificial force and finds a path of chemical reaction from a local minimum to the other local minimum. The structural deformation can be induced by minimizing a function so-called AFIR function (66). Thanks to careful design of the form of AFIR function, paths that are obtained through its minimization pass TS regions that actual reaction paths pass (66,68). Therefore, the AFIR method first explores AFIR paths and finds TSs for various reactions by further processing the AFIR paths. Details how it systematically explores AFIR paths and how actual TSs are obtained from AFIR paths are described in the previous papers (66-69).

My idea or hypothesis proposed in this study is explained using a 2-dimensional model PES shown in **Figure 2.1**. On this PES, three local minima, **R**, **P1**, and **P2**, and two TSs, **T1** and **T2**, exist. Let's consider the process of finding paths to **P1** and **P2** by the AFIR method starting from **R**. In this case, the AFIR method finds these two products by adding artificial forces along different directions. The corresponding AFIR paths are depicted as white lines. These AFIR paths pass the **T1** region, and

further geometry optimizations starting from the highest energy points along these AFIR paths converge to **T1**. Finally, the IRC path is computed from **T1**. The IRC path from **T1** toward products' valley once approaches to **T2** and finally falls into **P1**'s well.

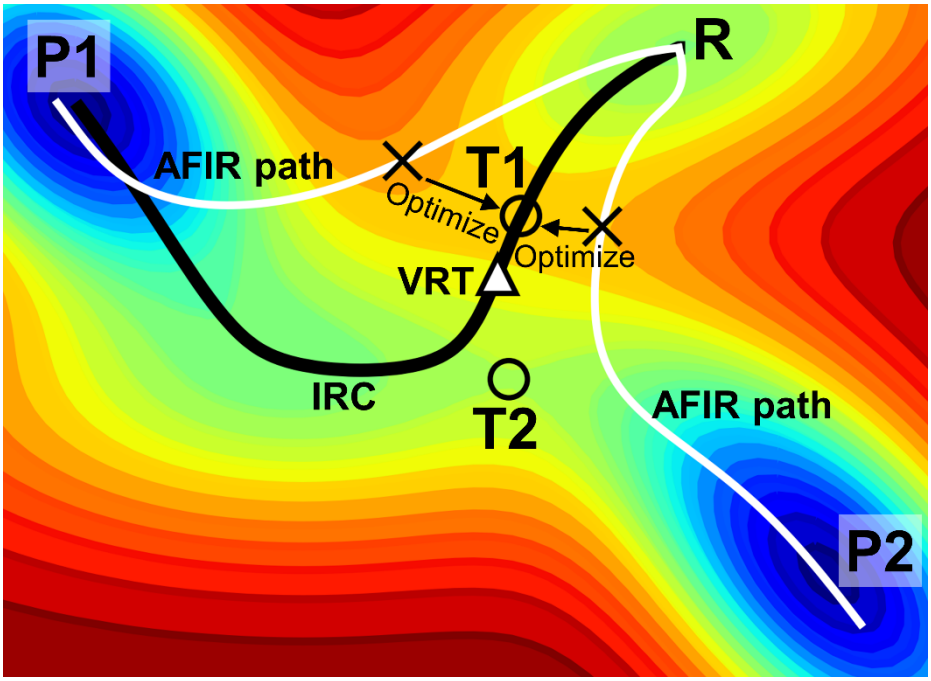

Figure 2.1. A schematic PES on which a reaction starting from a reactant MIN, R, reaches two different product MINs, P1 and P2. White lines indicate the AFIR paths, a black line indicates the IRC path, black circles indicate TSs, and a triangle indicate a VRT point.

In this case, two AFIR paths leading two different products provide a common TS. In other words, two AFIR paths share a single TS region. This situation suggests occurrence of the dynamical bifurcation. Actually, the VRT takes place along this IRC path. At **T1**, the curvature perpendicular to the IRC path is positive. On the other hand, the curvature decreases while approaching **T2** and

becomes negative around **T2**. As defined above, the point at which the curvature becomes negative from positive is called a VRT point.

In short, occurrence of dynamical bifurcations can be recognized by collecting cases where AFIR paths to different products provide a common TS. Furthermore, sets of products of these dynamical bifurcations can also be known as products of AFIR paths. This procedure is especially useful when the mechanism of the target reaction is unknown. In such a case, the automated search by the AFIR method is effective because the search systematically finds possible paths and help identifying the most probable mechanism. After the search, one can reveal both occurrence and products of possible dynamical bifurcations just by analyzing search logs without any additional quantum chemical calculations. In the actual application to the molecular system shown below, an additional procedure of relaxing the AFIR path was taken to avoid failure of TS optimization (see the computational details section for more description).

2.3 Computational Details

The AFIR paths between fragments A and B were computed starting from 1500 random mutual positions and orientations between 2-vinylfuran and 3-methoxycarbonylcyclopentadienone. The maximum model collision energy parameter, γ, was set to 1000 kJ mol-1. All the obtained AFIR paths were reoptimized using the LUP method (70), and the energy maxima along the relaxed AFIR paths were optimized to the actual TSs. From all obtained TSs, the IRC path was computed. These calculations were done at the ωB97X-D (71)/D95V level. AFIR paths passing the TS0 region were

further relaxed by the LUP method at the MPW1K/6-31+G** level to compare the results with those in the literature (33). 19 TSs which were shared by two AFIR paths giving products different in terms of SMILES representation were further optimized at the MPW1K/6-31+G** level. The IRC path was calculated for these 19 TSs at the MPW1K/6-31+G** level, and existence of a VRT point along the IRC path was examined through the curvature analysis using Hessian from which components along the gradient vector were eliminated (15). Energy, gradient, and Hessian were computed using the Gaussian 16 program package (72). AFIR, LUP, and IRC calculations were done using the developmental version of GRRM program (73). In this study, a post-processing code which automatically identifies candidates of ambimodal TSs was developed independently to the GRRM program.

2.4 Results

2.4.1 Analysis for one dynamical bifurcation

The Diels-Alder cycloaddition is a [4+2] cycloaddition reaction between a conjugated diene and dienophile. In this study, a case between 2-vinylfuran and 3-methoxycarbonylcyclopentadienone is studied (see **scheme 2.1**). For this reaction, occurrence of a bifurcation was previously reported (33). The reported bifurcation for this reaction gave two Diels-Alder products; one is the cycloaddition product composed of C3b, C4b, C5b, and C6b in cyclopentadienone and C1a and C2a in 2-vinylfuran (denoted by [C3b-C6b+C1a-C2a] type), and the other is that of C3b and C4b in cyclopentadienone and C1a, C2a, C3a, and C4a in 2-vinylfuran (denoted by [C1a-C4a+C3b-C4b]

type). In other words, a cyclopentadienone acts as diene in the case of [C3b-C6b+C1a-C2a] type, while 2-vinylfuran acts as diene in the case of [C1a-C4a+C3b-C4b] type. This type of bifurcation was called a bispericyclic reaction (4). Thus, fragment-A was set to C3b, C4b, C5b, and C6b in cyclopentadienone, and fragment-B is set to as C1a, C2a, C3a, and C4a in 2-vinylfuran.

The systematic AFIR search generated 134 product-MINs and 125 TSs automatically. The search found not only paths of [4+2] cycloaddition but also those of the other types such as [2+2] cycloaddition, [4+4] cycloaddition, [6+2] cycloaddition, and [6+4] cycloaddition. The obtained TSs are ordered in the ascending order of their energies and termed TSx (x = 0 ~ 124), where all energy values below are relative to the total energy of reactants. The lowest TS0 is for the [4+2] cycloaddition in **Scheme 2.1**. It was found that two AFIR paths shared TS0. These two AFIR paths lead to [C1a-C4a+C3b-C4b] and [C3b-C6b+C1a-C2a] products, respectively. This suggests that TS0 serves as a TS of bifurcation giving [C1a-C4a+C3b-C4b] and [C3b-C6b+C1a-C2a] products. This is consistent with the previous discovery summarized in **scheme 2.1** (33).

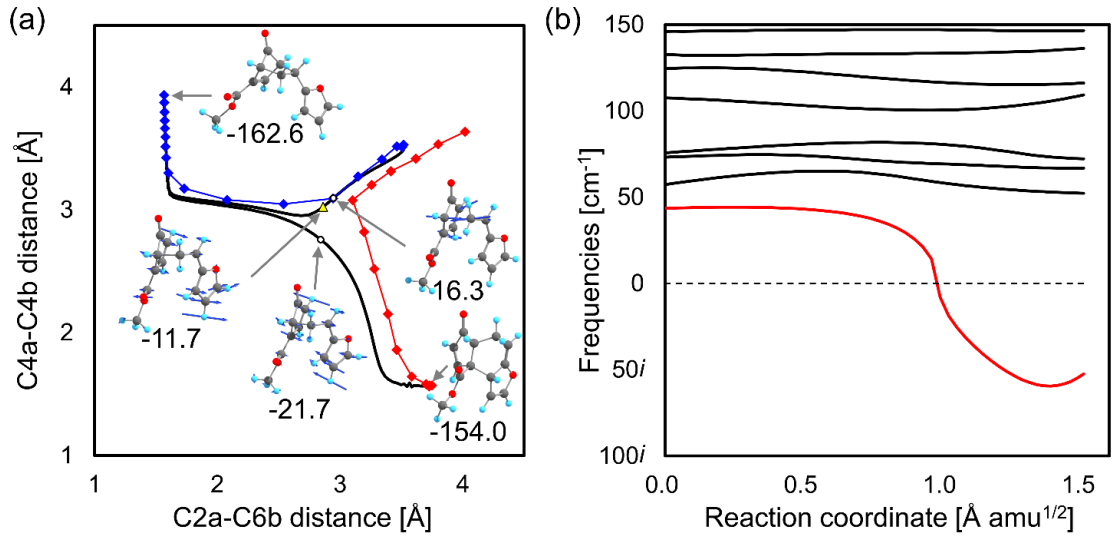

Figure 2.2. Analyses of AFIR paths and IRC paths. (a) shows a plot for C2a-C6b distance (*x*-axis) versus C4a-C4b distance (*y*-axis) along the IRC paths and the AFIR paths. Blue and red lines indicate AFIR paths, black lines indicate IRC paths, circles indicate TSs, and a triangle indicates a VRT point. Structures of TSs, MINs, and a VRT point are shown. Normal mode vectors corresponding to the negative eigenvalue mode at TSs and a VRT point are depicted. (b) shows the eight lowest vibrational frequencies of the modes perpendicular to the product side of the IRC path from s = 0.0 Å to 1.5 Å for TS0. Red line corresponds to the mode related to the dynamical bifurcation. All electronic energies are shown in kJ mol^{-1} relative to the set of reactants.

Figure 2.2a compares variations of two internal coordinates along the IRC path from TS0 with those along the two AFIR paths, where the AFIR paths shown in this figure were obtained by relaxing the initial AFIR paths of the low computational level by the final computational level (see computational details). Like the two-dimensional model shown in **Figure 2.1**, the AFIR method found

these two products. The corresponding AFIR paths depicted as blue and red lines passed the TS region, and further geometry optimizations starting from the highest energy points along these AFIR paths converged to the TS. The IRC path computed from the TS toward products' valley once approached to the TS between the two products and finally fell into the [C1a-C4a+C3b-C4b] product.

The VRT took place along this IRC path. **Figure 2.2b** shows variation of the eight lowest vibrational frequencies of the modes perpendicular to the IRC path from s = 0.0 Å to 1.5 Å. The negative eigenvalue mode (the red line) at the VRT point (see **Figure 2.2a**) is nearly parallel to the negative eigenvalue mode of the TS between the two products (see **Figure 2.2a**) and thus is related to the bifurcation. These results supported my idea shown in **Figure 2.1** and stimulated me to further study the other paths with the same idea.

2.4.2 Analysis for all dynamical bifurcations

Next, let's consider all [4+2] cycloaddition reactions that are assumable to occur between the diene and dienophile. There are eight combinations of diene and dienophile for [4+2] cycloaddition reactions; [C3b-C6b+C4a-C3a], [C3b-C6b+C3a-C4a], [C1a-C4a+C3b-C4b], [C1a-C4a+C4b-C3b], [C3b-C6b+C1a-C2a], [C3b-C6b+C2a-C1a], [C1a-C4a+C5b-C6b], [C1a-C4a+C6b-C5b]. All the eight patterns have endo-exo types, and thus, 16 unique [4+2] cycloadditions are expected in this system. These 16 patterns are listed in **Table 1**. As shown in **Figure 2.3a** and **2.3b**, when two dienes approach together during a Diels-Alder cycloaddition, both of [4+2] and [2+4] cycloadditions are expected. This is because both two dienes can act as the dienophile of the reaction.

In this case, the [4+2] and [2+4] cycloadditions sometimes pass through a common TS, i.e. bispericyclic reaction (4) (indicated by a [4+2]/[2+4] bispericyclic reaction). In **Table 2.1**, all the excepted [2+4] reactions which can be paired with the 16 [4+2] reactions as [4+2]/[2+4] bispericyclic reactions discussed above were listed in the row corresponding to each [4+2] cycloaddition reaction. It is mentioned that there are no excepted [4+2]/[2+4] bispericyclic reaction in entry-10, 12, 14, and 16 (indicated by N/A in **Table 2.1**). This is because these reactions are exo cycloaddition where dienophiles are terminal part of each molecule, C5b-C6b or C1a-C2a, and a diene part does not approach another diene part during the reaction. In addition, excepted [4+2]/[2+4] bispericyclic reactions of four entries, i.e. entry-1, 3, 5, and 11, are the same as those for entry-7, 13, 9, and 15. This is because both dienes are included in the two reactant molecules, and these were doubly counted. Actually, all the 16 [4+2] cycloaddition products were found by the present AFIR search.

Table 2.1. All the expected [4+2] cycloaddition reactions related to fragment-A and -B, i.e. C3b-C6b in cyclopentadienone and C1a-C4a in 2-vinylfuran, respectively. Pairs of diene and dienophile, orientations of endo or exo, indices of TSs, and energies of TSs in kJ mol^{-1} for each cycloaddition are indicated. The cycloadditions which can be paired with the 16 [4+2] cycloadditions as bispericyclic reactions, i.e. [2+4] cycloaddition and [6+4] cycloaddition, are shown in each row. "N/A" indicates a not-applicable case (see text).

	[4+2] cycloaddition					[2+4] cycloaddition				[6+4] cycloaddition			
Entry.	diene	dienophile		ΔE_S	TS	Diene	dienophile	ΔE_{TS}	TS	triene	Diene	ΔE_{TS}	TS
1[a]	C3b-C6b	C4a-C3a	endo	40.6	TS 8	C1a-C4a	C4b-C3b	35.3	TS 6	C1b-C6b	C6a-C3a	68.5	TS 37
2	C3b-C6b	C4a-C3a	exo	68.2	TS 35	C3a-C6a	C6b-C5b	51.4	TS 20	C1b-C3b	C1a-C4a	57.7	TS 22
3[c]	C3b-C6b	C3a-C4a	endo	59.7	TS 26	C1a-C4a	C5b-C6b	42.9	TS 10	C1b-C3b	C6a-C3a	59.7	TS 26
4	C3b-C6b	C3a-C4a	exo	50.5	TS 18	C3a-C6a	C3b-C4b	44.4	TS 11	C1b-C6b	C1a-C4a	85.6	TS 41
5[b]	C1a-C4a	C3b-C4b	endo	2.6	TS 0	C3b-C6b	C1a-C2a	2.6	TS 0	N/A	N/A	N/A	N/A
6	C1a-C4a	C3b-C4b	exo	23.3	TS 2	C3b-C8b	C1a-C2a	23.3	TS 2	N/A	N/A	N/A	N/A
7[a]	C1a-C4a	C4b-C3b	endo	35.3	TS 6	C3b-C6b	C4a-C3a	40.6	TS 8	N/A	N/A	N/A	N/A
8	C1a-C4a	C4b-C3b	exo	47.5	TS 15	C3b-C8b	C4a-C3a	47.5	TS 15	N/A	N/A	N/A	N/A
9[b]	C3b-C6b	C1a-C2a	endo	2.6	TS 0	C1a-C4a	C3b-C4b	2.6	TS 0	N/A	N/A	N/A	N/A
10	C3b-C6b	C1a-C2a	exo	25.7	TS 5	N/A	N/A	N/A	N/A	C1b-C3b	C4a-C1a	25.7	TS 5
11[d]	C3b-C6b	C2a-C1a	endo	24.5	TS 3	C1a-C4a	C6b-C5b	24.5	TS 3	N/A	N/A	N/A	N/A
12	C3b-C6b	C2a-C1a	exo	45.2	TS 12	N/A	N/A	N/A	N/A	C1b-C6b	C4a-C1a	45.2	TS 12
13[c]	C1a-C4a	C5b-C6b	endo	42.9	TS 10	C3b-C6b	C3a-C4a	59.7	TS 26	N/A	N/A	N/A	N/A
14	C1a-C4a	C5b-C6b	exo	64.9	TS 34	N/A	N/A	N/A	N/A	N/A	N/A	N/A	N/A
15[d]	C1a-C4a	C6b-C5b	endo	24.5	TS 3	C3b-C6b	C2a-C1a	24.5	TS 3	N/A	N/A	N/A	N/A
16	C1a-C4a	C6b-C5b	exo	63.7	TS 31	N/A	N/A	N/A	N/A	N/A	N/A	N/A	N/A

[a][2+4] and [4+2] cycloadditions of entry-1 correspond to [4+2] and [2+4] cycloadditions of entry-7, respectively. [b][2+4] and [4+2] cycloadditions of entry-3 correspond to [4+2] and [2+4] cycloadditions of entry-13, respectively. [c][2+4] and [4+2] cycloadditions of entry-5 correspond to [4+2] and [2+4] cycloadditions of entry-9, respectively. [d][2+4] and [4+2] cycloadditions of entry-11 correspond to [4+2] and [2+4] cycloadditions of entry-15, respectively.

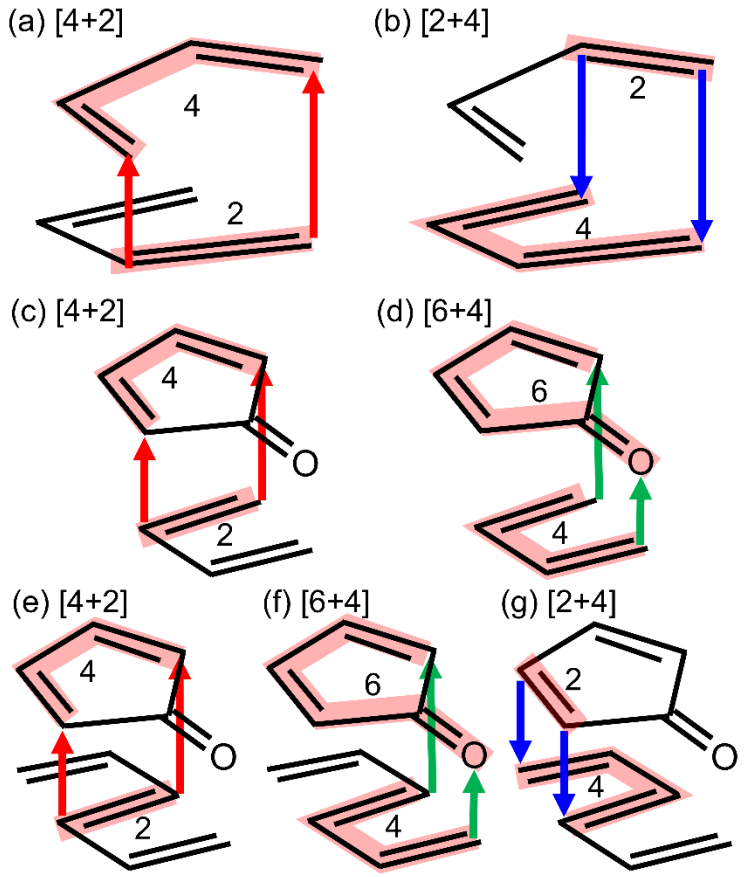

Figure 2.3. Schematic picture of bispericyclic bifurcations. (a) and (b) are for the case of [4+2]/[2+4] bispericyclic reactions. (c) and (d) are for [4+2]/[6+4] bispericyclic reactions. (e), (f) and (g) are for the case where both of [4+2]/[2+4] bispericyclic reactions or [4+2]/[6+4] bispericyclic reactions are expected.

Similarly, [4+2] and [6+4] cycloadditions sometimes pass through a common TS geometry, when a diene and a triene parts approach together during a [4+2] Diels-Alder cycloaddition like **Figure 2.3c** and **2.3d**. This type is indicated by a [4+2]/[6+4] bispericyclic reaction, and the expected [6+4] reactions are indicated in **Table 2.1**. In the four cases, i.e. entry-1, 2, 3, 4, 10 and 12, there were possibilities of [4+2]/[6+4] bispericyclic reaction. On the other hand, there was no candidate expected

for the other eight cases, because a diene in 2-vinylfuran does not approach triene in cyclopentadienone during the reaction of eight cases, which are indicated by N/A in **Table 2.1**. Actually, all the expected [6+4] products were also obtained by the present AFIR search.

In the results of the present search, a common TS region was shared by two AFIR paths in seven cases among the 16 bispericyclic reactions listed in **Table 2.1**. All the seven cases are indicated by a black flame in **Figure 2.4**. Entry-3, 10 and 12 correspond to [4+2]/[6+4] bispericyclic reactions, and entry-5 (equal to entry-9), 6, 8, and 11 (equal to entry-15) correspond to [4+2]/[2+4] bispericyclic reactions. On the other hand, two different TSs were found for a pair of AFIR paths for [4+2]/[6+4] bispericyclic pair of entry-1,2, and 4, and for [4+2]/[2+4] bispericyclic pair of entry-1,2,3 and 4. In the case of entry-3, [4+2]/[2+4] bispericyclic pair was not found, although that of [4+2]/[6+4] was found. This is explained by the absence of a common chemical bond generated during cycloaddition reactions. As shown in **Figure 2.3e**, **2.3f**, and **2.3g**, a common chemical bond is generated during [4+2] and [2+4] cycloadditions, and the situation is same for [4+2] and [6+4] cycloadditions. However, there is no common chemical bond generated during [2+4] and [6+4] cycloadditions, which makes their TSs different. In the cases of entry-1, 2, and 4, three AFIR path had the own TSs. This is explained based on the energy on TSs which connect two product minima. When a bifurcation occurs along a path from reactant-1 (denoted by R1) to product-1 (denoted by P1) and product-2 (denoted by P2), the TS connecting R1 to P1/P2 must be higher than the TS connecting P1 and P2. This is because a dynamical bifurcation leading to P1 and P2 takes place along a decent path from TS between R1 and P1/P2. In other words, a dynamical bifurcation does not occur when the TS between

P1 and P2 is higher than the TS between R1 and P1/P2. In the three cases of entry-1, 2, and 3, the TSs between products were higher than the lowest TS which connected the reactant and product. Thus, these are not cases of dynamical bifurcations. In short, there were the seven cases among the 16 bispericyclic reactions where the TS between P1 and P2 was lower than the TS between R1 to P1/P2, and, in the all the seven cases, a common TS region was shared by two AFIR paths.

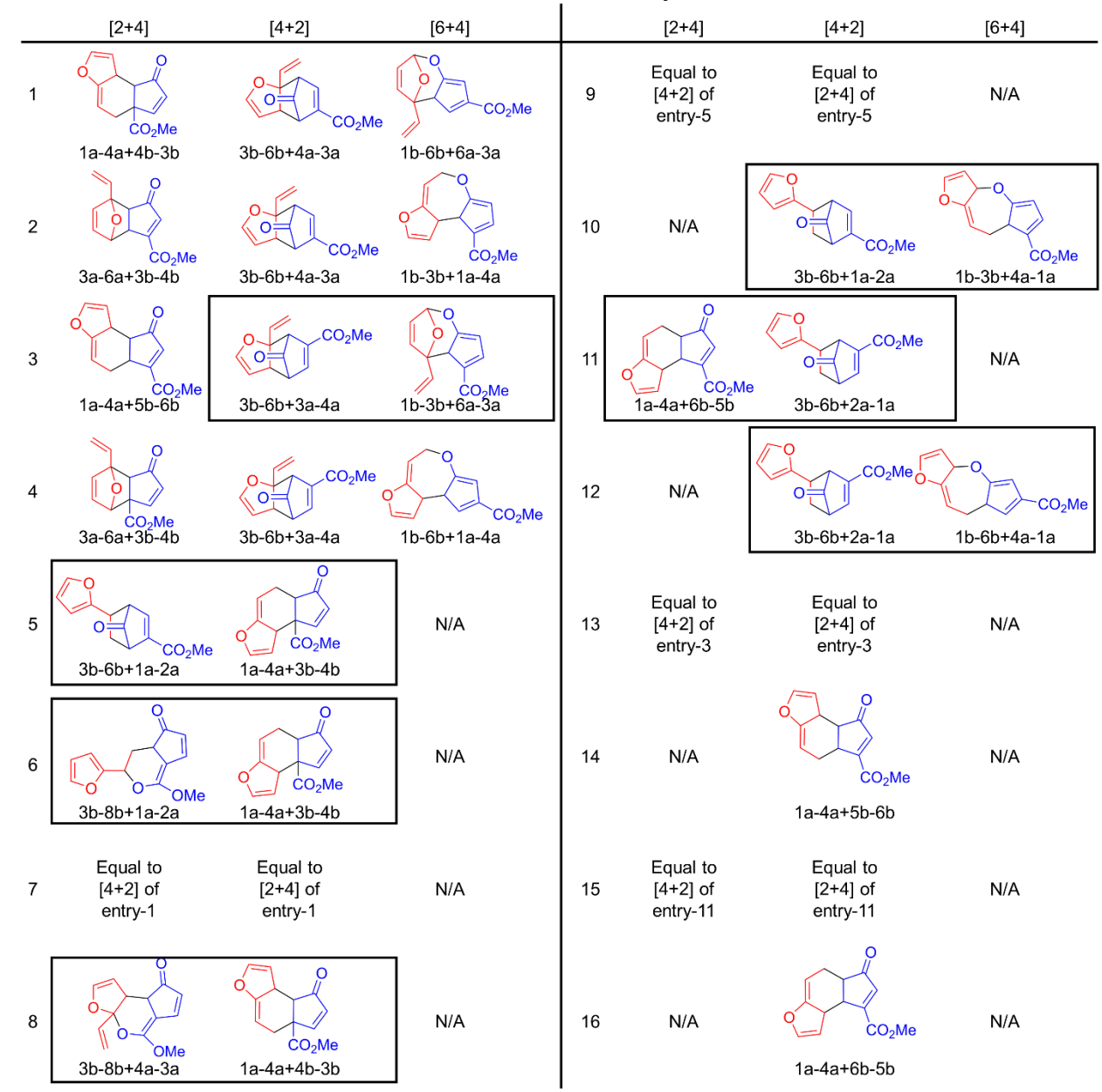

Figure 2.4. Expected [4+2] cycloaddition products for the target reaction. All the 16 [4+2] cycloaddition (Diels-Alder) products indicated in **Table 1** are shown. The obtained [2+4] and [6+4] cycloaddition products which can be paired with [4+2] cycloadditions as bispericyclic reactions are indicated in the corresponding row. Black frames indicate the cases where two AFIR paths to the products shared a common TS. "N/A" indicates a not-applicable case.

2. Automated search for dynamical bifurcations

Finally, all the obtained AFIR paths and TSs are summarized. In **Figure 2.5**, energies of all the obtained TSs in the search, i.e. 125 TSs, were plotted against the indices of atom pairs for each TS. Here, *i-j* indicates the atom pair with the shortest atom-atom distance between the two reactants on each TS. Red and green dashed line indicates a TS shared by two or more AFIR paths which gave products with different SMILES representations, and blue dotted line indicates that for the same SMILES representations. Black solid line indicates a TS for one AFIR path. Red dashed lines are for the cases when the VRT corresponding to the bifurcation was found along the IRC path, and green dashed line are for these without the VRT. All the structures for the obtained TSs are shown in the supporting information

Interestingly, there were 29 cases where a common TS was shared by two AFIR paths, and there were six cases where a common TS was shared by three AFIR paths. The latter case is related to a trifurcation reported in a previous study (28). Thus, totally 35 candidates of bifurcations were found in the present search. In 16 cases among the 35 cases, two different product minima had the same SMILES representations, which corresponds to the reactions giving conformationally different products. In 19 cases among the 35 cases, two different product minima had different bonding patterns. Among these 19 cases, there was the VRT corresponding to the bifurcation along the IRC path in six cases (indicated by red dashed lines in **Figure 2.5**). The TS geometries and the products of the six cases were depicted in ascending order of TS energies in **Figure 2.6**.

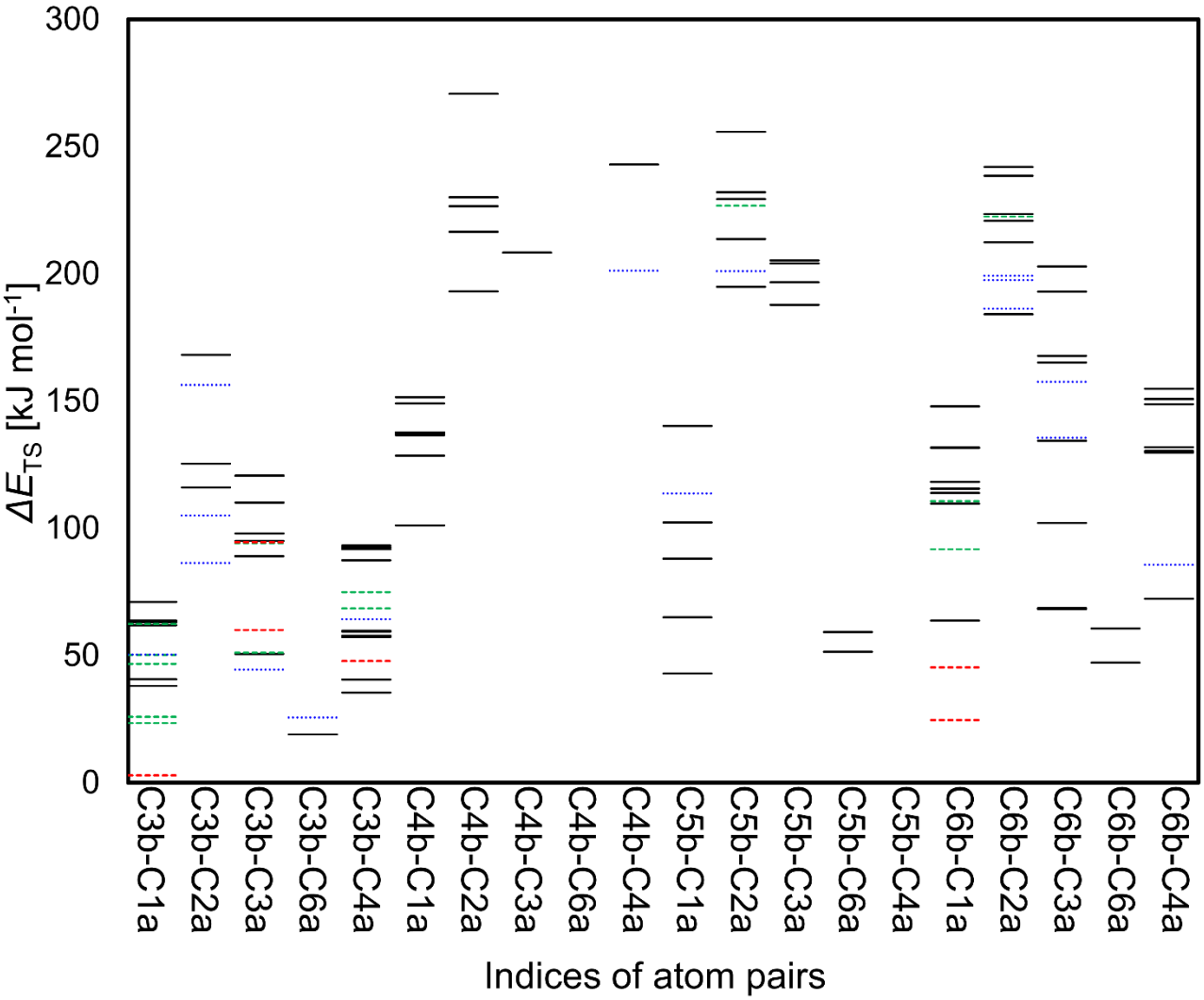

Figure 2.5. A plot of ΔE_{TS} against indices of the closest atom pairs on TSs. Black solid lines indicate TSs that one AFIR path passes through it. Blue dotted lines indicate TSs shared by two or more AFIR paths which gave products with the same SMILES representations. Green and red dashed lines indicate TSs shared by two or more AFIR paths which gave products with different SMILES representations. Red dashed lines indicate TSs with a VRT on its IRC path, and green dashed lines indicate TSs without any VRTs.

In **Figure 2.6**, in addition to the [4+2]/[2+4] bispericyclic reactions and [4+2]/[6+4]

bispericyclic reactions expected in **Table 2.1** (TS0, TS3, TS12, TS15, and TS26), the other one (TS51) was listed. The case of TS51 is a bifurcation to a [2+2] product and a [4+4] product, which has not been known previously. It is emphasized that the prediction of this bifurcation is not easy, but it was automatically obtained by using the present approach without using any prior knowledges of the reaction. These results demonstrate usefulness of the present approach to search for bifurcations.

As shown in **Figure 2.6**, for all the six cases, the TS energies, ΔE_{TS}, was lower than 110 kJ mol^{-1}. Also, the six cases correspond to the reaction in which the atom pair was composed by the terminal carbon atoms of a diene, C3b or C6b of cyclopentadienone, and C1a, C3a, C4a, or C6a of 2-vinylfuran. Thus, it is concluded that, in this system, the bifurcations accompany the bond formation between the terminal carbon atoms of the dienes.

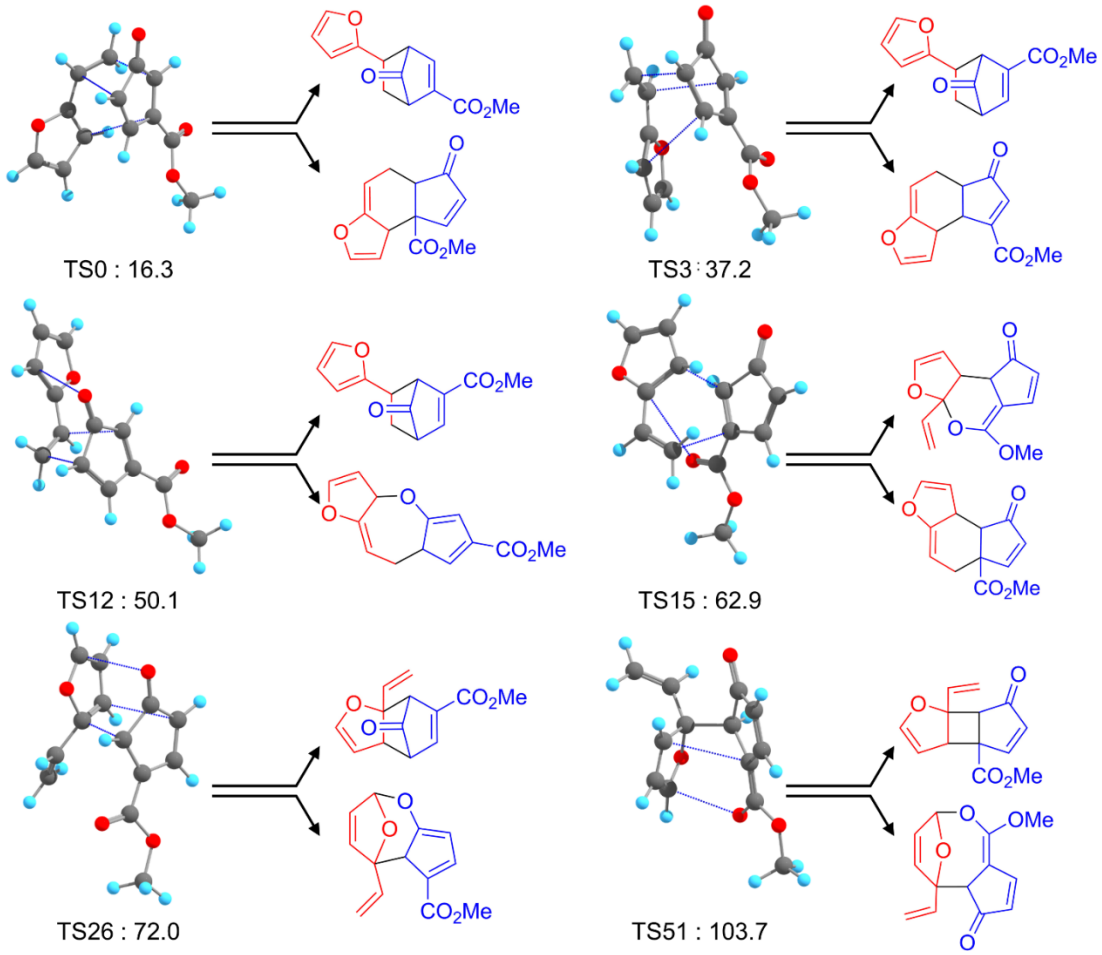

Figure 2.6. Six cases in which a common TS region was shared by two AFIR paths to reach two different product minima with different SMILES representations. In all the six cases, a VRT was found on the IRC path. Blue dotted line indicates the atom pair which makes the chemical bond during the reaction. TS energies are also indicated in kJ mol^{-1}.

2.5 Conclusion

In this study, paths of Diels-Alder reactions between 2-vinylfuran and 3-methoxycarbonylcyclopentadienone were systematically explored by the MC-AFIR method. This reaction is known to give two Diels-Alder products from a single TS region through the dynamical bifurcation (33). In this study, I proposed a procedure to systematically predict cases in which the

dynamical bifurcation occurs and applied it to the reaction. In this procedure, occurrence of the dynamical bifurcation is identified by collecting cases where AFIR paths to different products share a single TS region. The idea was inspired by an early study in which steepest descent paths computed in different coordinate systems led two different products of the dynamical bifurcation (22).

The present MC-AFIR search generated 125 TSs to 65 unique products. In addition to all possible [4+2] cycloaddition paths (Diels-Alder reactions), paths of the other cycloaddition types such as [2+2] cycloaddition, [4+4] cycloaddition, [6+2] cycloaddition, and [6+4] cycloaddition were also found. In 19 among all the 125 TSs, two AFIR paths shared a single TS region as the bottleneck and gave product minima different in terms of SMILES representation. Then, these 19 cases were further studied, and in 6 cases among the 19, a VRT point was found along the corresponding IRC path. Therefore, these six including the one reported in the literature (33) were proposed as TSs causing the dynamical bifurcation. The five new cases corresponded to two [4+2]/[2+4] bispericyclic reactions, two [4+2]/[6+4] bispericyclic reactions, and the other. The present procedure can find TSs causing dynamical bifurcations without using any prior knowledge on the target reaction and thus would be promising in future mechanistic studies on reactions involving dynamical bifurcations.

2.6 Reference

1. Diels, O.; Alder, K. Synthesen in der hydroaromatischen Reihe. *Justus Liebigs Ann. Chem.* **1928**, 460, 98–122. https://doi.org/10.1002/jlac.19284600106.

2. Nicolaou, K. C.; Snyder, S. A.; Montagnon, T.; Vassilikogiannakis, G. The Diels–Alder Reaction

in Total Synthesis. *Angew. Chem. Int. Ed.* **2002**, 41, 1668–1698. https://doi.org/10.1002/1521-3773(20020517)41:10<1668::AID-ANIE1668>3.0.CO;2-Z.

3. Ess, D. H.; Jones, G. O.; Houk, K. N. Conceptual, Qualitative, and Quantitative Theories of 1,3-Dipolar and Diels–Alder Cycloadditions Used in Synthesis. *Adv. Synth. Catal.* 2006, **348**, 2337–2361. https://doi.org/10.1002/adsc.200600431.

4. Caramella, P.; Quadrelli, P.; Toma, L. An Unexpected Bispericyclic Transition Structure Leading to 4+2 and 2+4 Cycloadducts in the Endo Dimerization of Cyclopentadiene . *J. Am. Chem. Soc.* **2002**, 124, 1130–1131. https://doi.org/10.1021/ja016622h.

5. Yang, Z.; Dong, X.; Yu, Y.; Yu, P.; Li, Y.; Jamieson, C.; Houk, K. N. Relationships between Product Ratios in Ambimodal Pericyclic Reactions and Bond Lengths in Transition Structures. *J. Am. Chem. Soc.* **2018**, 140, 3061−3067. https://doi.org/10.1021/jacs.7b13562.

6. Fukui, K. The path of chemical reactions - the IRC approach. *Acc. Chem. Res.* **1981**, 14, 363−368. https://doi.org/10.1021/ar00072a001.

7. Maeda, S.; Harabuchi, Y.; Ono, Y.; Taketsugu, T.; Morokuma, K. Intrinsic reaction coordinate: Calculation, bifurcation, and automated search. *Int. J. Quantum Chem.* **2015**, 115, 258−269. https://doi.org/10.1002/qua.24757.

8. Sun, L.; Song, K.; Hase, W. L. A S_N2 Reaction That Avoids Its Deep Potential Energy Minimum. *Science* **2002**, 296, 875−878. https://doi.org/10.1126/science.1068053.

9. Carpenter, B. K. NONSTATISTICAL DYNAMICS IN THERMAL REACTIONS OF POLYATOMIC MOLECULES. *Ann. Rev. Phys. Chem.* **2005**, 56, 57−79.

https://doi.org/10.1146/annurev.physchem.56.092503.141240.

10. Ess, D. H.; Wheeler, S. E.; Iafe, R. G.; Xu, L.; Çelebi-Ölçüm, N.; Houk, K. N.; *Angew. Chem. Int. Ed.* **2008**, 47, 7592–7601. https://doi.org/10.1002/anie.200800918.
11. Tachibana, A.; Okazaki, I.; Koizumi, M.; Hori, K.; Yamabe, T. Bifurcations on Potential Energy Surfaces of Organic Reactions. *J. Am. Chem. Soc.* **1985**, 107, 1190–1196. https://doi.org/10.1021/ja00291a018.
12. Valtazanos, P.; Ruedenberg, K. Bifurcations and transition states. *Theoret. Chim. Acta* **1986**, 69, 281–307. https://doi.org/10.1007/BF00527705.
13. Basilevsky, M. V. The structural stability principle and branching points on multidimensional potential energy surfaces. *Theor. Chim. Acta* **1987**, 72, 63–67. https://doi.org/10.1007/BF00526555.
14. Quapp, W. Gradient extremals and valley floor bifurcations on potential energy surfaces. *Theor. Chim. Acta* **1989**, 75, 447–460. https://doi.org/10.1007/BF00527676.
15. Baker, J.; Gill, P. M. W.; An algorithm for the location of branching points on reaction paths. *J. Comput. Chem.* **1988**, 9, 465–475. https://doi.org/10.1002/jcc.540090505.
16. Valtazanos, P.; Elbert, S. T.; Xantheas, S.; Ruedenberg, K. The ring opening of cyclopropylidene to allene: global features of the reaction surface. *Theoret. Chim. Acta* 1991, **78**, 287–326. https://doi.org/10.1007/BF01112344.
17. Taketsugu, T.; Hirano, T. Mechanism of bifurcation along the reaction path: An application in the case of thioformaldehyde. *J. Chem. Phys.* **1993**, 99, 9806–9814.

https://doi.org/10.1063/1.465462.

18. Taketsugu, T.; Hirano, T. Bifurcation analysis in terms of second-order Jahn—Teller effect. *J. Mol. Struct.: THEOCHEM* **1994**, 116, 169–176. https://doi.org/10.1016/S0022-2860(10)80067-5.

19. Sastry, G. N.; Shaik, S. Structured Electron Transfer Transition State. Valence Bond Configuration Mixing Analysis and ab Initio Calculations of the Reactions of Formaldehyde Radical Anion with Methyl Chloride . *J. Phys. Chem.* **1996**, 100, 12241–12252. https://doi.org/10.1021/jp952827z.

20. Taketsugu, T.; Tajima, N.; Hirao, K. Approaches to bifurcating reaction path. *J. Chem. Phys.* **1996**, 105, 1933–1939. https://doi.org/10.1063/1.472063.

21. Yanai, T.; Taketsugu, T.; Hirao, K. *J. Chem. Phys.* Theoretical study of bifurcating reaction paths. **1997**, 107, 1137–1146. https://doi.org/10.1063/1.474459.

22. Shaik, S.; Danovich, D.; Sastry, G. N.; Ayala, P. Y.; Schlegel, H. B. Dissociative Electron Transfer, Substitution, and Borderline Mechanisms in Reactions of Ketyl Radical Anions. Differences and Difficulties in Their Reaction Paths. *J. Am. Chem. Soc.* **1997**, 119, 9237–9245. https://doi.org/10.1021/ja971105d.

23. Taketsugu, T.; Yanai, T.; Hirao, K.; Gordon, M. S. Dynamic Reaction Path Study of $SiH_4+H^- \rightarrow SiH_5^-$ and the Berry Pseudorotation Mechanism. *J. Mol. Struct.: THEOCHEM* **1998**. 451, 163–177. https://doi.org/10.1021/j100040a005.

24. Kumeda, Y.; Taketsugu, Isotope effect on bifurcating reaction path: Valley–ridge inflection point

in totally symmetric coordinate. T. *J. Chem. Phys*. **2000**, 113, 477–484. https://doi.org/10.1063/1.481826.

25. Taketsugu, T.; Kumeda, Y. An *ab initio* direct-trajectory study of the kinetic isotope effect on the bifurcating reaction*J. Chem. Phys*. **2001**, 114, 6973–6982. https://doi.org/10.1063/1.1358864.
26. Quapp, W.; How does a reaction path branching take place? A classification of bifurcation events. *J. Mol. Struct.*, **2004**, 695–696, 95–101. https://doi.org/10.1016/j.molstruc.2003.10.034.
27. Bofill, J. M.; Quapp, W. Analysis of the Valley-Ridge inflection points through the partitioning technique of the Hessian eigenvalue equation. *J. Math. Chem.* **2013**, 51, 1099–1115. https://doi.org/10.1007/s10910-012-0134-3.
28. Harabuchi, Y.; Ono, Y.; Maeda, S.; Taketsugu, T.; Keipert, K.; Gordon, M. S. Nontotally symmetric trifurcation of an S_N2 reaction pathway. *J. Comput. Chem.* **2016**, 37, 487−493. https://doi.org/10.1002/jcc.24241.
29. Harabuchi, Y.; Taketsugu, T. A significant role of the totally symmetric valley-ridge inflection point in the bifurcating reaction pathway. *Theor. Chem. Acc.* **2011**, 130, 305−315. https://doi.org/10.1007/s00214-011-0977-x.
30. Bekele, T.; Christian, C. F.; Lipton, M. A.; Singleton, D. A. "Concerted" Transition State, Stepwise Mechanism. DynamicsEffects in C^2-C^6 Enyne Allene Cyclizations. *J. Am. Chem. Soc.*, **2005**, 127, 9216−9223. https://doi.org/10.1021/ja0508673.
31. Li, J.; Shaik, S.; Schlegel, H. B. A Single Transition State Serves Two Mechanisms. The Branching Ratio for $CH2O^{\bullet-}$ + CH3Cl on Improved Potential Energy Surfaces. *J. Phys. Chem. A*

2006, 110, 2801−2806. https://doi.org/10.1021/jp0563336.

32. Ussing, B. R.; Hang, C.; Singleton, D. A. Dynamic Effects on the Periselectivity, Rate, Isotope Effects, and Mechanism of Cycloadditions of Ketenes with Cyclopentadiene. *J. Am. Chem. Soc.* **2006**, 128, 7594−7607. https://doi.org/10.1021/ja0606024.

33. Thomas, J. B.; Waas, J. R.; Harmata, M.; Singleton, D. A. Control Elements in Dynamically Determined Selectivity on a Bifurcating Surface. *J. Am. Chem. Soc.* **2008**, 130, 14544−14555. https://doi.org/10.1021/ja802577v.

34. Kelly, K. K.; Hirschi, J. S.; Singleton, D. A. *J. Am. Chem. Soc.* **2009**, 131, 8382−8383. https://doi.org/10.1021/ja9031083.

35. Wang, Z.; Hirschi, J. S.; Singleton, D. A. Newtonian Kinetic Isotope Effects. Observation, Prediction, and Origin of Heavy-Atom Dynamic Isotope Effects. *Angew. Chem. Int*. **2009**, 121, 9320−9323. https://doi.org/10.1002/anie.200903293.

36. Siebert, M. R.; Zhang, J.; Addepalli, S. V.; Tantillo, D. J.; Hase, W. L. The Need for Enzymatic Steering in Abietic Acid Biosynthesis: Gas-Phase Chemical Dynamics Simulations of Carbocation Rearrangements on a Bifurcating Potential Energy Surface. *J. Am. Chem. Soc.* **2011**, 133, 8335−8343. https://doi.org/10.1021/ja201730y.

37. Bogle, X. S.; Singleton, D. A. Dynamic Origin of the Stereoselectivity of a Nucleophilic Substitution Reaction. *Org. Lett.* **2012**, 14, 2528−2531. https://doi.org/10.1021/ol300817a.

38. Gonzalez-James, O. M.; Kwan, E. E.; Singleton, D. A. Entropic Intermediates and Hidden Rate-Limiting Steps in Seemingly Concerted Cycloadditions. Observation, Prediction, and Origin of

an Isotope Effect on Recrossing. *J. Am. Chem. Soc.* **2012**, 134, 1914−1917. https://doi.org/10.1021/ja208779k.

39. Patel, A.; Chen, Z.; Yang, Z.; Gutiérrez, O.; Liu, H. Houk, K. N.; Singleton, D. A. Dynamically Complex [6+4] and [4+2] Cycloadditions in the Biosynthesis of Spinosyn A. *J. Am. Chem. Soc.* **2016**, 138, 3631−3634. https://doi.org/10.1021/jacs.6b00017.
40. Martín-Sómer, A.; Yáñez, M.; Hase, W. L.; Gaigeot, M.; Spezia, R. Post-Transition State Dynamics in Gas Phase Reactivity: Importance of Bifurcations and Rotational Activation. *J. Chem. Theory Comput.*, 2016, **12**, 974−982. https://doi.org/10.1021/acs.jctc.5b01135.
41. Hare, S. R.; Tantillo, D. J. Cryptic post-transition state bifurcations that reduce the efficiency of lactone-forming Rh-carbenoid C–H insertions. *Chem. Sci.* **2017**, 8, 1442–1449. https://doi.org/10.1039/C6SC03745C.
42. Hare, S. R.; Pemberton, R. P.; Tantillo, D. J. Navigating Past a Fork in the Road: Carbocation−π Interactions Can Manipulate Dynamic Behavior of Reactions Facing Post-Transition-State Bifurcations. *J. Am. Chem. Soc.* **2017**, 139, 7485–7493. https://doi.org/10.1021/jacs.7b01042.
43. Noey, E. L.; Yang, Z.; Li, Y.; Yu, H.; Richey, R. N.; Merritt, J. M.; Kjell, D. P.; Houk, K. N. Origins of Regioselectivity in the Fischer Indole Synthesis of a Selective Androgen Receptor Modulator. *J. Org. Chem.* **2017**, 82, 5904−5909. https://doi.org/10.1021/acs.joc.7b00878.
44. Yu, P.; Chen, T. Q.; Yang, Z.; He, C. Q.; Patel, A.; Lam, Y.; Liu, C.; Houk, K. N. Mechanisms and Origins of Periselectivity of the Ambimodal [6 + 4] Cycloadditions of Tropone to Dimethylfulvene. *J. Am. Chem. Soc.* **2017**, 139, 8251−8258.

https://doi.org/10.1021/jacs.7b02966.

45. Hare, S. R.; Li, A.; Tantillo, D. J. Post-transition state bifurcations induce dynamical detours in Pummerer-like reactions. *Chem. Sci.* **2018**, 9, 8937–8945. https://doi.org/10.1039/C8SC02653J.

46. Yang, Z.; Zou, L.; Yu, Y.; Liu, F.; Dong, X.; Houk, K. N.; *Chem. Phys.* **2018**, 514, 120–125. https://doi.org/10.1016/j.chemphys.2018.02.020.

47. Xue, X.; Jamieson, C. S.; Garcia-Borràs, M.; Dong, X.; Yang, Z.; Houk, K. N. Molecular dynamics of the two-stage mechanism of cyclopentadiene dimerization: concerted or stepwise?. *J. Am. Chem. Soc.* **2019**, 141, 1217–1221. https://doi.org/10.1021/jacs.8b12674.

48. Yang, Z.; Jamieson, C. S.; Xue, X.; Garcia-Borràs, M.; Benton, T.; Dong, X.; Liu, F.; Houk, K.N. Mechanisms and Dynamics of Reactions Involving Entropic Intermediates. *Tre. Chem.* **2019**, 1, 22–34. https://doi.org/10.1016/j.trechm.2019.01.009.

49. Campos, R. B.; Tantillo, D. J. *Chem* Designing Reactions with Post-Transition-State Bifurcations: Asynchronous Nitrene Insertions into C–C σ Bonds. **2019**, 5, 227–236. https://doi.org/10.1016/j.chempr.2018.10.019.

50. Yamataka, H.; Aida, M.; Dupuis, M. One transition state leading to two product states: ab initio molecular dynamics simulations of the reaction of formaldehyde radical anion and methyl chloride. *Chem. Phys. Lett.* **1999**, 300, 583–587. https://doi.org/10.1016/S0009-2614(98)01440-7.

51. Bakken, V.; Danovich, D.; Shaik, S.; Schlegel, H. B.; *J. Am. Chem. Soc.* A Single Transition State Serves Two Mechanisms: An ab Initio Classical Trajectory Study of the Electron Transfer and

Substitution Mechanisms in Reactions of Ketyl Radical Anions with Alkyl Halides. **2001**, 123, 130–134. https://doi.org/10.1021/ja002799k.

52. Li, J.; Li, X.; Shaik, S.; Schlegel, H. B. Single Transition State Serves Two Mechanisms. Ab Initio Classical Trajectory Calculations of the Substitution−Electron Transfer Branching Ratio in $CH2O^{\bullet-}$ + CH3Cl. *J. Phys. Chem. A* **2004**, 108, 8526–8532. https://doi.org/10.1021/jp046827n.
53. Bekele, T.; Christian, C. F.; Lipton, M. A.; Singleton, D. A. Dynamic Effects on the Periselectivity, Rate, Isotope Effects, and Mechanism of Cycloadditions of Ketenes with Cyclopentadiene. *J. Am. Chem. Soc.*, **2005**, 127, 9216–9223. https://doi.org/10.1021/ja0606024.
54. Singleton, D. A.; Hang, C.; Szymanski, M. J.; Meyer, M. P.; Leach, A. G.; Kuwata, K. T.; Chen, J. S.; Greer, A.; Foote, C. S.; Houk, K. N. Mechanism of Ene Reactions of Singlet Oxygen. A Two-Step No-Intermediate Mechanism. *J. Am. Chem. Soc.* **2003**, 125, 1319–1328. https://doi.org/10.1021/ja027225p.
55. Limanto, J.; Khuong, K. S.; Houk, K. N.; Snapper, M. L. Intramolecular Cycloadditions of Cyclobutadiene with Dienes: Experimental and Computational Studies of the Competing (2 + 2) and (4 + 2) Modes of Reaction. *J. Am. Chem. Soc.* **2003**, 125, 16310–16321. https://doi.org/10.1021/ja0380547.
56. Çelebi-Ölçüm, N.; Ess, D. H., Aviyente, V.; Houk, K. N. Lewis Acid Catalysis Alters the Shapes and Products of Bis-Pericyclic Diels−Alder Transition States. *J. Am. Chem. Soc.* **2007**, 129, 4528–4529. https://doi.org/10.1021/ja070686w.
57. Pham, H. V.; Houk, K. N. Diels–Alder Reactions of Allene with Benzene and Butadiene:

Concerted, Stepwise, and Ambimodal Transition States. *J. Org. Chem.* **2014**, 79, 8968−8976. https://doi.org/10.1021/jo502041f.

58. Noey, E. L.; Wang, X.; Houk, K. N. Selective Gold(I)-Catalyzed Formation of Tetracyclic Indolines: A Single Transition Structure and Bifurcations Lead to Multiple Products. *J. Org. Chem.* **2011**, 76, 3477–3483. https://doi.org/10.1021/jo200556f.

59. Hong, Y. J.; Tantillo, D. J. A potential energy surface bifurcation in terpene biosynthesis. *Nat. Chem.* **2009**, 1, 384–389. https://doi.org/10.1038/nchem.287.

60. Hong, Y. J.; Tantillo, D. J. Quantum chemical dissection of the classic terpinyl/pinyl/bornyl/camphyl cation conundrum—the role of pyrophosphate in manipulating pathways to monoterpenes. *Org. Biomol. Chem.* **2010**, 8, 4589–4600. https://doi.org/10.1039/c0ob00167h.

61. Tantillo, D. J. Biosynthesisvia carbocations: Theoretical studies on terpene formation. *Nat. Prod. Rep.* **2011**, 28, 1035–1053. https://doi.org/10.1039/c1np00006c.

62. Hong, Y. J.; Irmisch, S.; Wang, S. C.; Garms, S.; Gershenzon, J.; Zu, L.; Kçllner, T. G.; Tantillo, D. J. Theoretical and Experimental Analysis of the Reaction Mechanism of MrTPS2, a Triquinane-Forming Sesquiterpene Synthase from Chamomile. *Chem. Eur. J.* 2013, **19**, 13590–13600. https://doi.org/10.1002/chem.201301018.

63. Pemberton, R. P.; Hong, Y. J.; Tantillo, D. J. Inherent dynamical preferences in carbocation rearrangements leading to terpene natural products. *Pure Appl. Chem.* **2013**, 85, 1949–1957. https://doi.org/10.1351/pac-con-12-11-22.

64. Hong, Y. J.; Tantillo, D. J. Biosynthetic consequences of multiple sequential post-transition-state bifurcations. *Nat. Chem.* **2014**, 6, 104-111. https://doi.org/10.1038/nchem.1843.

65. Harabuchi, Y.; Ono, Y.; Maeda, S.; Taketsugu, T. Analyses of bifurcation of reaction pathways on a global reaction route map: A case study of gold cluster Au_5. *J. Chem. Phys.*, 2015, **143**, 014301. https://doi.org/10.1063/1.4923163.

66. Maeda, S.; Morokuma, K. *J. Chem. Phys.* **2010**, 132, 241102. https://doi.org/10.1063/1.3457903.

67. Maeda, S.; Harabuchi, Y.; Takagi, M.; Taketsugu, T.; Morokuma, K. *Chem. Rec.* **2016**, 16, 2232–2248. https://doi.org/10.1002/tcr.201600043.

68. Maeda, S.; Morokuma, K. Communications: A systematic method for locating transition structures of A + B →X type reactions. *J. Chem. Theory Comput*. **2011**, 7, 2335–2345. https://doi.org/10.1021/ct200290m.

69. Maeda, S.; Harabuchi, Y.; Takagi, M.; Saita, K.; Suzuki, K.; Ichino, T.; Sumiya, Y.; Sugiyama, K.; Ono, Y. Implementation and performance of the artificial force induced reaction method in the GRRM17 program. *J. Comput. Chem.* **2018**, 39, 233–250. https://doi.org/10.1002/jcc.25106.

70. Choi, C.; Elber, R. Reaction path study of helix formation in tetrapeptides: Effect of side chains. *J. Chem. Phys.* **1991**, 94, 751–760. https://doi.org/10.1063/1.460343.

71. Chai, J. D.; Head-Gordon, M. Long-range corrected hybrid density functionals with damped atom–atom dispersion corrections. *Phys. Chem. Chem. Phys.* **2008**, 10, 6615–6620. https://doi.org/10.1039/B810189B.

72. Frisch, M. J.; Trucks, G. W.; Schlegel, H. B.; Scuseria, G. E.; Robb, M. A.; Cheeseman, J. R.; Scalmani, G.; Barone, V.; Petersson, G. A.; Nakatsuji, H.; Li, X.; Caricato, M.; Marenich, A. V.; Bloino, J.; Janesko, B. G.; Gomperts, R.; Mennucci, B.; Hratchian, H. P.; Ortiz, J. V.; Izmaylov, A. F.; Sonnenberg, J. L.; Williams, Y. D.; Ding F.; Lipparini, F.; Egidi, F.; Goings, J.; Peng, B.; Petrone, A.; Henderson, T.; Ranasinghe, D.; Zakrzewski, V. G.; Gao, J.; Rega, N.; Zheng, G.; Liang, W.; Hada, M.; Ehara, M.; Toyota, K.; Fukuda, R.; Hasegawa, J.; Ishida, M.; Nakajima, T.; Honda, Y.; Kitao, O.; Nakai, H.; Vreven, T.; Throssell, K.; Montgomery Jr., J. A.; Peralta, J. E.; Ogliaro, F.; Bearpark, M. J.; Heyd, J. J.; Brothers, E. N.; Kudin, K. N.; Staroverov, V. N.; Keith, T. A.; Kobayashi, R.; Normand, J.; Raghavachari, K.; Rendell, A. P.; Burant, J. C.; Iyengar, S. S.; Tomasi, J.; Cossi, M.; Millam, J. M.; Klene, M.; Adamo, C.; Cammi, R.; Ochterski, J. W.; Martin, R. L.; Morokuma, K.; Farkas, O.; Foresman, J. B.; Fox, D. J. *Gaussian16 Rev. B.01*; Gaussian, Incorp.: Wallingford, CT, 2016.

73. Maeda, S.; Harabuchi, Y.; Sumiya, Y.; Takagi, M.; Suzuki, K.; Sugiyama, K.; Ono, Y.; Hatanaka, M.; Osada, Y.; Taketsugu, T.; Morokuma, K.; Ohno, K.; *GRRM (A Developmental Version)*; Hokkaido University, 2020.

3. Kinetic Analysis of a Reaction Path Network Including Ambimodal Transition States: A Case Study of an Intramolecular Diels−Alder Reaction

3.1 Introduction

The intrinsic reaction coordinate (IRC) is widely used to analyze reaction mechanisms based on quantum chemical calculations (1,2). An IRC path is defined as the mass-weighted steepest descent path from a transition state (TS) connecting two minima (MINs) on the potential energy surface (PES) and represents an elementary reaction. The rate constant k for an elementary reaction represented by an IRC path can be calculated using the following equation based on the transition state theory (3,4)

$$k = \Gamma \frac{k_B T}{h} \exp\left(-\frac{\Delta G_{\mathrm{TS}} - \Delta G_R}{RT}\right), \tag{3.1}$$

where ΔG_{TS} and ΔG_{R} are the relative Gibbs free energies of the TS and reactant, respectively, k_{B} is the Boltzmann constant, T is the temperature, h is the Planck constant, R is the gas constant, and Γ is the transmission coefficient.

In recent years, the development of several automated reaction path search methods, such as the anharmonic downward distortion following (5–7) and artificial force induced reaction (AFIR) methods (8,9), has made it possible to construct a reaction path network where IRC paths connect a number of minima on the PES. By calculating the rate constants of all elementary reactions in a reaction path network using eq 1 and solving the resulting rate equations, the time propagation of the

populations of all MINs in the network can be investigated.

Because the reaction path network can consist of both fast (e.g., conformational change) and relatively slow elementary reactions (e.g., bond reorganization), it is difficult to solve the rate equations numerically. One of the solutions to this problem is the rate constant matrix contraction (RCMC) method (10,11). This method repeats the operation of contraction, which distributes short-life intermediates to neighboring MINs and generates superstates (denoted by SS). The overall rate constants, which include the effect of multiple conformers existing in the reaction path network, are obtained as rate constants for the transition between SSs. In addition, by simultaneously distributing the population during contraction, the time propagation of the population can be traced. Chemical reactions consisting of many elementary reactions can also be simulated for a long time. The details of the RCMC method were described in a previous review (11).

The IRC-based reaction analysis described above is widely used and often provides reasonable insight into a chemical reaction. However, this analysis sometimes fails to explain the experimental picture because it does not account for the effect of the kinetic energies of the nuclei (12). In particular, dynamical bifurcations (13,14) are the most important factor because they have a significant impact on the actual yields. When dynamical bifurcations occur, an ensemble of trajectories passing through a single TS, called ambimodal TS, bifurcates to multiple minima (15,16). Dynamical bifurcations were initially found in theoretical studies (17–32) and have since been reported for various organic, organometallic, and biochemical reactions (33–71).

Dynamical bifurcations cannot be studied by analyses based on an IRC path, which

connects one reactant and one product minimum. On the other hand, using analyses based on static PES information, they can be found by searching for a point where the shape of the PES perpendicular to the IRC changes from the valley to the ridge called the valley-ridge transition point. However, such analyses do not provide information about the products of the dynamical bifurcation and branching ratio (17,72). Thus, ab initio molecular dynamics (AIMD) simulations have been employed to investigate dynamical bifurcations. AIMD provides information about not only the occurrence of dynamical bifurcation, but also the branching ratio, and has been applied to various reactions (12,73). However, it is time-consuming to simulate reactions longer than a nanosecond because the computational cost of AIMD is proportional to the time scale. A chemical reaction accompanied by dynamical bifurcations consists of a short process of molecular motion causing the dynamical bifurcations and a long process of interconversion between products (55). Thus, a comprehensive analysis of these processes is necessary to understand selectivity. The present study aims to realize a long simulation (longer than days) of a chemical reaction that includes dynamical bifurcations by combining kinetic analysis of a reaction path network consisting of wide time-range reaction processes and AIMD simulations dealing with molecular motions after passage through a TS.

3.2 Theory

In the present study, the kinetic analysis of a reaction path network including ambimodal TSs is realized by combining three methods: the method for constructing a reaction path network including ambimodal TSs and their products developed in my previous study (74), AIMD simulation to evaluate the branching ratios, and a newly introduced method for modifying the rate constant to

incorporate the branching ratios. Each method is explained below.

3.2.1. Construction of a Reaction Path Network Including Ambimodal TSs

The method used to search for ambimodal TSs, reported in my previous work, is based on the AFIR method (74). Reaction paths from a MIN are located by applying an artificial force between so-called fragments, which are groups of atoms. The path followed is called an AFIR path (8). In the usual procedure, all AFIR paths are relaxed by the locally updated planes (LUP) method (the relaxed paths are called LUP paths). TS optimization is then performed from the energy maxima along the LUP path, and the IRC is calculated from the optimized TS. When the AFIR method is applied to the reactant of an elementary reaction wherein the dynamical bifurcation gives two products, both AFIR paths from the reactants to the two products are obtained and give a common TS. TSs given by multiple AFIR paths are found among many TSs obtained from the search and regarded as ambimodal TSs. In this procedure, the products are obtained as the terminal points of the AFIR paths. The details of the method have been described in a previous paper (74).

In my previous study, ambimodal TSs were explored using the multi-component AFIR method, which was originally developed to search for intermolecular reactions (74). In this study, this method was extended to the single component AFIR (SC-AFIR) method to create a reaction path network. In the SC-AFIR method, fragment pairs are systematically defined for MINs obtained by the search, and the procedure of the AFIR method described above is repeated. In this way, a reaction path network based on the IRC paths is obtained. In principle, it is necessary to perform TS

optimization from the energy maxima of all obtained LUP paths to identify the ambimodal TSs included in the reaction path network using the procedure described above. However, because of the large number of LUP paths included in the reaction path network, it is not easy to calculate the TSs for all paths.

Recently, to reduce the computational cost of TS optimization, kinetic analysis based on an IRC-LUP hybrid network was proposed. In this approach, the IRC paths are used only for the kinetically important paths, and the LUP paths are used for the other paths (75,76). When constructing an IRC-LUP hybrid network, the RCMC method is used to extract the kinetically important paths (called Bottleneck paths) for the reaction path network based on the LUP path, and the IRC paths for the Bottleneck paths are calculated by optimizing the energy maxima of the corresponding LUP paths to the true TS. This treatment excludes very high-energy TSs and insignificant reaction paths, such as conformational changes. I followed this procedure and searched for ambimodal TSs only for Bottleneck paths. In this treatment, ambimodal TSs in paths other than the Bottleneck paths are ignored because they are assumed to have no significant impact on the kinetics or reaction yields. This allowed me to efficiently search for only the kinetically important ambimodal TSs. The actual definition of the Bottleneck paths in this study is presented in the Computational Details section.

3.2.2. Prediction of the Branching Ratio Using AIMD

In this study, AIMD simulations were performed in the vicinity of the TS to estimate the branching ratio from the number of trajectories leading to each product. The initial condition for

AIMD was defined using the Progdyn program (41). Here, the $3N$-7 (N is the number of atoms) modes orthogonal to the imaginary vibrational modes were treated as quantized harmonic oscillators. For the $3N$-7 modes, the initial positions and momenta of trajectories were determined based on randomly generated angles in phase space and the quantized vibrational energies sampled to follow a Boltzmann distribution. For the imaginary vibrational modes, only the momentum was sampled so that the kinetic energy follows a Boltzmann distribution. The previous studies verified that AIMD simulation using this initial sampling accurately predicted the experimental ratio (45).

3.2.3. Rate Constants of Dynamical Bifurcations

In the kinetic simulations, a dynamical bifurcation is represented by elementary reactions, to which rate constants are assigned. **Figure 3.1** shows the transformation of a dynamical bifurcation giving n products to $2n$ rate constants, where R is the reactant, Pi is the i-th product (i = 0–n), p_i is the branching ratio for Pi, and $k_{R\rightarrow Pi}$ and $k_{Pi\rightarrow R}$ are the rate constants for R→Pi and Pi→R, respectively. In this study, the rate constants are assumed to satisfy the following three conditions: 1) the sum of the rate constants of processes leading from the reactant to a product via a common TS, $k_{R\rightarrow P1}$, $k_{R\rightarrow P2}$, …, $k_{R\rightarrow Pn}$, is equal to the rate constant evaluated by the conventional transition state theory, 2) the ratio of the rate constant of each product formation is equal to the branching ratio, and 3) the detailed balance is satisfied in thermal equilibrium. On the basis of these assumptions, the rate constants are expressed by the following equations:

$$k_{R\to Pi} = p_i \Gamma \frac{k_B T}{h} \exp\left(-\frac{\Delta G_{\mathrm{TS}} - \Delta G_R}{RT}\right), \tag{3.2}$$

$$k_{Pi\to R} = p_i \Gamma \frac{k_B T}{h} \exp\left(-\frac{\Delta G_{\mathrm{TS}} - \Delta G_{Pi}}{RT}\right). \tag{3.3}$$

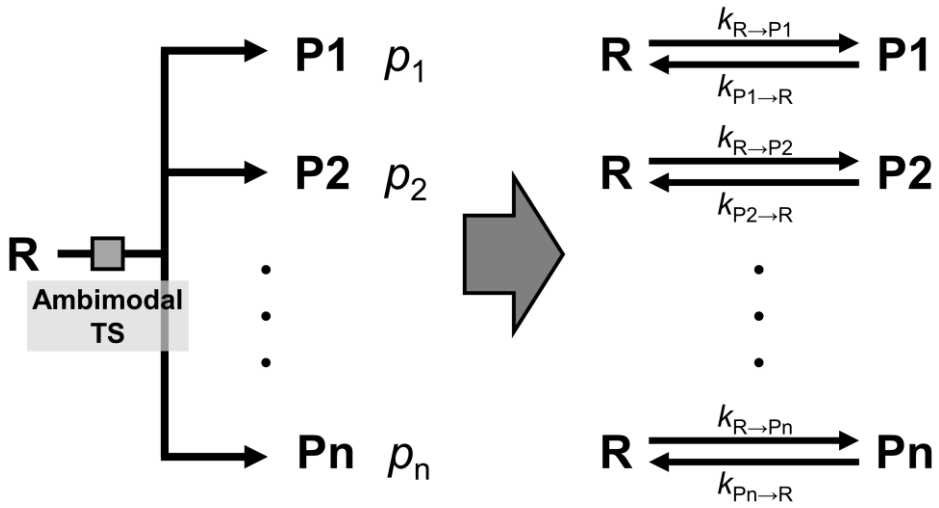

Figure 3.1. Schematic picture of the transformation of a dynamical bifurcation giving *n* products to 2*n* rate constants. R is the reactant, P*i* is the *i*-th product (*i* = 0–*n*), p_i is the branching ratio for P*i*, and $k_{R\to Pi}$ and $k_{Pi\to R}$ are the rate constants for R⟶Pi and P*i*⟶R, respectively.

3.3 Computational Details

The proposed kinetic analysis methodology was applied to an intramolecular Diels-Alder reaction that reportedly involves dynamical bifurcations, as shown in **Scheme 3.1** (36). The reactant has both a cyclobutadiene and butadiene skeleton. When butadiene or cyclobutadiene acts as the diene, the (4+2) or (2+2) product, respectively, is obtained. Experimentally, the two products are obtained in a (4+2):(2+2) ratio of 3.5:1.0 (37).

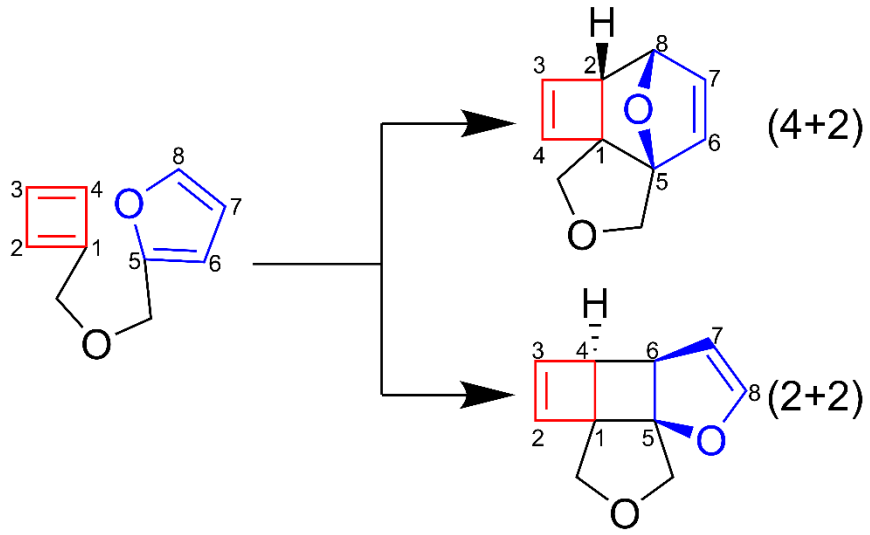

Scheme 3.1. Reaction scheme of an intramolecular Diels-Alder reaction accompanied by dynamical bifurcations.

SC-AFIR was applied to construct a reaction path network for the target reaction. To explore only the kinetically accessible region, a method called kinetics-based navigation (75) was used in this study. In the kinetics-based navigation, MINs for the SC-AFIR search were chosen on the basis of a value called traffic volume, Λ_i, the sum of the population inflow to the i-th MIN and population outflow from the i-th MIN. During the SC-AFIR search with kinetics-based navigation, on-the-fly kinetic simulations were performed to calculate the Λ_i for each MIN, and the SC-AFIR search was applied to MINs with $\Lambda_i \geq 10^{-10}$. The details were presented in previous papers (11,75). Three temperatures (250, 300, and 350 K) and a timescale of 1.0 s were specified for the kinetics-based navigation, and all the obtained AFIR paths were relaxed using the LUP method. The SC-AFIR search requires a large amount of computational cost, and thus the smaller basis set, D95V, is used in

the search, and all the paths are refined using a larger basis set, 6-31+G(d). The previous work suggests the ωB97X-D (77) functional provides reasonable geometries in the case of Diels-Alder reactions (78). Thus, the SC-AFIR search was performed at the ωB97X-D/D95V level with the Grid=FineGrid option. The obtained LUP paths were then relaxed again at the ωB97X-D/6-31+G(d) level.

Subsequently, as described in the Method section, Bottleneck paths were selected using the RCMC method and relaxed until their energy maxima converged to the corresponding TS. In the present study, the Bottleneck paths correspond to those connecting MINs belonging to the reactant's SS and a product's SS and those connecting MINs belonging to the different product's SS, respectively. The SSs of the products were defined on the basis of $\Lambda_i \geq 10^{-10}$ when the RCMC method was applied using a timescale of 1.0 s at 250, 300, and 350 K.

The ambimodal TSs in the obtained reaction path network were explored using the method described above. From TSs where dynamic bifurcations occur, AIMD simulations were performed at the ωB97X-D/6-31+G(d) level. In the AIMD calculations, the temperature was set to 298.15 K for the initial condition, and the time step was set to 0.5 fs. The settings for each AIMD simulation are described in the Results and Discussion section. Although three temperatures (250, 300, and 350 K) were used during the construction of the reaction path network to see various chemical transformations that possibly proceed at these temperatures, all the kinetic simulations using the resultant reaction path network were performed at 298.15 K. The rate constants were evaluated using eq 1, eq 2, or eq 3, where the Wigner correction (3) is used as Γ. Although the variational effects and

multi-dimensional tunneling effects on the rate constants were discussed in the previous studies (3,79), the conventional one with the Wigner correction was adopted in this study by compromise of huge costs to evaluate accurate rate constants taking these effects into account for the thousands of elementary reactions in the reaction path network.

All electronic structure calculations were performed using Gaussian16 (80). AFIR, LUP, IRC, and RCMC calculations were performed using the developer version of GRRM (81), and AIMD calculations were performed using the Progdyn program (41).

3.4 Results

3.4.1 Reaction Path Network

The reaction path network obtained by the SC-AFIR method contains 468 MINs, 7 IRC paths, and 1162 LUP paths. **Figure 3.2** shows the reaction path network, in which MINs are indicated by nodes and reaction paths by edges. The red and gray lines indicate Bottleneck paths (see the definition in the Computational Details section) and the other paths, respectively.

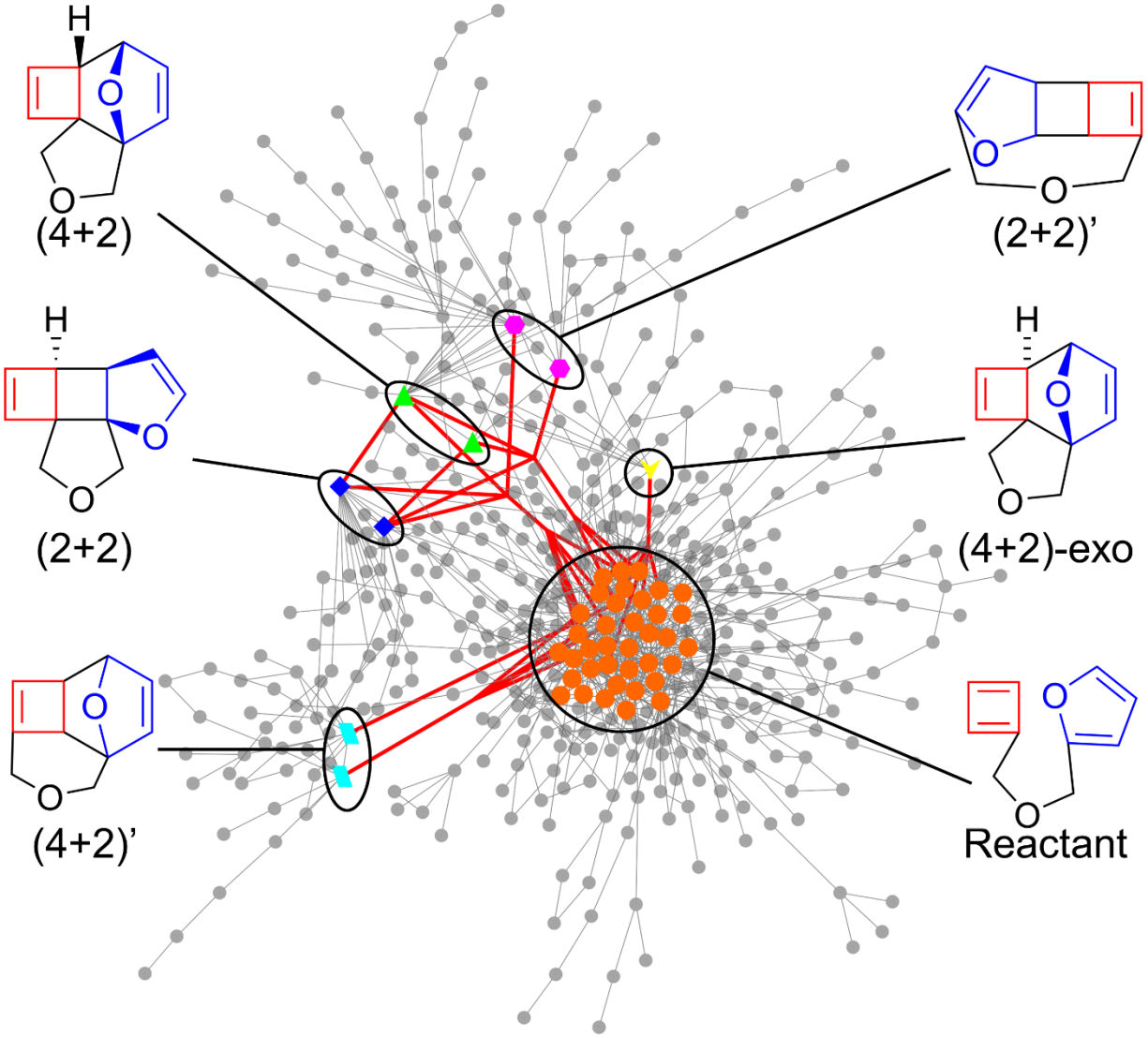

Figure 3.2. Reaction path network obtained by the single-component artificial force induced reaction search. Circles, triangles, hexagons, diamonds, parallelograms, and a wedge represent minima (MINs), and lines represent reaction paths. The red and gray lines indicate Bottleneck paths and the other paths, respectively. The branches of the red lines indicate dynamical bifurcations. Structural formulas are depicted for MINs connected by Bottleneck paths.

Additionally, the structural formulas of the MINs connected by the Bottleneck paths are depicted. The reaction path network includes the reactants, the experimentally observed (2+2) and (4+2) products, and other cycloadducts.

There are four ambimodal TSs in the reaction network from which six dynamical bifurcations occur (represented by the branches of red lines in **Figure 3.2**). In other words, dynamical bifurcations occur along both sides of the IRC path in two cases. Four of the six dynamical bifurcations lead to different reactant conformations. Because these conformers are connected by a low-barrier reaction path, the corresponding dynamical bifurcations do not affect the kinetic analyses and are not discussed further. The other two dynamical bifurcations lead to different chemical species and are discussed in detail below.

3.4.2 Obtained dynamical bifurcations

Figure 3.3 shows the geometries of two ambimodal TSs, TS1 and TS2. Both dynamical bifurcations give three products, namely the (4+2), (2+2), and (2+2)' products. Notably, only one of these TSs, TS1, has been discussed in a previous study (36); thus, this is the first report of the existence of the two low-lying TSs in this reaction. In addition, new bifurcating paths that have not been experimentally observed were found for the (2+2) product. However, the results suggest that the (2+2)' product is difficult to obtain because $r_{C3–C7}$ (pertaining to the bond formed when the (2+2)' product is generated) is longer than $r_{C2–C8}$ (pertaining to the bond formed when the (4+2) product is generated), $r_{C4–C6}$ (pertaining to the bond formed when the (2+2) product is generated), or $r_{C1–C5}$ (pertaining to the bond formed when the (2+2) or (4+2) product is generated) in both TSs, where $r_{Ck–Cl}$ is the distance between C*k* and C*l*. AIMD simulations are necessary to confirm this hypothesis.

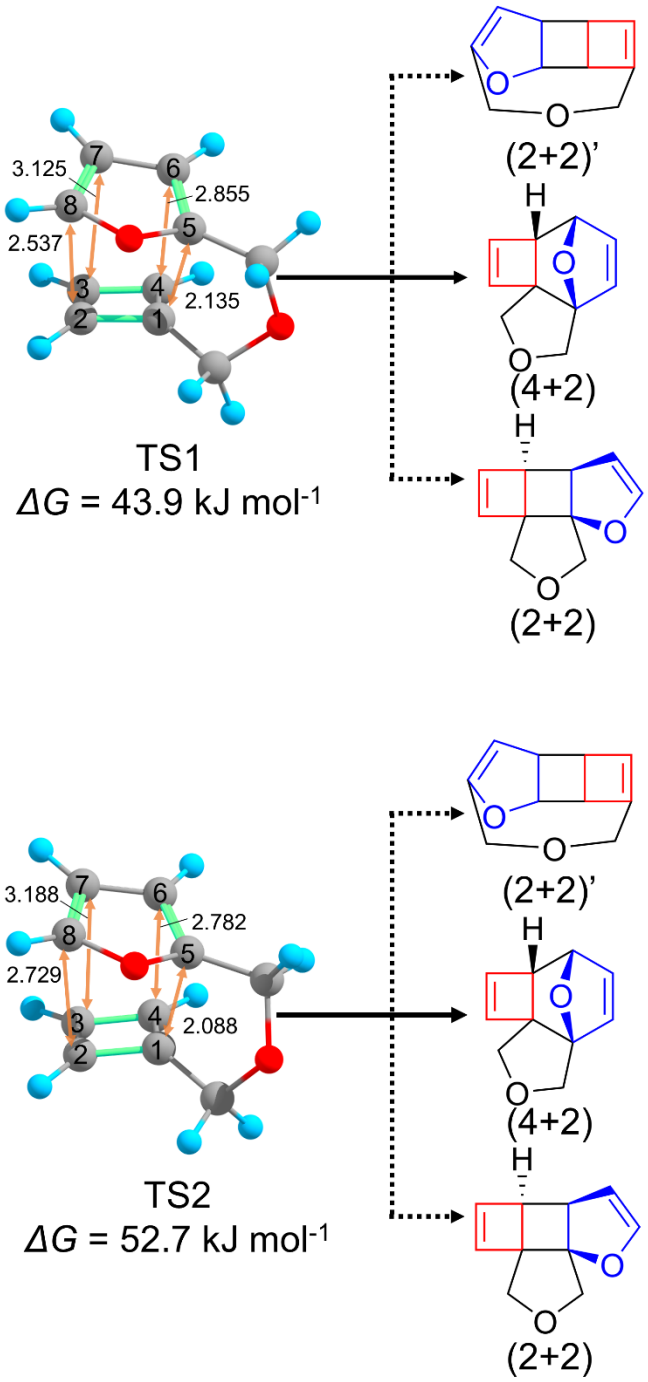

Figure 3.3. Geometries of two ambimodal transition states (TSs) and structural formulas of their products. The solid lines connect to the intrinsic reaction coordinate products, and the dotted lines connect to the other products. The interatomic distances on the TSs associated with the bonds formed in some of the products are shown in Å.

3.4.3 ab initio molecular dynamics

Table 3.1 shows the results of the AIMD simulations starting from TS1 and TS2. The destination of the trajectories were classified into four groups according to interatomic distances. The calculations were terminated when the trajectories reached one of the four destinations: $r_{C1–C5} < r_{form}$ and $r_{C2–C8} < r_{form}$ for the (4+2) product, $r_{C1–C5} < r_{form}$ and $r_{C4–C6} < r_{form}$ for the (2+2) product, $r_{C2–C8} < r_{form}$ and $r_{C3–C7} < r_{form}$ for the (2+2)' product, and $r_{C1–C5} > r_{diss}$, $r_{C2–C8} > r_{diss}$, $r_{C3–C7} > r_{diss}$, and $r_{C4–C6} > r_{diss}$ for the reactant, where r_{form} is 1.875 Å and r_{diss} is 2.400 Å. **Table 3.1** shows the number of trajectories and branching ratios for each destination.

The (4+2) product is a major product for both TSs, although the number of trajectories leading to the (2+2) product from TS2 is larger than that from TS1. There are no trajectories from TS1 or TS2 to the (2+2)' product. This indicates that although the shape of the PES suggests the accessibility of this product, but the reaction does not occur easily from a dynamical aspect. Since these two ambimodal TSs are energetically competitive, consideration of both TSs is necessary.

Table 3.1. Number of trajectories leading to the products and branching ratio obtained by ab initio molecular dynamics simulations of 500 trajectories starting from the transition states (TSs), TS1 and TS2.[a]

	TS1	TS2
total	500	500
(4+2)	452 (91.3%)	372 (74.5%)
(2+2)	43 (8.7%)	127 (25.5%)
(2+2)'	0 (0.0%)	0 (0.0%)
reactant	5	1

[a]The trajectories are categorized according to their destination, i.e., (4+2) product, (2+2) product, (2+2)' product, and reactant.

Figures 3.4a and **3.4b** show the variation of $r_{C4–C6}$ and $r_{C2–C8}$ along each of the 500 trajectories starting from TS1 and TS2, respectively. The blue, red, and green lines show the trajectories leading to the (2+2) product, (4+2) product, and reactant, respectively. In the figure, TS1, TS2, and the two TSs connecting the (2+2) and (4+2) products, TS3 and TS4, are indicated by black circles, and the IRCs from these TSs are depicted as black lines. TS1 and TS2 are located on the (4+2) side compared to TS3 and TS4, which explains the larger branching ratios of the (4+2) product in both cases. As indicated in **Table 3.1**, the ratio of the (2+2) product from TS1 (8.7%) is smaller than that from TS2 (25.5%) since TS2 ($r_{C4–C6}$ = 2.782 Å and $r_{C2–C8}$ = 2.729 Å) is located closer to the (2+2) product than TS1 ($r_{C4–C6}$ = 2.855 Å and $r_{C2–C8}$ = 2.537 Å) (**Figures 3.3** and **3.4a**). This correlation between bond length and branching ratio is consistent with a previous claim (82).

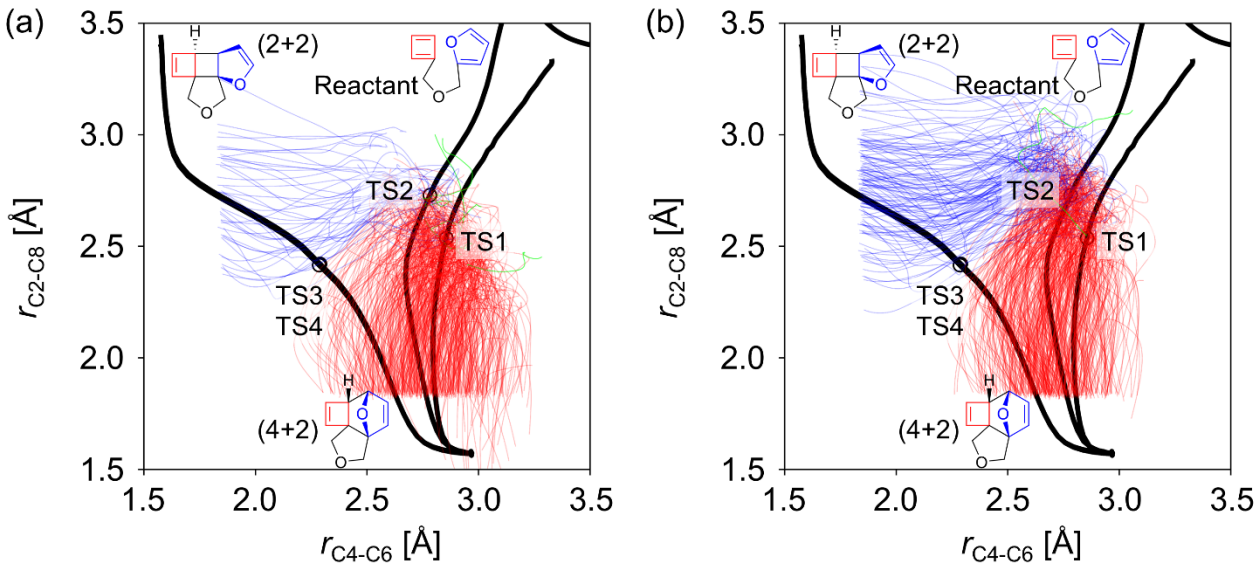

Figure 3.4. Plot of two interatomic distances along the ab initio molecular dynamics (AIMD) trajectories and intrinsic reaction coordinate (IRC) paths. The *x* and *y* axes correspond to the $r_{C4–C6}$ and $r_{C2–C8}$ distances, respectively. Results of AIMD simulations from the transition states (TSs), (a) TS1 and (b) TS2. The red, blue, and green lines show the trajectories leading to the (2+2) product, (4+2) product, and reactant, respectively. TS1, TS2, and the TSs connecting the (2+2) and (4+2) products, TS3 and TS4, are indicated by black circles and the IRC paths from them by black lines. Most trajectories leading to the (4+2) product were terminated when $r_{C2–C8} < r_{form}$, which corresponds to the case where the C2–C8 bond forms after the C1–C5 bond. On the other hand, some trajectories explored the region where $r_{C2–C8} < r_{form}$, which corresponds to the case where the C2–C8 bond forms before the C1–C5 bond.

3.4.4 Kinetic simulations

Figure 3.5 shows the time propagation of the populations of all chemical species computed

by applying the RCMC method in the time range from 10^{-14} to 10^{16} s. **Figures 3.5a** and **3.5b** correspond to the reaction path network without and with dynamical bifurcations, respectively. For the latter case, the rate constants incorporate the AIMD branching ratios, as described in the Method section. In the kinetic simulations, the temperature was set to 298.15 K, and the initial population was set to 1.0 for one of the reactant MINs.

As shown in **Figure 3.5a**, the population of the reactant is almost 1.0 from 10^{-14} to 10^{-4} s. Subsequently, the reaction proceeds in 10^{-3} s, and the (4+2) product is obtained with a population of 1.0. The population of the (2+2) product is zero in 10^{0} s, which is near the experimental timescale, because there are no paths connecting the reactant to this product in the reaction path network based on the IRC paths. On the other hand, in the reaction path network with dynamical bifurcations, the populations of the (4+2) and (2+2) products at 10^{0} s are 0.910 and 0.090, respectively (**Figure 3.5b**). This is qualitatively consistent with the experimental observation that the (2+2) product is a byproduct. Such a comprehensive discussion, including the short-lifetime process of molecular motion beyond the TS bifurcating to products and long-lifetime process accompanying bond reorganizations, is realized for the first time using the present methodology.

Notably, this study aims to discuss how ambimodal TSs affect the kinetic behaviors on the reaction path network. Therefore, a quantitative reproduction of the experimental values is beyond the scope of this study. Although it is better to calculate more accurate rate constants taking higher-order electron correlations, variational effects in TST, multi-dimensional tunneling effects, anharmonicity in the initial sampling of AIMD, and so on into account, such calculations are

computationally impractical in the case using the reaction path network including thousands of elementary reactions, and, thus, are not performed in this study.

The ratio of the (2+2) product (0.090) in **Figure 3.5b** is slightly larger than the AIMD branching ratio of the (2+2) product from TS1 (0.087) in **Table 3.1**. This difference is due to the existence of TS2, which has a slightly higher energy than TS1. This result verifies the importance of considering multiple TSs in a reaction path network to understand the experimental reaction yields. Note that the effect of multiple TSs is not discussed in the conventional AIMD simulation from a single TS.

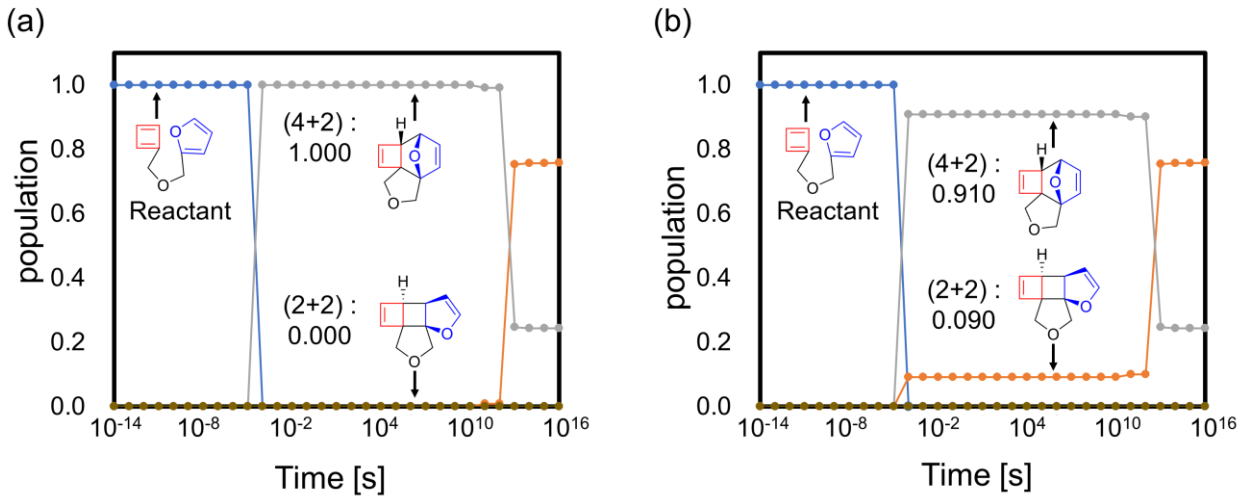

Figure 3.5. Time propagation of the populations of all chemical species from 10^{-14} to 10^{16} s in the reaction path network (a) without and (b) with dynamical bifurcations.

As shown in **Figure 3.5**, in timescales longer than 10^{12} s, the ratio of the two products is

(4+2):(2+2) = 0.24:0.76. In other words, the populations are the same in the models with and without dynamical bifurcations. This corresponds to the ratio of the Boltzmann distribution at 298.15 K, which is caused by the thermal equilibrium between the (4+2) and (2+2) products at 10^{13} s. This result clearly indicates that dynamical bifurcations affect the populations only until 10^{12} s. In other words, the existence of a high-energy barrier that cannot be overcome in the experimental timescale is necessary to observe the effect of the dynamical bifurcations from TS1 and TS2 in this reaction. Notably, the timescale considered in the simulation exceeds the experimental reaction time, and the present search focusing on kinetically feasible paths under the given reaction conditions might have missed paths that occur in the longer timescale than the experimental reaction time.

Table 3.2 shows the rate constants of the elementary reactions leading from the reactant to the (2+2) or (4+2) product. The rate constants are calculated using four models: the lowest conformer to multiple transition states (LC-mTS)-IRC model, LC-mTS-Bif model, RCMC-IRC model, and RCMC-Bif model (i.e., the present method). In the LC-mTS-IRC model, the rate constants of the processes leading to the IRC product (i.e., (4+2) product) via TS1 and IRC product via TS2 are first calculated using eq 1 and then summed. In the LC-mTS-Bif model, four rate constants, namely the rate constants of the processes leading to the (2+2) product via TS1, (4+2) product via TS1, (2+2) product via TS2, and (4+2) product via TS2 are first calculated using eq 2 and then the sum for each product is obtained. In both models, the relative Gibbs free energy of the most stable reactant conformer was used as ΔG_R in eq 1 or eq 2. In the RCMC-IRC and RCMC-Bif models, the rate constants are calculated by applying the RCMC method to the reaction path network without and with

dynamical bifurcations, respectively. As indicated in **Table 3.2**, the rate constant of the process leading to the (4+2) product in the RCMC-IRC model is about four times smaller than that in the LC-mTS-IRC model. This is because the existence of multiple reactant conformers in the reaction path network stabilizes the reactant state. On the other hand, the rate constant of the process leading to the (2+2) product is almost zero in both the LC-mTS and RCMC-IRC models since there is no IRC path connecting the reactant and (2+2) product. The LC-mTS-Bif model gives a non-zero value for the rate constant of the process leading to the (2+2) product, although the effect of multiple reactant conformers is excluded. The RCMC-Bif model also gives a non-zero rate constant for the process leading to the (2+2) product. Moreover, both rate constants are about four times smaller than those obtained using LC-mTS-Bif model. This indicates that the present method provides rate constants that include the effects of both dynamical bifurcations and multiple conformers in the reaction path network.

Table 3.2. Rate constants of the elementary reactions leading from the reactant to the (2+2) and (4+2) products calculated using the lowest conformer to multiple transition states-intrinsic reaction coordinate (LC-mTS-IRC), LC-mTS-bifurcation (Bif), rate constant matrix contraction (RCMC)-IRC, and RCMC-Bif models.[a]

	LC-mTS-IRC [s^{-1}]	LC-mTS-Bif [s^{-1}]	RCMC-IRC [s^{-1}]	RCMC-Bif [s^{-1}]
(4+2)	1.51×10^5	1.37×10^5	3.78×10^4	3.44×10^4
(2+2)	0	1.38×10^4	9.11×10^{-23}[b]	3.46×10^3

[a]The details of each model are explained in the text. [b]This very small rate constant represents the process of passing through the (4+2) product once before reaching the (2+2) product.

3.5 Conclusion

In this study, a methodology for performing kinetic simulation on the reaction path network including ambimodal TSs was realized by combining kinetic analysis of a reaction path network, which deals with slow processes, and AIMD simulations, which deal with fast molecular motions after passing a TS. In the present method, the automated search method for ambimodal TSs generated a reaction path network that includes ambimodal TSs. This search was limited to Bottleneck paths to improve the efficiency and reduce the computational cost. Subsequently, the branching ratios were estimated by performing AIMD simulations and then used to evaluate the rate constants. The method for including dynamical bifurcations in the rate constants was derived for the first time in this study. Finally, a kinetic simulation to trace the time propagation of the population of each chemical species was performed using the modified rate constants.

The present methodology was applied to an intramolecular Diels-Alder reaction, for which

the occurrence of dynamical bifurcations has been previously reported. Two ambimodal TSs were found in the reaction path network, and the branching ratios were calculated using AIMD simulations. The (4+2) product was found to be the major product in both dynamical bifurcations. Finally, kinetic simulations were performed for the reaction path network without and with dynamical bifurcations. In the case of a reaction path network without dynamical bifurcations, only the (4+2) product was obtained. On the other hand, the (2+2) product was also obtained in the analyses based on the reaction path network with dynamical bifurcations, which is qualitatively consistent with the generation of the (2+2) product in the experiment. In addition, it took 10^{13} s to reach thermal equilibrium between the two products, and the ratio determined by dynamical bifurcations was maintained until 10^{12} s. The present results revealed that the experimental ratio is determined not by the interconversion between the products, but by the dynamical bifurcations.

Not only the most stable TS, but also the metastable TS, contributed to the selectivity obtained by the present methodology. Moreover, the overall branching ratio when dynamical bifurcations occur from two energetically competing TSs can be estimated, which is difficult to achieve using only AIMD-based analyses. Finally, the present methodology enables the calculation of rate constants that include two effects: multiple conformers in the reaction path network and branching ratio. Thus, this methodology is expected to be used in the analysis of various chemical reactions involving dynamical bifurcations in the future.

3.6 Reference

1. Fukui, K. Formulation of the Reaction Coordinate. *J. Phys. Chem.* **1970**, *74* (23), 4161–4163. https://doi.org/10.1021/j100717a029.

2. Fukui, K. The Path of Chemical Reactions - The IRC Approach. *Acc. Chem. Res.* **1981**, *14* (12), 363–368. https://doi.org/10.1021/ar00072a001.

3. Fernández-Ramos, A.; Miller, J. A.; Klippenstein, S. J.; Truhlar, D. G. Modeling the Kinetics of Bimolecular Reactions. *Chem. Rev.* **2006**, *106* (11), 4518–4584. https://doi.org/10.1021/cr050205w.

4. Klippenstein, S. J.; Pande, V. S.; Truhlar, D. G. Chemical Kinetics and Mechanisms of Complex Systems: A Perspective on Recent Theoretical Advances. *J. Am. Chem. Soc.* **2014**, *136* (2), 528–546. https://doi.org/10.1021/ja408723a.

5. Maeda, S.; Ohno, K. A New Method for Constructing Multidimensional Potential Energy Surfaces by a Polar Coordinate Interpolation Technique. *Chem. Phys. Lett.* **2003**, *381* (1–2), 177–186. https://doi.org/10.1016/j.cplett.2003.08.129.

6. Ohno, K.; Maeda, S. A Scaled Hypersphere Search Method for the Topography of Reaction Pathways on the Potential Energy Surface. *Chem. Phys. Lett.* **2004**, *384* (4–6), 277–282. https://doi.org/10.1016/j.cplett.2003.12.030.

3. Kinetic Analysis including dynamical bifurcations

7. Maeda, S.; Ohno, K. Global Mapping of Equilibrium and Transition Structures on Potential Energy Surfaces by the Scaled Hypersphere Search Method: Applications to Ab Initio Surfaces of Formaldehyde and Propyne Molecules. *J. Phys. Chem. A* **2005**, *109* (25), 5742–5753. https://doi.org/10.1021/jp0513162.

8. Maeda, S.; Morokuma, K. Communications: A Systematic Method for Locating Transition Structures of A+B→X Type Reactions. *J. Chem. Phys.* **2010**, *132* (24), 241102. https://doi.org/10.1063/1.3457903.

9. Maeda, S.; Morokuma, K. Finding Reaction Pathways of Type A + B → X: Toward Systematic Prediction of Reaction Mechanisms. *J. Chem. Theor. Comput.* **2011**, *7* (8), 2335–2345. https://doi.org/10.1021/ct200290m.

10. Sumiya, Y.; Nagahata, Y.; Komatsuzaki, T.; Taketsugu, T.; Maeda, S. Kinetic Analysis for the Multistep Profiles of Organic Reactions: Significance of the Conformational Entropy on the Rate Constants of the Claisen Rearrangement. *J. Phys. Chem. A* **2015**, *119* (48), 11641–11649. https://doi.org/10.1021/acs.jpca.5b09447.

11. Sumiya, Y.; Maeda, S. Rate Constant Matrix Contraction Method for Systematic Analysis of Reaction Path Networks. *Chem. Lett.* **2020**, *49* (5), 553–564. https://doi.org/10.1246/cl.200092.

12. Rehbein, J.; Carpenter, B. K. Do We Fully Understand What Controls Chemical Selectivity? *Phys. Chem. Chem. Phys.* **2011**, *13* (47), 20906–20922. https://doi.org/10.1039/c1cp22565k.

13. Ess, D. H.; Wheeler, S. E.; Iafe, R. G.; Xu, L.; Çelebi-Ölçüm, N.; Houk, K. N. Bifurcations on Potential Energy Surfaces of Organic Reactions. *Angew. Chem. Int. Ed. Engl.* **2008**, *47* (40), 7592–7601. https://doi.org/10.1002/anie.200800918.

14. Hare, S. R.; Tantillo, D. J. Post-Transition State Bifurcations Gain Momentum – Current State of the Field, *J. Pure Appl. Chem.* **2017**, *89* (6), 679-698. https://doi.org/10.1515/pac-2017-0104.

15. Pham, H. V.; Houk, K. N. Diels–Alder Reactions of Allene with Benzene and Butadiene: Concerted, Stepwise, and Ambimodal Transition States. *J. Org. Chem.* **2014**, *79* (19), 8968–8976. https://doi.org/10.1021/jo502041f.

16. Houk, K. N.; Xue, X.-S.; Liu, F.; Chen, Y.; Chen, X.; Jamieson, C. Computations on Pericyclic Reactions Reveal the Richness of Ambimodal Transition States and Pericyclases. *Isr. J. Chem.* **2021**, *61*. https://doi.org/10.1002/ijch.202100071.

17. Valtazanos, P.; Ruedenberg, K. Bifurcations and Transition States. *Theoret Chim. Acta* **1986**, *69* (4), 281–307. https://doi.org/10.1007/BF00527705.

18. Basilevsky, M. V. The Structural Stability Principle and Branching Points on Multidimensional Potential Energy Surfaces. *Theoret Chim. Acta* **1987**, *72* (1), 63–67. https://doi.org/10.1007/BF00526555.

19. Quapp, W. Gradient Extremals and Valley Floor Bifurcations on Potential Energy Surfaces. *Theoret Chim. Acta* **1989**, *75* (6), 447–460. https://doi.org/10.1007/BF00527676.

20. Baker, J.; Gill, P. M. W. An Algorithm for the Location of Branching Points on Reaction Paths. *J. Comput. Chem.* **1988**, *9* (5), 465–475. https://doi.org/10.1002/jcc.540090505.

21. Valtazanos, P.; Elbert, S. T.; Xantheas, S.; Ruedenberg, K. The Ring Opening of Cyclopropylidene to Allene: Global Features of the Reaction Surface. *Theoret Chim. Acta* **1991**, *78* (5–6), 287–326. https://doi.org/10.1007/BF01112344.

22. Taketsugu, T.; Hirano, T. Mechanism of Bifurcation along the Reaction Path: An Application in the Case of Thioformaldehyde. *J. Chem. Phys.* **1993**, *99* (12), 9806–9814. https://doi.org/10.1063/1.465462.

23. Sastry, G. N.; Shaik, S. Structured Electron Transfer Transition State. Valence Bond Configuration Mixing Analysis and Ab Initio Calculations of the Reactions of Formaldehyde Radical Anion with Methyl Chloride. *J. Phys. Chem.* **1996**, *100* (30), 12241–12252. https://doi.org/10.1021/jp952827z.

24. Taketsugu, T.; Tajima, N.; Hirao, K. Approaches to Bifurcating Reaction Path. *J. Chem. Phys.* **1996**, *105* (5), 1933–1939. https://doi.org/10.1063/1.472063.

25. Yanai, T.; Taketsugu, T.; Hirao, K. Theoretical Study of Bifurcating Reaction Paths. *J. Chem. Phys.* **1997**, *107* (4), 1137–1146. https://doi.org/10.1063/1.474459.

26. Shaik, S.; Danovich, D.; Sastry, G. N.; Ayala, P. Y.; Schlegel, H. B. Dissociative Electron Transfer, Substitution, and Borderline Mechanisms in Reactions of Ketyl Radical Anions.

Differences and Difficulties in Their Reaction Paths. *J. Am. Chem. Soc.* **1997**, *119* (39), 9237–9245. https://doi.org/10.1021/ja971105d.

27. Taketsugu, T.; Yanai, T.; Hirao, K.; Gordon, M. S. Dynamic reaction path study of SiH_4+F^- $\rightarrow SiH_4F^-$ and the Berry pseudorotation with valley–ridge inflection. J. Mol. Struct. THEOCHEM **1998**, 15, *1* 163-177. https://doi.org/10.1016/S0166-1280(98)00169-9

28. Kumeda, Y.; Taketsugu, T. Isotope Effect on Bifurcating Reaction Path: Valley–Ridge Inflection Point in Totally Symmetric Coordinate. *J. Chem. Phys.* **2000**, *113* (2), 477–484. https://doi.org/10.1063/1.481826.

29. Taketsugu, T.; Kumeda, Y. An *Ab Initio* Direct-Trajectory Study of the Kinetic Isotope Effect on the Bifurcating Reaction. *J. Chem. Phys.* **2001**, *114* (16), 6973–6982. https://doi.org/10.1063/1.1358864.

30. Quapp, W. How Does a Reaction Path Branching Take Place? A Classification of Bifurcation Events. *J. Mol. Struct.* **2004**, *695–696*, 95–101. https://doi.org/10.1016/j.molstruc.2003.10.034.

31. Bofill, J. M.; Quapp, W. Analysis of the Valley-Ridge Inflection Points through the Partitioning Technique of the Hessian Eigenvalue Equation. *J. Math. Chem.* **2013**, *51* (3), 1099–1115. https://doi.org/10.1007/s10910-012-0134-3.

32. Harabuchi, Y.; Ono, Y.; Maeda, S.; Taketsugu, T.; Keipert, K.; Gordon, M. S. Nontotally Symmetric Trifurcation of an S_N2 Reaction Pathway. *J. Comput. Chem.* **2016**, *37* (5), 487–493. https://doi.org/10.1002/jcc.24241.

33. Yamataka, H.; Aida, M.; Dupuis, M. One Transition State Leading to Two Product States: Ab Initio Molecular Dynamics Simulations of the Reaction of Formaldehyde Radical Anion and Methyl Chloride. *Chem. Phys. Lett.* **1999**, *300* (5–6), 583–587. https://doi.org/10.1016/S0009-2614(98)01440-7.

34. Bakken, V.; Danovich, D.; Shaik, S.; Schlegel, H. B.; A Single Transition State Serves Two Mechanisms: An Ab Initio Classical Trajectory Study of the Electron Transfer and Substitution Mechanisms in Reactions of Ketyl Radical Anions with Alkyl Halides. *J. Am. Chem. Soc.* **2001**, *123* (1), 130–134. https://doi.org/10.1021/ja002799k.

35. Caramella, P.; Quadrelli, P.; Toma, L. An Unexpected Bispericyclic Transition Structure Leading to 4+2 and 2+4 Cycloadducts in the Endo Dimerization of Cyclopentadiene. *J. Am. Chem. Soc.* **2002**, *124* (7), 1130–1131. https://doi.org/10.1021/ja016622h.

36. Singleton, D. A.; Hang, C.; Szymanski, M. J.; Meyer, M. P.; Leach, A. G.; Kuwata, K. T.; Chen, J. S.; Greer, A.; Foote, C. S.; Houk, K. N. Mechanism of Ene Reactions of Singlet Oxygen. A Two-Step No-Intermediate Mechanism. *J. Am. Chem. Soc.* **2003**, *125* (5), 1319–1328. https://doi.org/10.1021/ja027225p.

37. Limanto, J.; Khuong, K. S.; Houk, K. N.; Snapper, M. L. Intramolecular Cycloadditions of Cyclobutadiene with Dienes: Experimental and Computational Studies of the Competing (2 + 2) and (4 + 2) Modes of Reaction. *J. Am. Chem. Soc.* **2003**, *125* (52), 16310–16321. https://doi.org/10.1021/ja0380547.

38. Li, J.; Li, X.; Shaik, S.; Schlegel, H. B. Single Transition State Serves Two Mechanisms. Ab Initio Classical Trajectory Calculations of the Substitution−Electron Transfer Branching Ratio in $CH_2O^{\bullet-} + CH_3Cl$. *J. Phys. Chem. A* **2004**, *108* (40), 8526–8532. https://doi.org/10.1021/jp046827n.

39. Bekele, T.; Christian, C. F.; Lipton, M. A.; Singleton, D. A. "Concerted" Transition State, Stepwise Mechanism. Dynamics Effects in C2-C6 Enyne Allene Cyclizations. *J. Am. Chem. Soc.* **2005**, *127* (25), 9216–9223. https://doi.org/10.1021/ja0508673.

40. Li, J.; Shaik, S.; Schlegel, H. B.; A Single Transition State Serves Two Mechanisms. The Branching Ratio for $CH_2O^{\bullet-} + CH_3Cl$ on Improved Potential Energy Surfaces. *J. Phys. Chem. A* **2006**, *110* (8), 2801–2806. https://doi.org/10.1021/jp0563336.

41. Ussing, B. R.; Hang, C.; Singleton, D. A. Dynamic Effects on the Periselectivity, Rate, Isotope Effects, and Mechanism of Cycloadditions of Ketenes with Cyclopentadiene. *J. Am. Chem. Soc.* **2006**, *128* (23), 7594–7607. https://doi.org/10.1021/ja0606024.

42. Celebi-Olçüm, N.; Ess, D. H.; Aviyente, V.; Houk, K. N. Lewis Acid Catalysis Alters the Shapes and Products of Bis-Pericyclic Diels-Alder Transition States. *J. Am. Chem. Soc.* **2007**, *129* (15), 4528–4529. https://doi.org/10.1021/ja070686w.

43. Thomas, J. B.; Waas, J. R.; Harmata, M.; Singleton, D. A. Control Elements in Dynamically Determined Selectivity on a Bifurcating Surface. *J. Am. Chem. Soc.* **2008**, *130* (44), 14544–14555. https://doi.org/10.1021/ja802577v.

44. Kelly, K. K.; Hirschi, J. S.; Singleton, D. A. Newtonian Kinetic Isotope Effects. Observation, Prediction, and Origin of Heavy-Atom Dynamic Isotope Effects. *J. Am. Chem. Soc.* **2009**, *131* (24), 8382–8383. https://doi.org/10.1021/ja9031083.

45. Wang, Z.; Hirschi, J. S.; Singleton, D. A. Recrossing and Dynamic Matching Effects on Selectivity in a Diels-Alder Reaction. *Angew. Chem. Int. Ed. Engl.* **2009**, *48* (48), 9156–9159. https://doi.org/10.1002/anie.200903293.

46. Hong, Y. J.; Tantillo, D. J. A Potential Energy Surface Bifurcation in Terpene Biosynthesis. *Nat. Chem.* **2009**, *1* (5), 384–389. https://doi.org/10.1038/nchem.287.

47. Hong, Y. J.; Tantillo, D. J. Quantum Chemical Dissection of the Classic Terpinyl/Pinyl/Bornyl/Camphyl Cation Conundrum-the Role of Pyrophosphate in Manipulating Pathways to Monoterpenes. *Org. Biomol. Chem.* **2010**, *8* (20), 4589–4600. https://doi.org/10.1039/c0ob00167h.

48. Siebert, M. R.; Zhang, J.; Addepalli, S. V.; Tantillo, D. J.; Hase, W. L. The Need for Enzymatic Steering in Abietic Acid Biosynthesis: Gas-Phase Chemical Dynamics Simulations of Carbocation Rearrangements on a Bifurcating Potential Energy Surface. *J. Am. Chem. Soc.* **2011**, *133* (21), 8335–8343. https://doi.org/10.1021/ja201730y.

49. Noey, E. L.; Wang, X.; Houk, K. N. Selective Gold(I)-Catalyzed Formation of Tetracyclic Indolines: A Single Transition Structure and Bifurcations Lead to Multiple Products. *J. Org. Chem.* **2011**, *76* (9), 3477–3483. https://doi.org/10.1021/jo200556f.

50. Tantillo, D. J. Biosynthesis via Carbocations: Theoretical Studies on Terpene Formation. *Nat. Prod. Rep.* **2011**, *28* (6), 1035–1053. https://doi.org/10.1039/c1np00006c.

51. Bogle, X. S.; Singleton, D. A. Dynamic Origin of the Stereoselectivity of a Nucleophilic Substitution Reaction. *Org. Lett.* **2012**, *14* (10), 2528–2531. https://doi.org/10.1021/ol300817a.

52. Gonzalez-James, O. M.; Kwan, E. E.; Singleton, D. A. Entropic Intermediates and Hidden Rate-Limiting Steps in Seemingly Concerted Cycloadditions. Observation, Prediction, and Origin of an Isotope Effect on Recrossing. *J. Am. Chem. Soc.* **2012**, *134* (4), 1914–1917. https://doi.org/10.1021/ja208779k.

53. Hong, Y. J.; Irmisch, S.; Wang, S. C.; Garms, S.; Gershenzon, J.; Zu, L.; Köllner, T. G.; Tantillo, D. J. Theoretical and Experimental Analysis of the Reaction Mechanism of MrTPS2, a

Triquinane-Forming Sesquiterpene Synthase from Chamomile. *Chemistry* **2013**, *19* (40), 13590–13600. https://doi.org/10.1002/chem.201301018.

54. Pemberton, R. P.; Hong, Y. J.; Tantillo, D. J. Inherent Dynamical Preferences in Carbocation Rearrangements Leading to Terpene Natural Products. *Pure Appl. Chem.* **2013**, *85* (10), 1949–1957. https://doi.org/10.1351/pac-con-12-11-22.

55. Zhang, L.; Wang, Y.; Yao, Z. J.; Wang, S.; Yu, Z. X. Kinetic or Dynamic Control on a Bifurcating Potential Energy Surface? An Experimental and DFT Study of Gold-Catalyzed Ring Expansion and Spirocyclization of 2-Propargyl-β-Tetrahydrocarbolines. *J. Am. Chem. Soc.* **2015**, *137* (41), 13290–13300. https://doi.org/10.1021/jacs.5b05971.

56. Patel, A.; Chen, Z.; Yang, Z.; Gutiérrez, O.; Liu, H. W.; Houk, K. N.; Singleton, D. A. Dynamically Complex [6+4] and [4+2] Cycloadditions in the Biosynthesis of Spinosyn A. *J. Am. Chem. Soc.* **2016**, *138* (11), 3631–3634. https://doi.org/10.1021/jacs.6b00017.

57. Hare, S. R.; Tantillo, D. J. Cryptic Post-Transition State Bifurcations That Reduce the Efficiency of Lactone-Forming Rh-Carbenoid C-H Insertions. *Chem. Sci.* **2017**, *8* (2), 1442–1449. https://doi.org/10.1039/c6sc03745c.

58. Hare, S. R.; Pemberton, R. P.; Tantillo, D. J. Navigating Past a Fork in the Road: Carbocation-π Interactions Can Manipulate Dynamic Behavior of Reactions Facing Post-Transition-

State Bifurcations. *J. Am. Chem. Soc.* **2017**, *139* (22), 7485–7493. https://doi.org/10.1021/jacs.7b01042.

59. Noey, E. L.; Yang, Z.; Li, Y.; Yu, H.; Richey, R. N.; Merritt, J. M.; Kjell, D. P.; Houk, K. N. Origins of Regioselectivity in the Fischer Indole Synthesis of a Selective Androgen Receptor Modulator. *J. Org. Chem.* **2017**, *82* (11), 5904–5909. https://doi.org/10.1021/acs.joc.7b00878.

60. Yu, P.; Chen, T. Q.; Yang, Z.; He, C. Q.; Patel, A.; Lam, Y. H.; Liu, C. Y.; Houk, K. N. Mechanisms and Origins of Periselectivity of the Ambimodal [6 + 4] Cycloadditions of Tropone to Dimethylfulvene. *J. Am. Chem. Soc.* **2017**, *139* (24), 8251–8258. https://doi.org/10.1021/jacs.7b02966.

61. Hare, S. R.; Li, A.; Tantillo, D. J. Post-Transition State Bifurcations Induce Dynamical Detours in Pummerer-Like Reactions. *Chem. Sci.* **2018**, *9* (48), 8937–8945. https://doi.org/10.1039/C8SC02653J.

62. Xue, X. S.; Jamieson, C. S.; Garcia-Borràs, M.; Dong, X.; Yang, Z.; Houk, K. N. Ambimodal Trispericyclic Transition State and Dynamic Control of Periselectivity. *J. Am. Chem. Soc.* **2019**, *141* (3), 1217–1221. https://doi.org/10.1021/jacs.8b12674.

63. Yang, Z.; Jamieson, C. S.; Xue, X.-S.; Garcia-Borràs, M.; Benton, T.; Dong, X.; Liu, F.; Houk, K. N. Mechanisms and Dynamics of Reactions Involving Entropic Intermediates. *J. Trends Chem.* **2019**, *1* (1), 22–34. https://doi.org/10.1016/j.trechm.2019.01.009.

64. Campos, R. B.; Tantillo, D. J. Designing Reactions with Post-Transition-State Bifurcations: Asynchronous Nitrene Insertions into C–C σ Bonds. *Chem* **2019**, *5* (1), 227–236. https://doi.org/10.1016/j.chempr.2018.10.019.

65. Liu, F.; Chen, Y.; Houk, K. N. Huisgen's 1,3-Dipolar Cycloadditions to Fulvenes Proceed via Ambimodal [6+4]/[4+2] Transition States. *Angew. Chem. Int. Ed. Engl.* **2020**, *59* (30), 12412–12416. https://doi.org/10.1002/anie.202005265.

66. Zhang, H.; Novak, A. J. E.; Jamieson, C. S.; Xue, X. S.; Chen, S.; Trauner, D.; Houk, K. N. Computational Exploration of the Mechanism of Critical Steps in the Biomimetic Synthesis of Preuisolactone A, and Discovery of New Ambimodal (5 + 2)/(4 + 2) Cycloadditions. *J. Am. Chem. Soc.* **2021**, *143* (17), 6601–6608. https://doi.org/10.1021/jacs.1c01856.

67. Zhang, H.; Thøgersen, M. K.; Jamieson, C. S.; Xue, X.-S.; Jørgensen, K. A.; Houk, K. N. Ambimodal Transition States in Diels–Alder Cycloadditions of Tropolone and Tropolonate with N-Methylmaleimide. *Angew. Chem. Int. Ed.* **2021**, *60* (47), 24991-24996. https://doi.org/10.1002/anie.202109608.

68. Zou, Y.; Houk, K. N. Mechanisms and Dynamics of Synthetic and Biosynthetic Formation of Delitschiapyrones: Solvent Control of Ambimodal Periselectivity. *J. Am. Chem. Soc.* **2021**, *143* (30), 11734–11740. https://doi.org/10.1021/jacs.1c05293.

3. Kinetic Analysis including dynamical bifurcations

69. Kpante, M.; Wolf, L. M. Pathway Bifurcations in the Activation of Allylic Halides by Palladium and Their Influence on the Dynamics of η^1 and η^3 Allyl Intermediates. *J. Org. Chem.* **2021**, *86* (14), 9637–9650. https://doi.org/10.1021/acs.joc.1c00891.

70. Hong, Y. J.; Tantillo, D. J. Biosynthetic Consequences of Multiple Sequential Post-Transition-State Bifurcations. *Nat. Chem.* **2014**, *6* (2), 104–111. https://doi.org/10.1038/nchem.1843.

71. Wang, X.; Zhang, C.; Jiang, Y.; Wang, W.; Zhou, Y.; Chen, Y.; Zhang, B.; Tan, R. X.; Ge, H. M.; Yang, Z. J.; Liang, Y. Influence of Water and Enzyme on the Post-Transition State Bifurcation of NgnD-Catalyzed Ambimodal [6+4]/[4+2] Cycloaddition. *J. Am. Chem. Soc.* **2021**. https://doi.org/10.1021/jacs.1c10760.

72. Harabuchi, Y.; Ono, Y.; Maeda, S.; Taketsugu, T. Analyses of Bifurcation of Reaction Pathways on a Global Reaction Route Map: A Case Study of Gold Cluster Au_5. *J. Chem. Phys.* **2015**, *143* (1), 014301. https://doi.org/10.1063/1.4923163.

73. Tantillo, D. J. Dynamic Effects on Organic Reactivity—Pathways to (and From) Discomfort. *J. Phys. Org. Chem.* **2021**, *34* (6), e4202. https://doi.org/10.1002/poc.4202.

74. Ito, T.; Harabuchi, Y.; Maeda, S. AFIR Explorations of Transition States of Extended Unsaturated Systems: Automatic Location of Ambimodal Transition States. *Phys. Chem. Chem. Phys.* **2020**, *22* (25), 13942–13950. https://doi.org/10.1039/D0CP02379E.

75. Sumiya, Y.; Maeda, S. A Reaction Path Network for Wöhler's Urea Synthesis. *Chem. Lett.* **2019**, *48* (1), 47–50. https://doi.org/10.1246/cl.180850.

76. Maeda, S.; Sugiyama, K.; Sumiya, Y.; Takagi, M.; Saita, K. Global Reaction Route Mapping for Surface Adsorbed Molecules: A Case Study for H_2O on Cu(111) Surface. *Chem. Lett.* **2018**, *47* (4), 396–399. https://doi.org/10.1246/cl.171194.

77. Chaia, J. D.; Head-Gordon, M. Long-range corrected hybrid density functionals with damped atom-atom dispersion corrections. *Phys. Chem. Chem. Phys.* **2008**, 10, 6615-6620. https://doi.org/10.1039/B810189B.

78. Linder, M.; Brinck, T. On the method-dependence of transition state asynchronicity in Diels-Alder reactions. P*hys. Chem. Chem. Phys.* **2013**, 15, 5108-5114. https://pubs.rsc.org/en/content/articlelanding/2013/cp/c3cp44319a

79. Truhlar, D. G.; Garret, B. C. Variational Transition-State Theory. *Acc. Chem. Res.* **1980**, 13 (12), 440-448. https://doi.org/10.1021/ar50156a002.

80. Frisch, M. J.; Trucks, G. W.; Schlegel, H. B.; Scuseria, G. E.; Robb, M. A.; Cheeseman, J. R.; Scalmani, G.; Barone, V.; Petersson, G. A.; Nakatsuji, H.; Li, X.; Caricato, M.; Marenich, A. V.; Bloino, J.; Janesko, B. G.; Gomperts, R.; Mennucci, B.; Hratchian, H. P.; Ortiz, J. V.; Izmaylov, A. F.; Sonnenberg, J. L.; Williams, Y. D.; Ding F.; Lipparini, F.; Egidi, F.; Goings, J.; Peng, B.; Petrone, A.; Henderson, T.; Ranasinghe, D.; Zakrzewski, V. G.; Gao, J.; Rega, N.; Zheng, G.; Liang, W.; Hada,

M.; Ehara, M.; Toyota, K.; Fukuda, R.; Hasegawa, J.; Ishida, M.; Nakajima, T.; Honda, Y.; Kitao, O.; Nakai, H.; Vreven, T.; Throssell, K.; Montgomery Jr., J. A.; Peralta, J. E.; Ogliaro, F.; Bearpark, M. J.; Heyd, J. J.; Brothers, E. N.; Kudin, K. N.; Staroverov, V. N.; Keith, T. A.; Kobayashi, R.; Normand, J.; Raghavachari, K.; Rendell, A. P.; Burant, J. C.; Iyengar, S. S.; Tomasi, J.; Cossi, M.; Millam, J. M.; Klene, M.; Adamo, C.; Cammi, R.; Ochterski, J. W.; Martin, R. L.; Morokuma, K.; Farkas, O.; Foresman, J. B.; Fox, D. J. *Gaussian16 Rev. B.01*; Gaussian, Incorp.: Wallingford, CT, 2016.

81. Maeda, S.; Harabuchi, Y.; Sumiya, Y.; Takagi, M.; Suzuki, K.; Sugiyama, K.; Ono, Y.; Hatanaka, M.; Osada, Y.; Taketsugu, T.; Morokuma, K.; Ohno, K.; *GRRM (A Developmental Version)*; Hokkaido University, 2021.

82. Yang, Z.; Dong, X.; Yu, Y.; Yu, P.; Li, Y.; Jamieson, C.; Houk, K. N. Relationships between Product Ratios in Ambimodal Pericyclic Reactions and Bond Lengths in Transition Structures. *J. Am. Chem. Soc.* **2018**, *140* (8), 3061–3067. https://doi.org/10.1021/jacs.7b13562.

4. Machine learning assisted kinetic analysis of reaction path networks including dynamical bifurcations

4.1 Introduction

Chemical reactions are analyzed theoretically based on the potential energy surface (PES). Reactants, intermediates, and products corresponding to minima (MINs) on the PES, and transition states (TSs) correspond to the first order saddle points on the PES. The intrinsic reaction coordinate (IRC) is widely used to characterize reaction paths (1-3). An IRC path is defined as a steepest descent path in mass-weighted coordinate from a TS. The transition state theory (4-5) gives a rate constant for an elementary reaction represented by an IRC path. Recent development of automated reaction path search methods such as the artificial force induced reaction (AFIR) method has enabled to construct a reaction path network, in which several MINs on the PES are connected by IRC paths (6). By solving rate equations for a reaction path network, kinetic simulations considering all possible elementary process has also become possible.

This analysis based on the PES is very efficient to investigate reaction mechanisms but does not include the effect of nuclear momentum (7). Dynamical bifurcations are phenomena in which ensemble of trajectories passing through a TS bifurcate to multiple MINs (8,9). The IRC path cannot describe a dynamical bifurcation because it does not bifurcate. Therefore, theoretical analyses based on reaction path networks give incorrect conclusions for reactions including dynamical bifurcations.

4. Machine learning assisted kinetic analysis

To solve this problem, I have developed a method to perform a kinetic analysis for a reaction path network including dynamical bifurcations (10). This method consists of three methods; an automated method to search for dynamical bifurcations using the AFIR method (11), ab initio molecular dynamics (AIMD) simulations to compute branching ratio, and a method to incorporate branching ratio (12) into rate constants. This method showed that the dynamic effect is important in reaction selectivity in an intramolecular Diels-Alder reaction. However, the method requires massive AIMD trajectory calculations, which makes the method difficult to apply large reaction path networks including several dynamical bifurcations. Therefore, a method to estimate branching ratios without AIMD calculations is necessary.

In 1992, Carpenter proposed a simple model to predict branching ratio for the first time (13). Carpenter supposed that the direction of eigenvector corresponding to the imaginary frequency relates to the branching ratio, and a model to estimate branching ratio by computing inner products between the imaginary frequency vector and a vector from the TS to each product MINs. In 2018, Houk et al. reported that there is a relationship between branching ratio of dynamical bifurcations for cycloadditions and differences between lengths of two bonds related to two products (14). In 2020, Goodman et al. proposed a model which assumed that trajectories passing through a TS go straight along the imaginary frequency mode and trajectories bifurcate at a TS connecting two products in two-dimensional internal coordinate space (15). In 2021, Srnec et al. proposed a model to predict branching ratio based on the kinetic energy at the TS (16). However, three models except for Carpenter's model use the information of breaking and forming bonds during the reaction, which

makes it difficult to apply the model to reaction path network including MINs for which it is difficult to define bonds. In dynamical bifurcations, the shape of PES decides the trajectories, and therefore it is expected that the branching ratio can be estimated without bond information by using the information of PES. Instead, this study aims at constructing a machine learning (ML) model for prediction of branching ratios based on the PES and applying it to the kinetic analysis of reaction path networks.

4.2 Methodology

4.2.1 Descriptors for machine learning

The constructed model predicts a branching ratio by AIMD calculation for a dynamical bifurcation using the information about four geometries; a TS from which the dynamical bifurcation occurs (TS_r), MINs for two products (MIN_{P1} and MIN_{P2}), and a TS connecting MIN_{P1} and MIN_{P2} (TS_i). Next, descriptors used in this study is explained. At first, two unit vectors $\mathbf{e}_{x_1}$ and $\mathbf{e}_{x_2}$. are generated by performing Gram-Schmidt orthonormalization to the two imaginary frequency vectors for TS_i and TS_r. Then, four geometries TS_r, TS_i, MIN_{P1} and MIN_{P2} are projected to a two-dimensional space constructed by $\mathbf{e}_{x_1}$ and $\mathbf{e}_{x_2}$. In this time, the coordinate for TS_r is set to (0,0), and $\mathbf{e}_{x_1}$ and $\mathbf{e}_{x_2}$ are appropriately reversed so that x_1 for MIN_{P1} is always positive, and x_2 for MIN_{P1} is always larger than x_2 for MIN_{P2} for each reaction. And x_1 and x_2 for TS_i, MIN_{P1} and MIN_{P2} are used as descriptors. In addition, potential energies for TS_i, MIN_{P1} and MIN_{P2} relative to that for TS_r and the number of atoms are used as descriptors.

4.2.2 Application to the automated search for dynamical bifurcations

Here, a procedure to apply the constructed model is described. Currently, reaction path networks generated by AFIR method are sometimes not composed by IRC paths to reduce the computational cost (17). Instead of IRC paths, paths traced by the AFIR method (called AFIR paths) are relaxed by the locally updated plane (LUP) method to give so called LUP paths, which is used to construct reaction path networks. Normally, the energy maximum of a LUP path called a path top (PT) is not the actual TS. The previously developed automated dynamical bifurcation search method cannot be applied to LUP-based reaction path networks since the method judges sets of AFIR paths giving a common TS as dynamical bifurcations (11). Therefore, this study introduces a scheme to search for dynamical bifurcations for a LUP-based reaction path network based on the ML model.

Normally, dynamical bifurcations giving two products are hidden as a pair of two LUP paths, one connects a reactant MIN and a product MIN, and the other connects the product MIN and another MIN corresponding to the bifurcation product. This scheme finds all possible pairs of LUP paths and apply the ML model to compute branching ratios for them. Finally, the kinetic analysis mentioned above is applied using the computed branching ratios. This scheme automatically excludes non-dynamical bifurcations because the branching ratio is predicted as 1.0:0.0. In other words, this scheme performs the automated search for dynamical bifurcations and Prediction of branching ratios simultaneously.

Figure 4.1 shows an example using a model network in which 5 minima are connected by 5 PTs. Let’s consider examining the occurrence of dynamical bifurcations from PT1. There are three

pairs of LUP paths; PT1 and PT2, PT1 and PT3, and PT1 and PT4. Then, branching ratios for the three pairs using the ML model. Finally, three branching ratios are merged into an overall branching ratio. In this case, the branching ratio of MIN5 is zero, which indicates that no trajectories would reach MIN5.

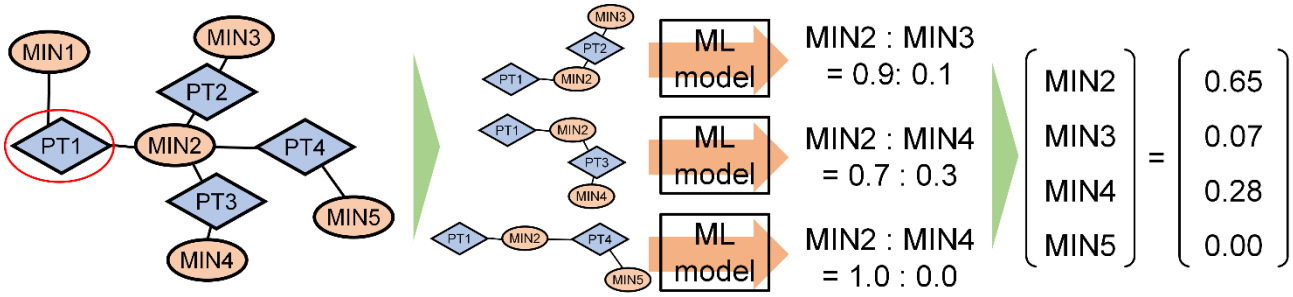

Figure 4.1. A schematic picture explaining the scheme of the network analysis using the machine learning model.

4.3 Computational Details

4.3.1 Construction of the dataset

50 reactions collected by Goodman et al. (15) are used as a dataset. TS_r, TS_i, MIN_{P1} and MIN_{P2} for each reaction were optimized. IRC calculations were performed from optimized TSs, and 5 reactions whose IRC paths does not connect desired geometries were excluded from the dataset. Then, descriptors described above were computed for these reactions. As objective variables, branching ratios computed from AIMD calculations in previous reports are used. In addition, dataset includes two data for one reaction, because there are two options about which MIN should be assigned

as MIN_{P1}. In summary, the dataset including 90 data were finally obtained. The quantum chemical methods were decided depending on what methods are used in AIMD calculations in previous papers, as shown in **Table 4.1**. All electronic structure calculations were performed using Gaussian16 (18), and geometry optimizations were performed using the developer version of GRRM (19).

Table 4.1. Level of theories for 45 reactions used to construct a database.

Number	Reference	Level of theory
1	Houk2007 (20)	B3LYP/LanL2DZ (for Sn) 6-31+G(d) (for H, C, O, P and Cl)
2	Houk2007 (20)	B3LYP/LanL2DZ (for Sn) 6-31+G(d) (for H, C, O, P and Cl)
3	Houk2007 (20)	B3LYP/6-31+G*
4	Houk2007 (20)	B3LYP/6-31+G*
5	Houk2003 (21)	B3LYP/6-31G(d)
6	Houk2003 (21)	B3LYP/6-31G(d)
7	Houk2003 (21)	B3LYP/6-31G(d)
8	Houk2003 (21)	B3LYP/6-31G(d)
9	Singleton2008 (22)	MPW1K/6-31+G(d,p)
10	Singleton2008 (22)	MPW1K/6-31+G(d,p)
11	Singleton2008 (22)	MPW1K/6-31+G(d,p)
12	Singleton2008 (22)	MPW1K/6-31+G(d,p)
13	Yamataka2010 (23)	HF/6-31G(d)
14	Yamataka2010 (23)	HF/6-31G(d)
15	Yamataka2010 (23)	HF/6-31G(d)
16	Yamataka2011 (24)	B3LYP/6-31+G(d)
17	Yamataka2011 (24)	B3LYP/6-31+G(d)
18	Yamataka2011 (24)	B3LYP/6-31+G(d)
19	Yamataka2011 (24)	B3LYP/6-31+G(d)
20	Yamataka2011 (24)	B3LYP/6-31+G(d)
21	Yamataka2011 (24)	B3LYP/6-31+G(d)
22	Wang2009 (25)	B3LYP/6-311+G(d,p)
23	Singleton2005 (26)	B3LYP/6-311+G(d,p)
24	Singleton2006 (27)	MPW1K/6-31+G(d,p)
25	Singleton2006 (27)	MPW1K/6-31+G(d,p)
26	Houk2017 (28)	B3LYP/6-31G(d)

27	Houk2018 (29)	B3LYP/6-31+G(d,p)
28	Houk2018 (29)	B3LYP/6-31+G(d,p)
29	Houk2018 (29)	B3LYP/6-31+G(d,p)
30	HoukNature (30)	B3LYP/6-31G(d)
31	Zhang2012 (31)	M06/LanL2DZ (for Au) 6-31+G(d) (for H, C and P)
32	Tantillo2019 (32)	B3LYP/6-31+G(d,p)
33	Tantillo2019 (32)	B3LYP/6-31+G(d,p)
34	Tantillo2019 (32)	B3LYP/6-31+G(d,p)
35	Tantillo2019 (32)	B3LYP/6-31+G(d,p)
36	Tantillo2010 (33)	B3LYP/6-31+G(d,p)
37	Tantillo2019-2 (34)	B3LYP/6-31G(d)
38	Tantillo2019-2 (34)	B3LYP/6-31G(d) SCRF=(PCM,Solvent=Toluene)
39	Tantillo2019-2 (34)	B3LYP/6-31G(d) SCRF=(PCM,Solvent=1-Butanol)
40	Tantillo2019-2 (34)	B3LYP/6-31G(d) SCRF=(PCM,Solvent=n,n-DiMethylFormamide)
41	Tantillo2019-2 (34)	B3LYP/6-31G(d) SCRF=(PCM,Solvent=Water)
42	Datta2018 (35)	B3LYP/6-31G(d)
43	SilvaLopez2017 (36)	UM062X/Def2SVP
44	SilvaLopez2017 (36)	UM062X/Def2SVP
45	Singleton2012 (37)	B3LYP/6-31+G(d,p)

4.3.2 Details about machine learning

The random forest regression (RFR) model (38) and the support vector regression (SVR) (39) model were used in this study. Hyperparameters for each model was decided based on the grid search. In the RFR model, “None” was used as max_depth, “sqrt” was used as max_features, 1 as used as min_sample_leafs, 2 as used as min_sample_split, and 75 was used as n_estimators. In the SVR model, 10.0 was used as C, 0.001 was used as epsilon, “scale” was used as gamma, and “rbf” was used as kernel. When evaluating hyperparameters, training using the 72 random data and computation of R^2 score using the rest 18 data were repeated five times, and the average of R^2 score was used to evaluate each model. RFR and SVR were performed using Python (ver. 3.11) and scikit

learn (ver. 1.3.0) (40).

4.4 Results

4.4.1 Two dimensional descriptors

Figure 4.2 shows plots of TS_r, TS_i, MIN_{P1} and MIN_{P2} for four example reactions in x_1-x_2 space, in which x_1 corresponds to the imaginary frequency mode for TS_r, and x_2 corresponds to the vibrational mode perpendicular to x_1. **Example 1** is a a deazetization reaction giving two symmetrically equivalent semibullvalenes (35), **example 2** is a Diels-Alder reaction between 2-vinylfuran and 3-methoxycarbonylcyclopentadienone (22), **example 3** is an asymmetric cycloaddition reaction including proton transfer (29), and **example 4** is a Schmidt reaction (23). The plot for **example 1** shown in **Figure 4.2a** indicates that x_2 of both TS_r and TS_i are zero, and the points for MIN_{P1} and MIN_{P2} are symmetrical about x_1-axis. This corresponds to the fact the PES is symmetrical and the two products are obtained in equal amounts. In contrast to **example 1**, the plots for the other three reactions shown in **Figure 4.2b-d** are asymmetrical, which is consistent with the fact that the branching ratios for **example 2-4** are not equivalent. In addition, the points for both MIN_{P1} and MIN_{P2} are located in $x_2 > 0$ only for **example 4**. This seems to be because the reaction path is highly curved and linear coordinate transformation does not work well to describe this reaction.

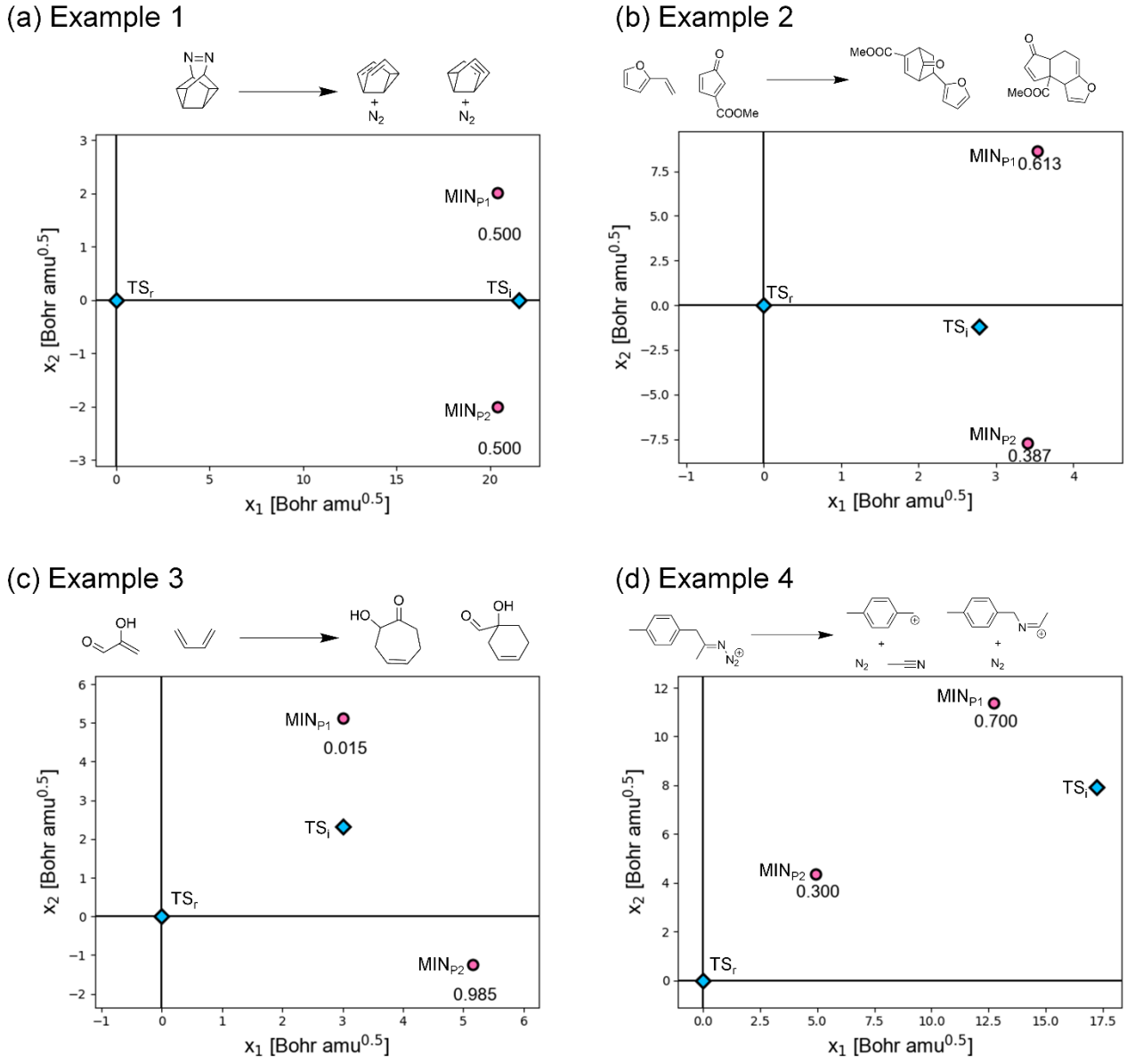

Figure 4.2. Plots of TS_r, TS_i, MIN_{P1} and MIN_{P2} for four example reactions in x_1-x_2 space. Pink circles and blue diamonds represent TSs and MINs, respectively. Branching ratios are also shown on the plots.

4.4.2 Performance of machine learning models

Next, the ML models were trained using the descriptors computed above. The averaged R^2 scores for the best hyperparameters are 0.41 for SVR and 0.60 for RFR. In the following, the

RFR model which gives better score than SVR was discussed. In **Figure 4.3,** the predicted branching ratios of P_1 for train data and test data are plotted against the actual branching ratios. The 90 data was randomly split to train data and test data five times, and **Figure 4.3a** shows the case for the best R^2 score, while **Figure 4.3b** shows the case for the worst R^2 score. For the best case, the model predicts well even for the test data, which was not used for training. On the other hand, in the worst case, the predict ratios tended to be close to 0.5.

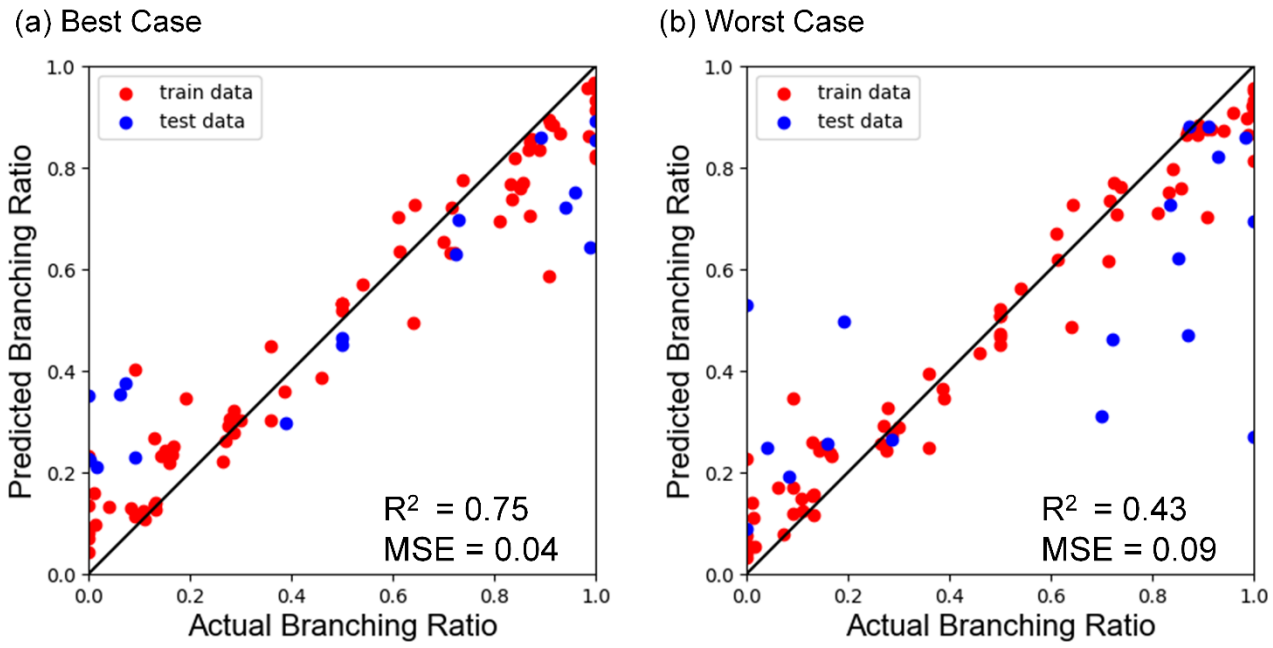

Figure 4.3. Plots for the predicted branching ratios of P_1 for train data and test data against the actual branching ratios. (a) shows the plot for the best case and (b) shows that for the worst case. Red points are for the train data, while blue points are for the test data.

Next, the importance of descriptors was evaluated in **Figure 4.4**. **Figure 4.4** indicates that x_2 of TS_i is quite important to predict branching ratios. This can be understood as follows. Ensemble

of trajectories passing through TS_r bifurcates when reaching to TS_i, which corresponds to a dividing surface of two products. For symmetrical reactions like **example 1** in **Figure 4.1**, trajectories bifurcate at TS_i in equal amounts because x_2 of TS_i is equal to that of TS_r. On the other hand, in reactions in which x_2 of TS_i is smaller than that of TS_r, like **example 2**, more trajectories reach the P_1 side of TS_i, which makes P_1 the major product. Similarly, reactions in which x_2 of TS_i is larger than that of TS_r, like **example 3** corresponds to the excess of P_2. In this reason, x_2 of TS_i has a significant effect on branching ratio.

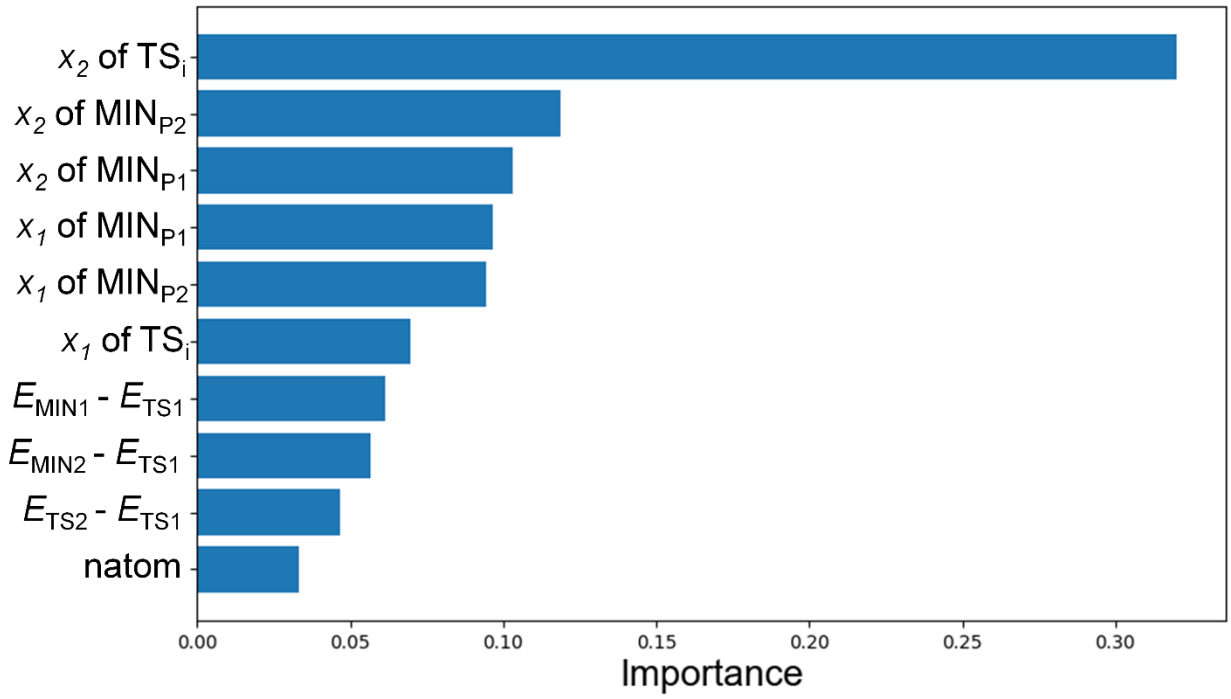

Figure 4.4. A bar graph showing the importance of each descriptor.

4.4.3 Application to reaction path networks

The constructed ML model was applied to the kinetic analysis of reaction path networks. At first, a reaction path network for an intramolecular reaction (21) studied in my previous study (41)

was reanalyzed by using the ML model. **Figure 4.5** shows the result for this reaction. This reaction gives two products, the (4+2) product and the (2+2) product from a reactant shown in **Figure 4.5a**, and the experimental selectivity of (4+2):(2+2) was 3.5:1.0. In **Figure 4.5b**, the reaction path network at ωB97X-D/6-31+G(d) level is shown. As shown in **Figure 4.5c**, the automated search method based on the AFIR method found two dynamical bifurcations. **Figure 4.5c** also shows that branching ratios computed by AIMD calculations and the ML model. The AIMD calculations showed that the (4+2) product was major for the two dynamical bifurcations, which was successfully reproduced by the present ML model. In addition, the ML model reproduced the trend that more AIMD trajectories from TS2 reached the (2+2) product than those from TS1. Finally, the kinetic analysis based on the rate constant matrix contraction method was performed based using the branching ratios predicted by the branching ratio. **Figure 4.5d** shows the plot of populations of chemical species in the network against time. In the plot, the reactant has a population of 1.0, and then reaction occurred to give the (4+2) product and (2+2) product with populations of 0.93 and 0.07, which is qualitatively consistent with the experiment (25). In summary, the kinetic analysis of a reaction path network including dynamical bifurcations without the AIMD calculations was realized using the ML model.

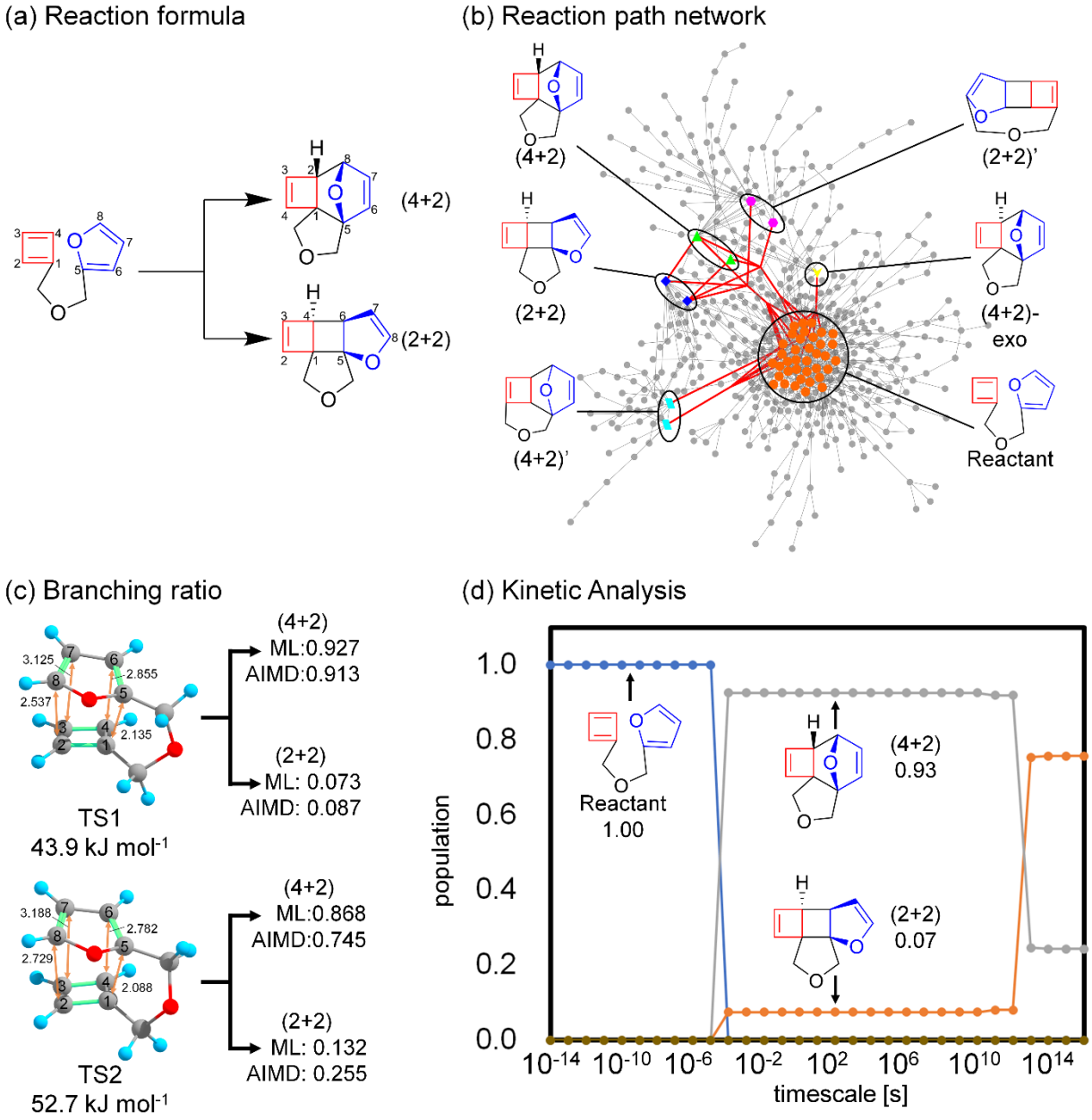

Figure 4.5. The results analyzed by the machine learning model for an intramolecular Diels-Alder reaction. (a) show a reaction formula for this reaction. (b) shows a reaction path network. Structural formulae for some compounds are also shown. (c) shows dynamical bifurcations included in the network. Branching ratios based on the machine learning model or ab initio molecular dynamics simulations are also shown. (d) shows a plot for populations of each chemical species included in the network against time.

4. Machine learning assisted kinetic analysis

Finally, a reaction path network for retrosynthesis of difluoroglycine (42) was analyzed and summarized in **Figure 4.6**. **Figure 4.6b** shows the reaction path network at ωB97X-D/def2-SV(P) level. The solvent effect of THF is included using the SMD model. The network was computed to search for all reactant candidates yielding difluoroglycine kinetically, and the experimental reaction design has been performed based on this network (42) (**Figure 4.6a**). Hereafter, the analysis was performed focusing one of the reactants shown in the right of **Figure 4.6c**. The reactant gives difluoroglycine through a series of reaction paths shown in **Figure 4.6d**. Because the network is constructed based on LUP paths, the ML-based analysis mentioned in the methodology section was applied. It was found that the reaction yield of difluoroglycine from the reactant was 0.83 (83 %) without dynamical bifurcations, while that with dynamical bifurcations was 0.73 (73 %). This indicates that the effect of dynamical bifurcations decreased the yield. These results showed that the effect of dynamical bifurcations was important even for the reaction path network used in the recent reaction design.

Figure 4.6d shows one of the dynamical bifurcations occurred in reaction paths shown in **Figure 4.6c**. 10 AIMD trajectories were computed for this dynamical bifurcation, and it was found that all trajectories reached to P_1. This indicates that the ML model sometimes regards a non-dynamical bifurcation as a dynamical bifurcation, probably because the dataset used in training does not include non-dynamical bifurcations. Therefore, the ML model should be improved by including non-dynamical bifurcations in future study.

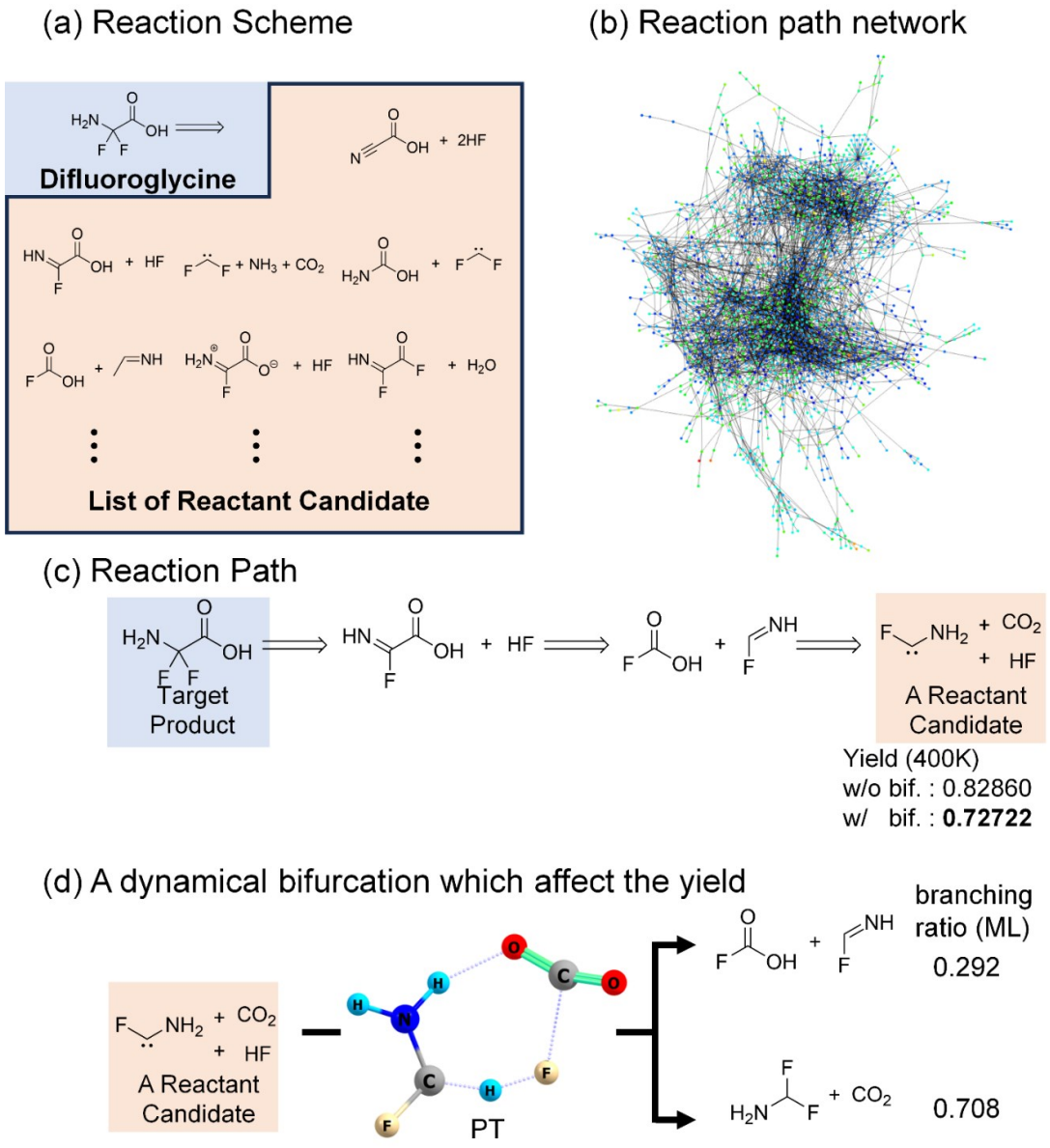

Figure 4.6. The results analyzed by the machine learning model for retrosynthesis of difluoroglycine. (a) shows a reaction scheme for retrosynthesis of difluoroglycine, (b) shows a reaction path network for retrosynthesis of difluoroglycine, (c) shows a series of reaction paths from reactants to difluoroglycine, and (d) shows a dynamical bifurcation which affect the yield of difluoroglycine from the reactant.

4.5 Conclusion

This study aims at developing a ML model to predict branching ratios to accelerate the kinetic analysis of reaction path network including dynamical bifurcations. The constructed model predicts branching ratios based on four geometries, TS_r, TS_i, MIN_{P1} and MIN_{P2}. The ML model was first applied to a reaction path network for an intramolecular Diels-Alder reaction. It was found that the experimental yield was reproduced using the kinetic analysis using the ML model. In addition, a scheme to perform the automated search for dynamical bifurcations and computation of branching ratio simultaneously was proposed to analyze LUP-based reaction path networks. This scheme was applied to a reaction path network for retrosynthesis of difluoroglycine, and it was found that the effect of dynamical bifurcations was important even for the reaction path network used in the recent reaction design. On the other hand, the limit of the ML model was also revealed. In the future, it is hoped to improve the accuracy of the ML model by including non-dynamical bifurcations in the dataset.

4.6 Reference

1. Fukui, K. Formulation of the Reaction Coordinate. *J. Phys. Chem.* **1970**, *74* (23), 4161–4163. https://doi.org/10.1021/j100717a029.

2. Fukui, K. The Path of Chemical Reactions - The IRC Approach. *Acc. Chem. Res.* **1981**, *14* (12), 363–368. https://doi.org/10.1021/ar00072a001.

3. Maeda, S.; Harabuchi, Y.; Ono, Y.; Taketsugu, T.; Morokuma, K. Intrinsic Reaction Coordinate: Calculation, Bifurcation, and Automated Search. *Int. J. Quantum Chem.* **2015**, 115 (5), 258−269. https://doi.org/10.1002/qua.24757.

4. Fernández-Ramos, A.; Miller, J. A.; Klippenstein, S. J.; Truhlar, D. G. Modeling the Kinetics of Bimolecular Reactions. *Chem. Rev.* **2006**, *106* (11), 4518–4584. https://doi.org/10.1021/cr050205w.

5. Klippenstein, S. J.; Pande, V. S.; Truhlar, D. G. Chemical Kinetics and Mechanisms of Complex Systems: A Perspective on Recent Theoretical Advances. *J. Am. Chem. Soc.* **2014**, *136* (2), 528–546. https://doi.org/10.1021/ja408723a.

6. Maeda, S.; Ohno, K.; Morokuma K. Systematic exploration of the mechanism of chemical reactions: the global reaction route mapping (GRRM) strategy using the ADDF and AFIR methods. *Phys. Chem. Chem. Phys.* **2013**, 15, 3683–3701. https://doi.org/10.1039/C3CP44063J.

7. Carpenter, B.K. NONSTATISTICAL DYNAMICS IN THERMAL REACTIONS OF POLYATOMIC MOLECULES. *Annu. Rev. Phys. Chem.* **2005**. 57–89. https://doi.org/10.1146/annurev.physchem.56.092503.141240.

8. Ess, D. H.; Wheeler, S. E.; Iafe, R. G.; Xu, L.; Çelebi-Ölçüm, N.; Houk, K. N. Bifurcations on Potential Energy Surfaces of Organic Reactions. *Angew. Chem. Int. Ed. Engl.* **2008**, *47* (40), 7592–7601. https://doi.org/10.1002/anie.200800918.

9. Hare, S. R.; Tantillo, D. J. Post-Transition State Bifurcations Gain Momentum – Current State of the Field, *J. Pure Appl. Chem.* **2017**, *89* (6), 679−698. https://doi.org/10.1515/pac-2017-0104.

10. Ito, T.; Maeda, S.; Harabuchi, Y. Kinetic Analysis of a Reaction Path Network Including Ambimodal Transition States: A Case Study of an Intramolecular Diels−Alder Reaction. *J. Chem. Theory Comput.* **2022**, 18, 1663−1671. https://doi.org/10.1021/acs.jctc.1c01297.

11. Ito, T.; Harabuchi, Y.; Maeda, S. AFIR Explorations of Transition States of Extended Unsaturated Systems: Automatic Location of Ambimodal Transition States. *Phys. Chem. Chem. Phys.* **2020**, *22* (25), 13942–13950. https://doi.org/10.1039/D0CP02379E.

12. Rehbein, J.; Carpenter, B. K. Do We Fully Understand What Controls Chemical Selectivity? *Phys. Chem. Chem. Phys.* **2011**, *13* (47), 20906–20922. https://doi.org/10.1039/c1cp22565k.

13. Peterson, T. H.; Carpenter, B. K. Estimation of dynamic effects on product ratios by vectorial decomposition of a reaction coordinate. Application to thermal nitrogen loss from bicyclic azo compounds. *J. Am. Chem. Soc.* **1992**, 114, 766–767. https://doi.org/10.1021/ja00028a057.

14. Yang, Z.; Dong, X.; Yu, Y.; Yu, P.; Li, Y.; Jamieson, C.; Houk, K. N. Relationships between Product Ratios in Ambimodal Pericyclic Reactions and Bond Lengths in Transition Structures. J. Am. Chem. Soc. 2018, 140 (8), 3061–3067. https://doi.org/10.1021/jacs.7b13562.

15. Lee, S.; Goodman, J. M. Rapid Route-Finding for Bifurcating Organic Reactions. *J. Am. Chem. Soc.* **2020**, 142, 9210−9219. https://doi.org/10.1021/jacs.9b13449.

16. Bharadwaz, P.; Maldonado-Domínguez, M.; Srnec, M. Bifurcating reactions: distribution of

products from energy distribution in a shared reactive mode. *Chem. Sci.*, **2021**, 12, 12682−12694. https://doi.org/10.1039/d1sc02826j.

17. Maeda, S.; Harabuchi, Y. Exploring paths of chemical transformations in molecular and periodic systems: An approach utilizing force. *WIREs Comput Mol Sci.* **2021**, 11, e1538. https://doi.org/10.1002/wcms.1538.

18. Frisch, M. J.; Trucks, G. W.; Schlegel, H. B.; Scuseria, G. E.; Robb, M. A.; Cheeseman, J. R.; Scalmani, G.; Barone, V.; Petersson, G. A.; Nakatsuji, H.; Li, X.; Caricato, M.; Marenich, A. V.; Bloino, J.; Janesko, B. G.; Gomperts, R.; Mennucci, B.; Hratchian, H. P.; Ortiz, J. V.; Izmaylov, A. F.; Sonnenberg, J. L.; Williams, Y. D.; Ding F.; Lipparini, F.; Egidi, F.; Goings, J.; Peng, B.; Petrone, A.; Henderson, T.; Ranasinghe, D.; Zakrzewski, V. G.; Gao, J.; Rega, N.; Zheng, G.; Liang, W.; Hada, M.; Ehara, M.; Toyota, K.; Fukuda, R.; Hasegawa, J.; Ishida, M.; Nakajima, T.; Honda, Y.; Kitao, O.; Nakai, H.; Vreven, T.; Throssell, K.; Montgomery Jr., J. A.; Peralta, J. E.; Ogliaro, F.; Bearpark, M. J.; Heyd, J. J.; Brothers, E. N.; Kudin, K. N.; Staroverov, V. N.; Keith, T. A.; Kobayashi, R.; Normand, J.; Raghavachari, K.; Rendell, A. P.; Burant, J. C.; Iyengar, S. S.; Tomasi, J.; Cossi, M.; Millam, J. M.; Klene, M.; Adamo, C.; Cammi, R.; Ochterski, J. W.; Martin, R. L.; Morokuma, K.; Farkas, O.; Foresman, J. B.; Fox, D. J. *Gaussian16 Rev. B.01*; Gaussian, Incorp.: Wallingford, CT, 2016.

19. Maeda, S.; Harabuchi, Y.; Sumiya, Y.; Takagi, M.; Suzuki, K.; Sugiyama, K.; Ono, Y.; Hatanaka, M.; Osada, Y.; Taketsugu, T.; Morokuma, K.; Ohno, K.; *GRRM (A Developmental Version)*; Hokkaido University, 2023.

20. Celebi-Olçüm, N.; Ess, D. H.; Aviyente, V.; Houk, K. N. Lewis Acid Catalysis Alters the Shapes and Products of Bis-Pericyclic Diels-Alder Transition States. *J. Am. Chem. Soc.* **2007**, *129* (15), 4528–4529. https://doi.org/10.1021/ja070686w.

21. Limanto, J.; Khuong, K. S.; Houk, K. N.; Snapper, M. L. Intramolecular Cycloadditions of Cyclobutadiene with Dienes: Experimental and Computational Studies of the Competing (2 + 2) and (4 + 2) Modes of Reaction. *J. Am. Chem. Soc.* **2003**, *125* (52), 16310–16321. https://doi.org/10.1021/ja0380547.

22. Thomas, J. B.; Waas, J. R.; Harmata, M.; Singleton, D. A. Control Elements in Dynamically Determined Selectivity on a Bifurcating Surface. *J. Am. Chem. Soc.* **2008**, *130* (44), 14544–14555. https://doi.org/10.1021/ja802577v.

23. Katori, T.; Itoh, S.; Sato, M.; Yamataka, H. Reaction Pathways and Possible Path Bifurcation for the Schmidt Reaction, J. Am. Chem. Soc. **2010**, 132, 3413–3422. https://doi.org/10.1021/ja908899u.

24. Yamataka, H.; Sato, M.; Hasegawa, H.; Ammal, S. C. Dynamic path bifurcation for the Beckmann reaction: observation and implication. *Faraday Discuss.* **2010**, 145, 327–340.

https://doi.org/10.1039/B906159B.

25. Wang, Z.; Hirschi, J. S.; Singleton, D. A. Recrossing and Dynamic Matching Effects on Selectivity in a Diels-Alder Reaction. *Angew. Chem. Int. Ed. Engl.* **2009**, *48* (48), 9156–9159. https://doi.org/10.1002/anie.200903293.

26. Bekele, T.; Christian, C. F.; Lipton, M. A.; Singleton, D. A. "Concerted" Transition State, Stepwise Mechanism. DynamicsEffects in C^2-C^6 Enyne Allene Cyclizations. *J. Am. Chem. Soc.*, **2005**, 127, 9216−9223. https://doi.org/10.1021/ja0508673.

27. Ussing, B. R.; Hang, C.; Singleton, D. A. Dynamic Effects on the Periselectivity, Rate, Isotope Effects, and Mechanism of Cycloadditions of Ketenes with Cyclopentadiene. *J. Am. Chem. Soc.* **2006**, 128, 7594−7607. https://doi.org/10.1021/ja0606024.

28. Yu, P.; Chen, T. Q.; Yang, Z.; He, C. Q.; Patel, A.; Lam, Y. H.; Liu, C. Y.; Houk, K. N. Mechanisms and Origins of Periselectivity of the Ambimodal [6 + 4] Cycloadditions of Tropone to Dimethylfulvene. *J. Am. Chem. Soc.* **2017**, *139* (24), 8251–8258. https://doi.org/10.1021/jacs.7b02966.

29. Chen, S.; Yu, P.; Houk, K. N. Ambimodal Dipolar/Diels–Alder Cycloaddition Transition States Involving Proton Transfers. *J. Am. Chem. Soc.* **2018**, *140* (51), 18124–18131. https://doi.org/10.1021/jacs.8b11080.

30. Ohashi, M.; Liu, Hai, F. Y.; Chen, M.; Tang, M.; Yang, Z.; Sato, M.; Watanabe, K.; Houk, K. N.; Tang, Y. SAM-dependent enzyme-catalysed pericyclic reactions in natural product biosynthesis.

Nature **2017**, 549, 502–506. https://doi.org/10.1038/nature23882.

31. Ye, L.; Wang, Y.; Aue, D. H.; Zhang, L. Experimental and Computational Evidence for Gold Vinylidenes: Generation from Terminal Alkynes via a Bifurcation Pathway and Facile C−H Insertions. J. Am. Chem. Soc. **2012**, 134, 31−34. https://doi.org/10.1021/ja2091992.
32. Campos, R. B.; Tantillo, D. J. *Chem* Designing Reactions with Post-Transition-State Bifurcations: Asynchronous Nitrene Insertions into C–C σ Bonds. **2019**, 5, 227–236. https://doi.org/10.1016/j.chempr.2018.10.019.
33. Hong, Y. J.; Tantillo, D. J. Quantum chemical dissection of the classic terpinyl/pinyl/bornyl/camphyl cation conundrum—the role of pyrophosphate in manipulating pathways to monoterpenes. *Org. Biomol. Chem.* **2010**, 8, 4589–4600. https://doi.org/10.1039/C0OB00167H.
34. Hare, S. R.; Li, A.; Tantillo, D. J. Post-transition state bifurcations induce dynamical detours in Pummerer-like reactions. *Chem. Sci.* **2018**, 9, 8937–8945. https://doi.org/10.1039/C8SC02653J.
35. Mandal, N.; Datta, A. Dynamical Effects along the Bifurcation Pathway Control Semibullvalene Formation in Deazetization Reactions. *J. Phys. Chem. B* **2018**, 122, 1239−1244. https://doi.org/10.1021/acs.jpcb.7b09533.
36. López, R. V.; Faza, O. N.; López, C. S. Dynamic Effects Responsible for High Selectivity in a [3,3] Sigmatropic Rearrangement Featuring a Bispericyclic Transition State. *J. Org. Chem.* **2017**, 82 (9), 4758–4765. https://doi.org/10.1021/acs.joc.7b00425.

37. Bogle, X. S.; Singleton, D. A. Dynamic Origin of the Stereoselectivity of a Nucleophilic Substitution Reaction. *Org. Lett.* **2012**, 14, 2528−2531. https://doi.org/10.1021/ol300817a.

38. Breiman, L. Random Forests. *Machine Learning*. **2001**, 45, 5−32. https://doi.org/10.1023/A:1010933404324.

39. Cortes, C.; Vapnik, V. Support-vector networks. *Machine Learning*. **1995**, 20, 273−297. https://doi.org/10.1007/BF00994018.

40. Pedregosa, F.; Varoquaux, G.; Gramfort, A.; Michel, V.; Thirion, B.; Grisel, O.; Blondel, M.; Prettenhofer, P.; Weiss, R.; Dubourg, V.; Vanderplas, J.; Passos, A.; Cournapeau, D.; Brucher, M.; Perrot, M.; Duchesnay, É. Scikit-learn: Machine learning in Python. *J. Mach. Learn. Res.* **2011**, 12, 2825−2830.

41. Ito, T.; Maeda, S.; Harabuchi, Y. Kinetic Analysis of a Reaction Path Network Including Ambimodal Transition States: A Case Study of an Intramolecular Diels−Alder Reaction. *J. Chem. Theory Comput.* **2022**, 18, 1663−1671. https://doi.org/10.1021/acs.jctc.1c01297.

42. Mita, T.; Harabuchi Y.; Maeda, S. Discovery of a synthesis method for a difluoroglycine derivative based on a path generated by quantum chemical calculations. *Chem. Sci.* **2020**, 11, 7569–7577. https://doi.org/10.1039/d0sc02089c.

5. An exploration of downhill bifurcations for [3,3]-sigmatropic rearrangement by finding the transition from an uphill bifurcation to a downhill bifurcation

5.1 Introduction

In recent years, dynamical bifurcation, in which an ensemble of trajectories passing through a transition state (TS) bifurcates into multiple minima, has attracted attention in various fields of chemistry (1–3). Dynamical bifurcation is sometimes called downhill bifurcation because the bifurcation occurs on the way down from the TS. In this case, there is only one TS despite two different products, and such TS is consequently called an ambimodal TS (4–5) .

Downhill bifurcations are characterized by a pair of reactions that occur simultaneously. In previous studies, downhill bifurcations have been observed for various reaction pairs (6–18) . Examples of these reaction pairs are pericyclic reactions such as two [4+2] cycloadditions (19), [4+2] and [2+2] cycloadditions (20), [4+2] and [6+4] cycloadditions (21), two [6+4] cycloadditions (22),two [3,3]-sigmatropic rearrangements (23), and others (24–26). However, downhill bifurcations have yet to be reported for many reaction pairs. Therefore, it would be interesting to explore the prevalence of downhill bifurcations in chemical reactions. Additionally, downhill bifurcations decrease the reaction yield of the target product (27) . Thus, exploring novel downhill bifurcations is also necessary from the viewpoint of achieving full control over chemical reactions.

In quantum chemistry, downhill bifurcations are located by analyzing the potential energy surface (PES). For example, the occurrence of a downhill bifurcation can be indicated by a point,

called valley–ridge transition (VRT) point, where the shape of the PES orthogonal to the intrinsic reaction coordinate (IRC) changes from a valley to a ridge (6,28). *Ab initio* molecular dynamics is also helpful because it can deal with dynamic effects on product selectivity for downhill bifurcations (1). Recently, I proposed an automated search for downhill bifurcations based on a theoretical method called the artificial force induced reaction (AFIR) method (29).

The occurrence of a downhill bifurcation in a PES depends on various perturbations, such as functional group substitution, atom replacement, and mechanical force. For example, Marx et al. used metadynamics simulations under a mechanical force to investigate the ring-opening reaction of cyclopropane derivatives (30). They reported that changing the substituent or applying a mechanical force changes an uphill bifurcation (31), which occurs along the path climbing up from the reactants, to a downhill bifurcation. Investigating the generality of this phenomenon is important for understanding the selectivity of chemical reactions including downhill bifurcations. In particular, it is interesting to examine its occurrence in pericyclic reactions, for which various downhill bifurcations have already been studied. To achieve this, an approach to systematically explore the occurrence of this phenomenon in a PES is required. The metadynamics approach mentioned above is one of the most promising ways to analyze this phenomenon (30,32,33). Here, I propose a more convenient alternative method for evaluating the occurrence of this phenomenon based on the AFIR method and apply it to three model sigmatropic rearrangement reactions.

First, I explain the mechanism of the transition from an uphill bifurcation to a downhill bifurcation. Then, I propose a practical method applicable to actual molecules using a force-modified

PES (FMPES) (34), in which a linear potential is applied to the PES along the reaction coordinate. This method confirms the occurrence of transition from uphill bifurcation to downhill bifurcation by checking the merging of the TSs of the two reaction paths. Application of the proposed method to the three model reactions shows that perturbations can cause downhill bifurcations in some sigmatropic rearrangement reactions.

5.2 Theory

I begin by explaining the mechanism of the transition from an uphill bifurcation to a downhill bifurcation, hereafter called uphill–downhill transition (UDT), using the ideal model potential shown in **Equation (5.1)**.

$$V(x,y) = -\frac{1}{2}\lambda(x - x_0)^2 - \frac{1}{2}c_{xy^2}xy^2. \tag{5.1}$$

This potential consists of two independent terms: the first term defines the shape of the PES along the reaction coordinate x, and the second term defines the shape of the PES along the vibrational coordinate y perpendicular to x. $\lambda > 0.0$ is the force constant along the x-axis and $c_{xy^2} > 0.0$ is the coefficient of the second term. Because $\lambda > 0.0$, the first term represents an upward convex harmonic potential in the x direction with the energy maximum located at $x = x_0$. The second term represents a vibrational mode orthogonal to x with curvature $-c_{xy^2}x$. The sign of $-c_{xy^2}x$ changes from positive to negative at $x = 0.0$, which is the VRT point. The VRT point is located before the energy maximum, meaning that the bifurcation occurs on the way up the reaction path, i.e., an uphill bifurcation (**Figure 5.1**, left). $V'(x, y)$ is the potential obtained by adding a linear potential in the x direction to V, as shown in **Equation (5.2)**.

$$V'(x,y) = V(x,y) - \alpha x = -\frac{1}{2}\lambda\left(x - (x_0 - \frac{\alpha}{\lambda})\right)^2 - \frac{1}{2}c_{xy^2}xy^2 + \frac{\alpha^2}{2\lambda} - \alpha x_0, \quad (5.2)$$

where $\alpha > 0$ is the coefficient of the linear potential. The linear potential is one of the simplest approximate potentials that expresses the application of a constant mechanical force to the molecule or a change in the stability of the reactant relative to the product due to chemical modification. The second term representing the curvature perpendicular to the reaction coordinate is the same as that in **Equation (5.1)**, even if a linear force is applied along the *x*-axis because the linear potential term is orthogonal to the vibrational coordinate. This implies that the linear force does not change the location of the VRT (x = 0.0). In contrast, considering the first term, the location of the energy maximum along the *x*-axis shifts in the reactant direction, which corresponds to Hammond's postulate. If $x_0 - \frac{\alpha}{\lambda} < 0$, the VRT moves down the reaction path, i.e., the uphill bifurcation changes to a downhill bifurcation (**Figure 5.1**, right). In other words, a UDT is caused by a shift in the position of the energy maximum toward the reactant owing to the addition of a linear potential along the reaction coordinate, which corresponds to a constant mechanical force or destabilization of the reactant through substitution of an atom or substituent.

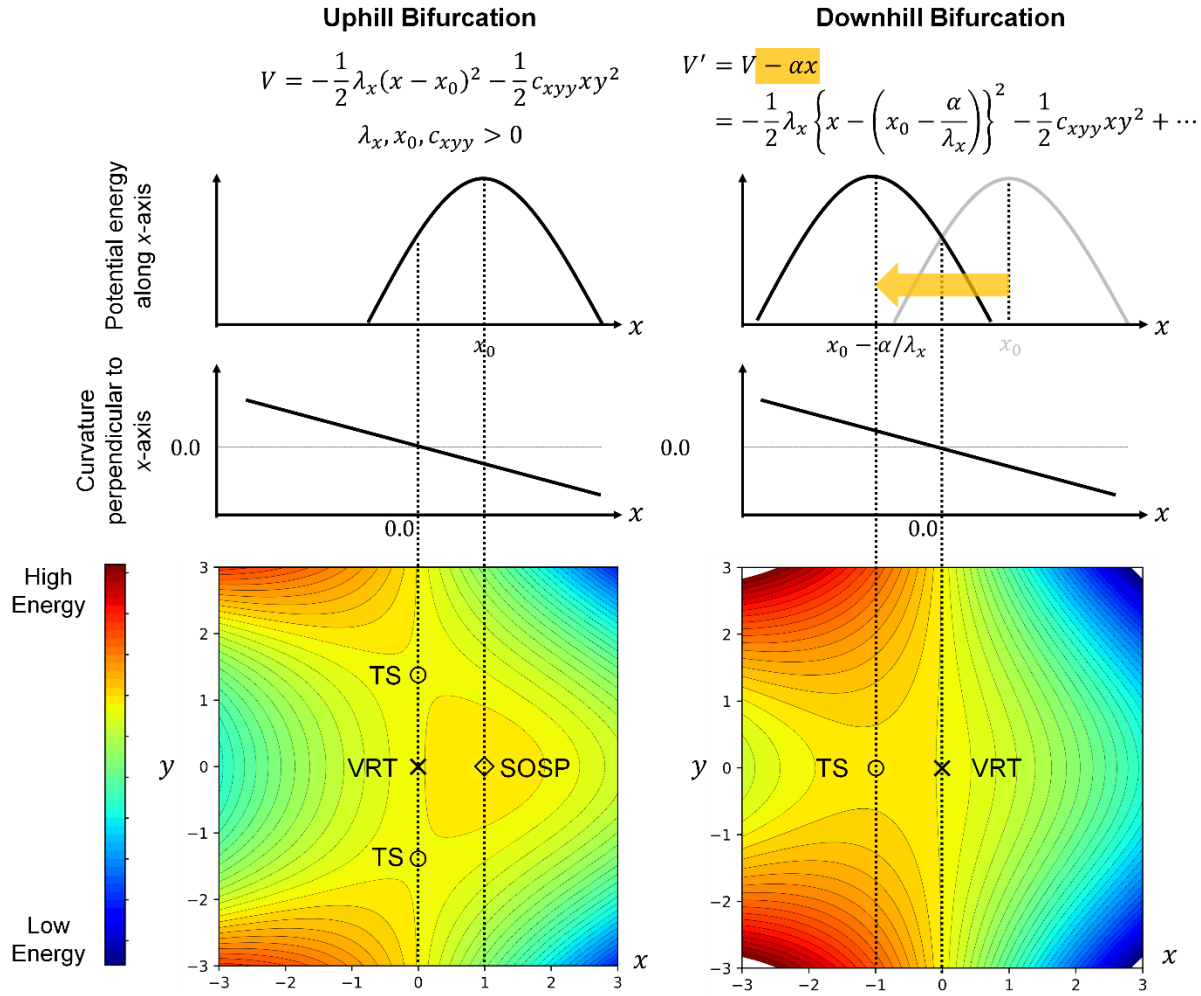

Figure 5.1. Schematic illustration of the uphill–downhill transition (UDT) mechanism. The left and right diagrams show the model potential energy surfaces (PESs) for the uphill and downhill bifurcations, respectively. Transition state (TS) points, valley–ridge transition (VRT) points, and a second-order saddle point (SOSP) are indicated on the 2D PES.

Based on the mechanism above, I propose a method for determining the occurrence of a downhill bifurcation by checking the occurrence of a UDT in two given reaction paths using a FMPES consisting of the original PES term and an additional force term. In this study, the FMPES is

represented by the AFIR function (**Equation (5.3)**), which was originally developed as an automated reaction path search method (35,36).

$$F(\mathbf{Q}) = E(\mathbf{Q}) + \rho\alpha\frac{\sum_{i\in X}\sum_{j\in Y}\omega_{ij}r_{ij}}{\sum_{i\in X}\sum_{j\in Y}\omega_{ij}}. \tag{5.3}$$

$E(\mathbf{Q})$ is the PES of the $3N$ (N is the number of atoms) coordinate $\mathbf{Q}$ of the molecule, r_{ij} is the distance between the i-th and j-th atoms, and X and Y are the fragments to which the artificial force is applied. The second term represents the force that pulls apart or pushes together X and Y. ρ is the sign of the force and is set to either 1 (push) or -1 (pull). ω_{ij} is a weight function defined by

$$\omega_{ij} = \left[\frac{R_i + R_j}{r_{ij}}\right]^6, \tag{5.4}$$

where R_i and R_j are the covalent radii of the i-th and j-th atoms, respectively. A is a parameter representing the strength of the force, defined by

$$\alpha = \frac{\eta}{\left[2^{-\frac{1}{6}} - \left(1 + \sqrt{1 + \frac{\eta}{\epsilon}}\right)^{-\frac{1}{6}}\right]R_0}, \tag{5.5}$$

where R_0 and ε are the Leonard–Jones parameters for Ar–Ar, which are 3.8164 Å and 1.0061 kJ mol^{-1}, respectively. In most of the previous papers (35,36), γ is used to denote the model collision parameter for the AFIR method, which corresponds to the magnitude of the artificial force. However, in this study, γ is a parameter for the reaction path search, and the model collision parameter describing the force for the FMPES is denoted by η. Hereafter, FMPES ($\eta = x$ kJ mol^{-1}) indicates a FMPES with the parameter $\eta = x$ kJ mol^{-1}. Based on the hypothesis above, the proposed method applies an artificial force along the reaction coordinate corresponding to a mechanical force or destabilization of the reactant minimum. The occurrence of a UDT is confirmed by changing η

gradually until the reactant minimum vanishes and investigating whether the two TSs merge. This procedure allows the detection of a perturbation-induced downhill bifurcation in the target molecular skeleton without brute-force calculations for various substituent.

5.3 Computational Details

3.1. Target model reactions

In this study, I searched for downhill bifurcations yielding two [3,3]-sigmatropic rearrangement products (37) because only one downhill bifurcation has been reported for this type of reaction thus far (23). **Figure 5.2** shows the three target model reactions for which there are two possible [3,3]-sigmatropic rearrangements from one reactant based on the reaction formula. The reactants contain a pair of 1,5-hexadiene moieties. The actual experimental activity of these reactants is beyond the scope of this study. In **Reaction-A**, P_{A1} is obtained when C5–C6 bond formation and C1–C2 bond dissociation occur simultaneously,

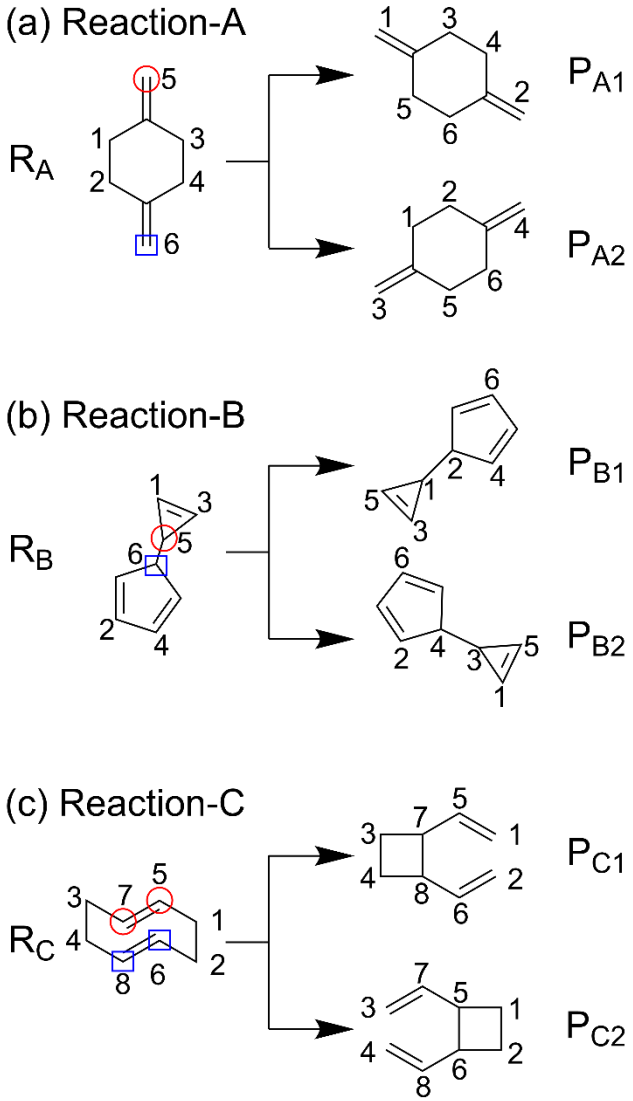

Figure 5.2. Three target reactions with one reactant I and two products (P): (a) **Reaction-A**, (b) **Reaction-B**, and (c) **Reaction-C**. Red circles and blue squares indicate atoms in fragment-X and fragment-Y, respectively.

and P_{A2} is obtained when C5–C6 bond formation and C3–C4 bond dissociation occur simultaneously. In **Reaction-B**, P_{B1} is obtained when C5–C6 bond dissociation and C1–C2 bond formation occur simultaneously, and P_{B2} is obtained when C5–C6 bond dissociation and C3–C4 bond formation occur simultaneously. In **Reaction-C**, P_{C1} is obtained when C7–C8 bond formation and C1–C2 bond

dissociation occur simultaneously, and P_{C2} is obtained when C5–C6 bond formation and C3–C4 bond dissociation occur simultaneously. The two sigmatropic rearrangements have a common bond formation or dissociation step (C5–C6) in **Reaction-A** and **Reaction-B** and none in **Reaction-C**. It should be noted that the downhill bifurcation observed in a previous theoretical study occurred in **Reaction-A** (23).

First, the conformers of the reactants for the three reactions were explored using the single-component (SC)-AFIR method with γ = 100.0 kJ mol^{-1}. Subsequently, the reaction paths (AFIR paths) leading to the two products were explored using the SC-AFIR method with γ = 500.0 kJ mol^{-1} for **Reaction-A** and **Reaction-C** in FMPES (η = 100.0 kJ mol^{-1}) and for **Reaction-B** in FMPES (η = −100.0 kJ mol^{-1}), where a negative η indicates ρ = −1. The obtained AFIR paths were then relaxed in the FMPES without an artificial force, i.e., FMPES (η = 0.0 kJ mol^{-1}) using the locally updated plane (LUP) method until the energy maxima on the paths became TSs. IRC paths were then calculated from the obtained TSs. I further optimized the TSs in FMPESs with different η values by relaxing the LUP path obtained in FMPES (η = 0.0 kJ mol^{-1}). For **Reaction-A** and **Reaction-C**, η was increased by 20 kJ mol^{-1} from −100 kJ mol^{-1} until the reactant minimum vanished. For **Reaction-B**, η was decreased by 20 kJ mol^{-1} from 100 kJ mol^{-1} until the reactant minimum vanished.

Based on the hypothesis that a perturbation along the reaction coordinate causes a UDT, I applied an artificial force to the reaction coordinate common to the two sigmatropic rearrangements. In **Reaction-A**, a bond is formed between C5 and C6 to yield P_{A1} and P_{A2}. Thus, I chose C5 as fragment-X and C6 as fragment-Y (**Figure 5.2**). The same fragments were used for **Reaction-B**

because the bond between C5 and C6 is broken in both reactions to yield P_{B1} and P_{B2}. Because the reactions in **Reaction-C** have no common bond formation or cleavage step, I chose C5 and C7 as fragment-X and C6 and C8 as fragment-Y, which correspond to the bond formation between C5 and C6 and that between C7 and C8.

The semiempirical method GFN2-xTB (38,39) was used only for the initial conformational search, and density functional theory (DFT) at the ωB97X-D (40)/def2-SV(P) level was used for the subsequent calculations. GFN2-xTB energies and gradients were calculated using the ORCA program package (41). DFT energies and gradients were computed using the Gaussian16 program package (42). Optimization of the minima and TSs, LUP, and the SC-AFIR explorations were carried out using a developmental version of the global reaction route mapping (GRRM) program (43).

5.4 Results

5.4.1 Optimized Structures

The optimized structures of the reactant minima (R_A, R_B, and R_C), TSs (TS_{A1}, TS_{A2}, TS_{B1}, TS_{B2}, TS_{C1}, and TS_{C2}), and product minima (P_{A1}, P_{A2}, P_{B1}, P_{B2}, P_{C1}, and P_{C2}) in the FMPES (η = 0.0 kJ mol^{-1}) for the three reactions are shown in **Figure 5.3**. Two different TSs leading to two different products were found for each of the three reactions. In other words, a downhill bifurcation did not occur for the original molecules.

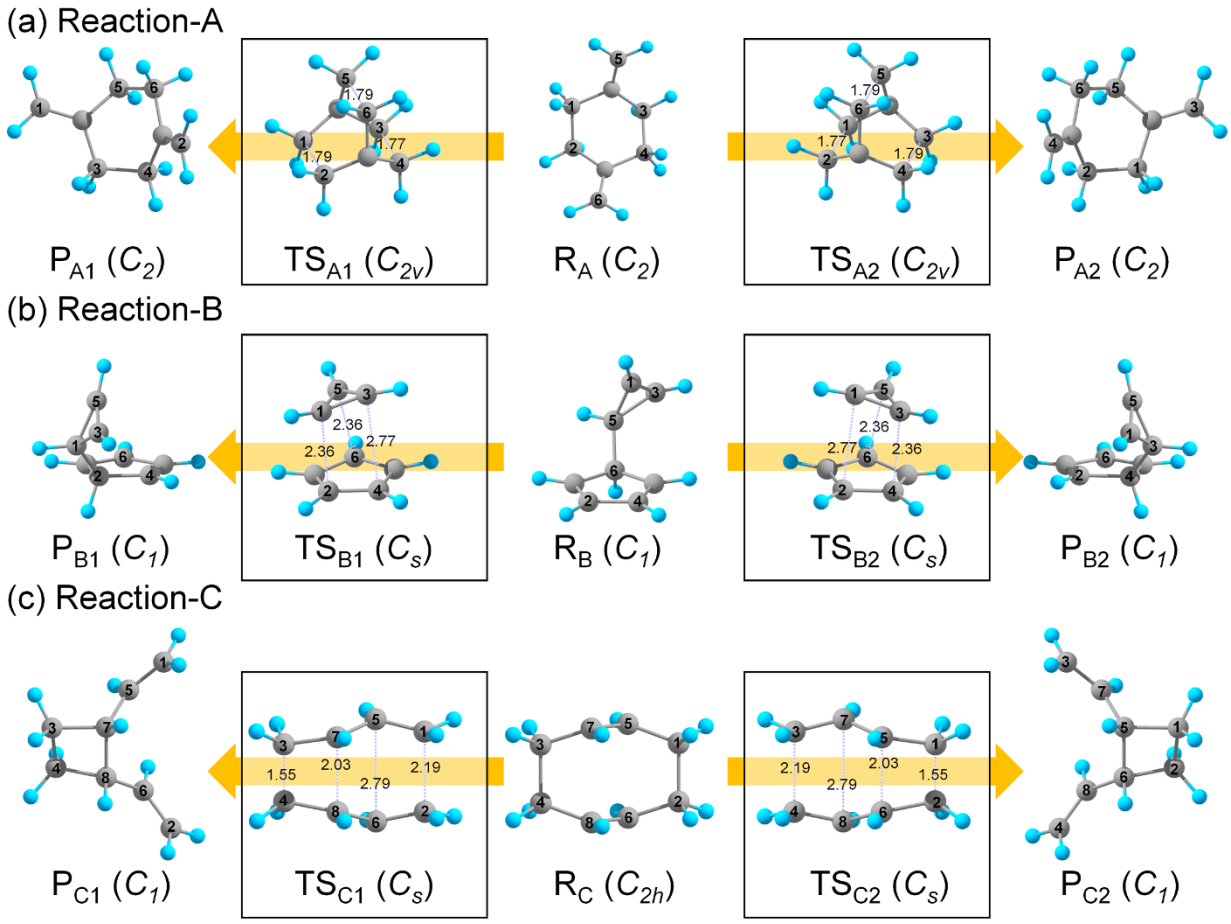

Figure 5.3. Calculated structures of the reactant minima (R_A, R_B, and R_C), transitions states (TSs) (TS_{A1}, TS_{A2}, TS_{B1}, TS_{B2}, TS_{C1}, and TS_{C2}), and product minima (P_{A1}, P_{A2}, P_{B1}, P_{B2}, P_{C1}, and P_{C2}) in the potential energy surface at $\eta = 0.0$ kJ mol^{-1} for (a) **Reaction-A**, (b) **Reaction-B**, and (c) **Reaction-C**. The symmetries of the structures are also shown.

5.4.1 Reaction-A

Figure 5.4 shows the results obtained by applying the proposed method to **Reaction-A**. The variation of two internal coordinates, the distances between C1 and C2 and between C3 and C4, in geometries along the IRC paths from TS_{A1} and TS_{A2} at $\eta = 0.0$ kJ mol^{-1} is shown in **Figure 5.4a**, and that in the TS_{A1} and TS_{A2} geometries at $\eta = -100.0$–120.0 kJ mol^{-1} is shown in **Figure 5.4b**. Because the

reactant minimum R_A disappeared in FMPES (η = 140.0 kJ mol−1), only FMPESs with η up to 120.0 kJ mol^{-1} was considered. **Figure 5.4a** shows that the IRC path from TS_{A1} connects reactant R_A in the lower-left region to product P_{A1} in the lower-right region, whereas the IRC path from TS_{A2} connects reactant R_A to product P_{A2} in the upper-left region. It appears that the two IRC paths initially move from R_A in the same direction, then bifurcate into two different TSs.

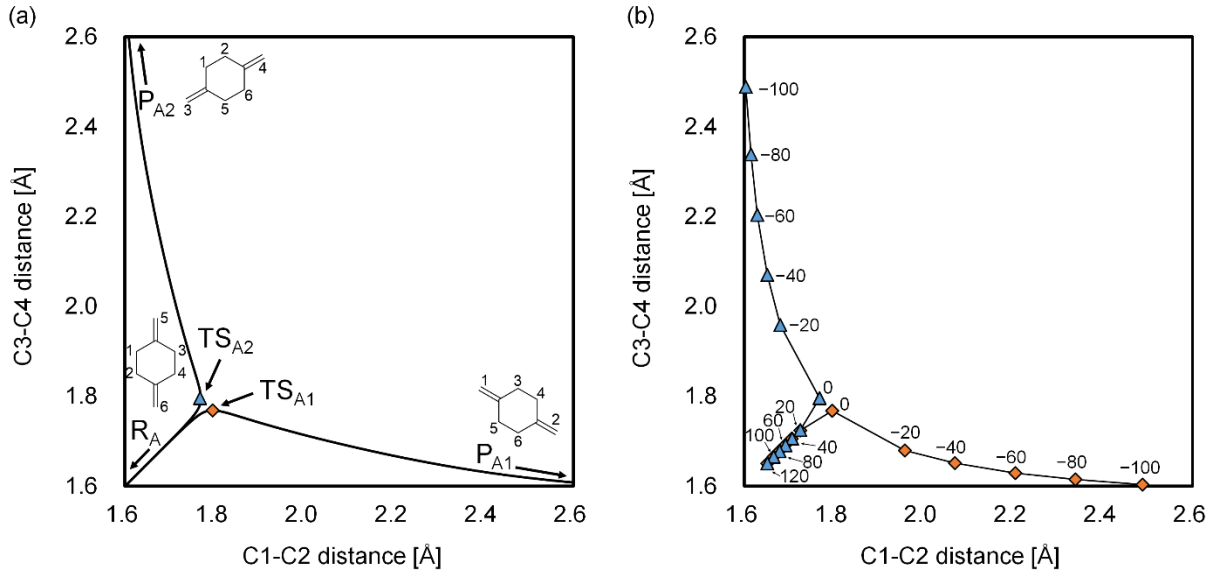

Figure 5.4. Variation of the C1–C2 and C3–C4 distances in (a) geometries along the intrinsic reaction coordinate (IRC) paths from transition states (TSs) TS_{A1} and TS_{A2} in the force-modified potential energy surface (FMPES) (η = 0.0 kJ mol^{-1}) and (b) TS_{A1} and TS_{A2} geometries in FMPES (η = −100.0−120.0 kJ mol^{-1}) of **Reaction-A**. The two pairs of carbon atoms (C1 and C2 and C3 and C4) form bonds along the paths toward products P_{A1} and P_{A2}. In (b), the values of the artificial force η in kJ mol^{-1} are shown, and the orange diamonds and blue triangles indicate TS_{A1} and TS_{A2}, respectively. The black lines in (a) correspond to the IRC paths, while the black line in (b) connects the TSs.

Figure 5.4b shows that the two TSs move to the reactant side (lower-left region) with increasing η and optimize to the same geometry (one ambimodal TS) in FMPESs with η > 20.0 kJ mol^{-1}. This result indicates that a UDT occurs in **Reaction-A** upon application of an artificial force, and the two TSs merge.

Figure 5.5 shows the results of the vibrational analysis along the IRC path from TS_{A1} (which is equal to TS_{A2}) in FMPES (η = 40.0 kJ mol^{-1}) of **Reaction-A**. The variation of the frequencies of the vibrational modes perpendicular to the IRC path are shown in **Figure 5.5a**. One of the frequencies changes from real to imaginary around s = 0.6 Å amu$^{1/2}$, indicating the occurrence of a VRT along the IRC path. **Figure 5.5b** shows the plots of the PES and FMPES (η = 40.0 kJ mol^{-1}) (E(**Q**) and F(**Q**) in **Equation (3)**, respectively) along the IRC path. The energy maxima in the PES and FMPES (η = 40.0 kJ mol^{-1}) are located at s = 1.0 Å and 0.0 Å amu$^{1/2}$, respectively. This indicates that the energy maximum moves along the path from the product side to the reactant side by destabilizing the reactant using an additional force term. This result supports the mechanism underlying the occurrence of a UDT and suggests that the UDT in **Reaction-A** occurs via chemical modification.

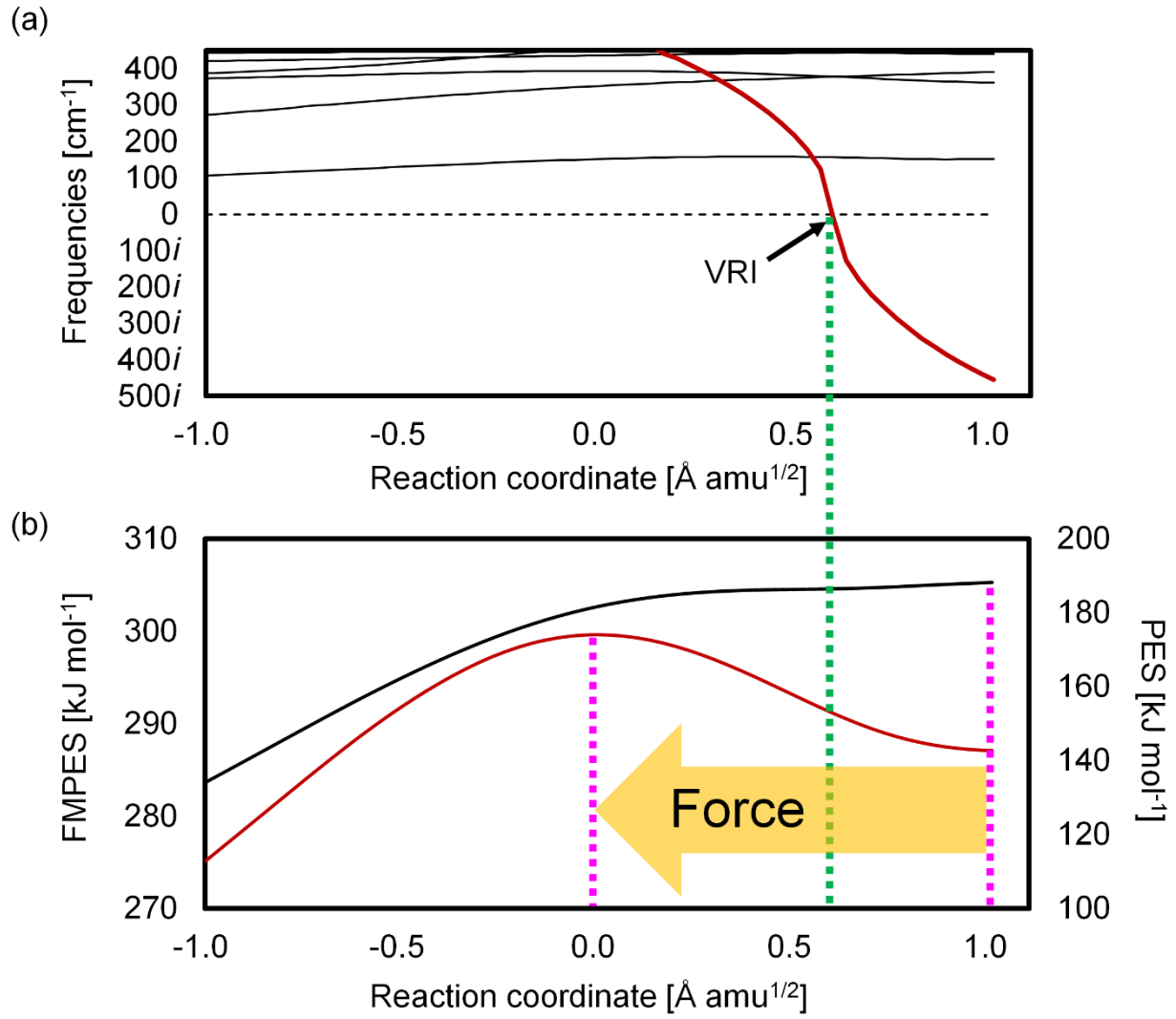

Figure 5.5. Vibrational analysis along the intrinsic reaction coordinate (IRC) path from transition state TS_{A1} (which is equal to TS_{A2}) in the force-modified potential energy surface (FMPES) (η = 40.0 kJ mol^{-1}) of **Reaction-A**. (a) Variation of the frequencies of the vibrational modes orthogonal to the IRC path. The red line indicates the frequency of the mode at which the valley–ridge transition (VRT) occurs, and the black lines indicate the frequencies of the other modes. (b) Plots of the potential energy surface (PES) and FMPES (η = 40.0 kJ mol^{-1}) along the IRC path. The pink dashed lines indicate the positions of the energy maxima, and the green dashed line indicates the position of the

VRT. The coordinate s = 0.0 Å amu$^{1/2}$ corresponds to TS_{A1}. The black and red lines show the energy variations in the PES and FMPES (η = 40.0 kJ mol^{-1}) along the IRC path, respectively.

In a previous study, a downhill bifurcation occurred when one of the methylene groups was substituted with a vinylidene group (23). **Figure 5.6** shows the TS of the substituted system as a red cross overlaid on **Figure 5.4b**. The TS of this substituted system is located in the region where the two TSs merge into one ambimodal TS upon application of an artificial force. The existence of two individual TSs for the unsubstituted system indicates that the previously reported downhill bifurcation is caused by a chemical-substitution-induced UDT.

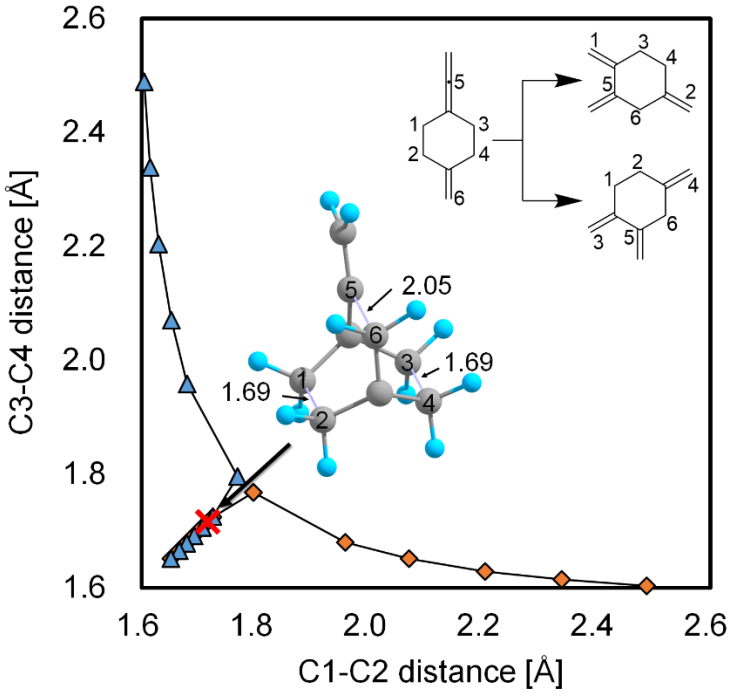

Figure 5.6. Variation of the C1–C2 and C1–C2 distances in the transition state (TS) geometries in the force-modified potential energy surface (FMPES) (η = −100.0–120.0 kJ mol^{-1}). The TS of the substituted system (red cross) is overlaid on **Figure 5.4b**, and its 3D geometry is shown with the atom–atom distances in Å.

5.4.2 Reaction-B

In contrast to **Reaction-A**, **Reaction-B** and **Reaction-C** have not been reported to exhibit a downhill bifurcation. **Figure 5.7** shows the results obtained by applying the proposed procedure to **Reaction-B**. The variation of the C1–C2 and C3–C4 distances in the geometries along the IRC paths from TS_{B1} and TS_{B2} at η = 0.0 kJ mol^{-1} is shown in **Figure 5.7a**, and that in the TS_{A1} and TS_{A2} geometries at $-260.0 \leq \eta \leq 100.0$ kJ mol^{-1} is shown in **Figure 5.7b**. **Figure 5.7a** shows that the IRC path from TS_{B1} connects reactant R_B in the upper-right region to product P_{A1} in the center-left region,

whereas the IRC path from TS_{B2} connects reactant R_B' to product P_{B2} in the lower-center region. R_B' is a conformer of R_B, and its three-membered ring is tilted to the left, in contrast to that of R_B, which is tilted to the right (**Figure 5.3b**). As shown in **Figure 5.7b**, two different TSs exist independently at $\eta \geq -20.0$ kJ mol^{-1}, while only one TS exists at $-240.0 \leq \eta \leq -20.0$ kJ mol^{-1}. This suggests that a UDT also occurs in **Reaction-B** upon decreasing η. However, at $\eta = -260.0$ kJ mol^{-1}, the TS splits into two TSs because there are two reactant conformers, R_B and'R_B'. Thus, a downhill bifurcation occurs on the reactant side, which then transitions to an uphill bifurcation at $\eta = -260.0$ kJ mol^{-1}.

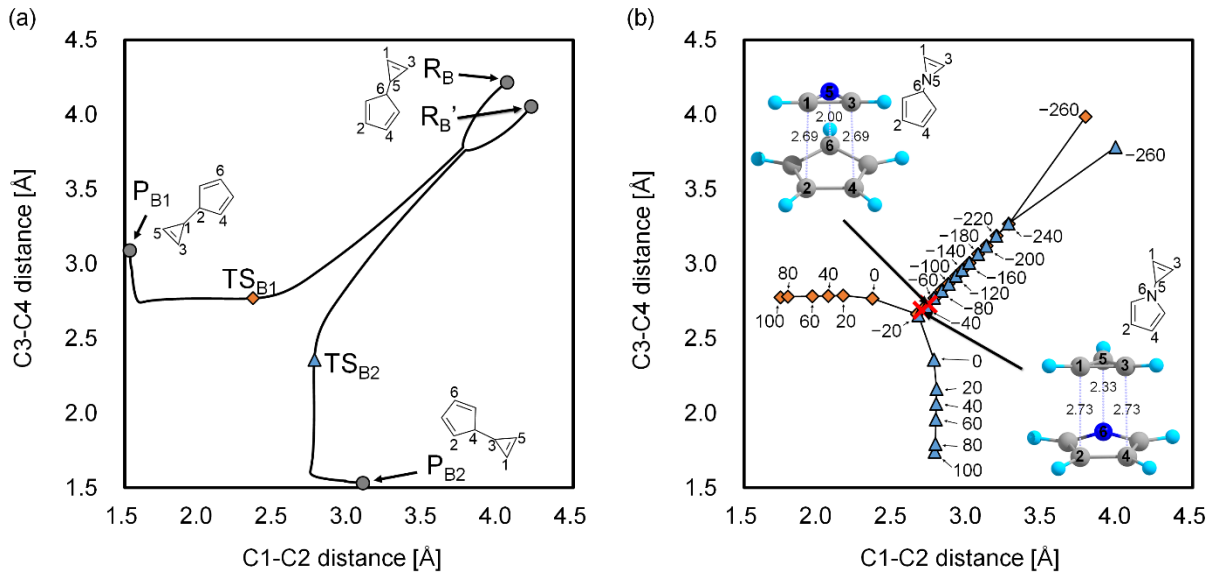

Figure 5.7. Variation of the C1–C2 and C3–C4 distances in (a) geometries along the intrinsic reaction coordinate (IRC) paths from transition states (TSs) TS_{B1} and TS_{B2} in the force-modified potential energy surface (FMPES) (η = 0.0 kJ mol^{-1}) and (b) TS_{B1} and TS_{B2} geometries in FMPES (η = −260.0−100.0 kJ mol^{-1}) of **Reaction-B**. The two pairs of carbon atoms (C1 and C2 and C3and C4) form bonds along the paths toward products P_{B1} and P_{B2}. In (b), the values of the artificial force η in

kJ mol^{-1} are shown, the orange diamonds and blue triangles indicate TS_{B1} and TS_{B2}, respectively, and the red crosses indicate the TSs of the systems in which C5 or C6 is substituted with nitrogen.

Subsequently, I determined the actual chemical modification that caused the downhill bifurcation, which was expected owing to the existence of a UDT. TS optimization was performed for the systems in which C5 or C6 was substituted with nitrogen. Optimization yielded only TSs whose C1–C2 distance was equal to the C3–C4 distance (red crosses in **Figure 5.7b**). This suggests that the UDT occurred because of the destabilization of the reactant relative to the product upon replacement of the C–C bonds with C–N bonds. In other words, a new downhill bifurcation in the [3,3]-sigmatropic rearrangement was found using the proposed strategy based on the UDT. These results verify that a downhill bifurcation system can be designed by investigating the occurrence of a UDT for a given pair of reactions in a molecular skeleton.

5.4.3 Reaction-C

Figure 5.8 shows the results obtained by applying the proposed method to **Reaction-C**. The variation of the C1–C2 and C3-C4 distances in the geometries along the IRC paths from TS_{B1} and TS_{B2} at η = 0.0 kJ mol^{-1} are shown in **Figure 5.8a**, and that in the TS_{A1} and TS_{A2} geometries at $-260.0 \leq \eta \leq 100.0$ kJ mol^{-1} is shown in **Figure 5.8b**. **Figure 5.8a** shows that the IRC from TS_{C1} connects reactant R_C in the lower-left region to product P_{C1} in the lower-right region, whereas the IRC from TS_{C2} connects R_C to product P_{C2} in the upper-left region. Interestingly, **Figure 5.8b** shows

that TS_{C1} and TS_{C2} do not merge when η is increased until R_C disappears. This indicates that there are systems in which a UDT does not occur. For **Reaction-C**, this is likely because the two IRC paths emerge from R_C in different directions, unlike the case in **Reaction-A** and **Reaction-B**, that is, **Reaction-C** does not involve an uphill bifurcation. In the chemical sense, the absence of an uphill bifurcation appears to correspond to the absence of a common bond formation or cleavage step in the two [3,3]-sigmatropic rearrangements. Thus, this result shows that the proposed procedure predicts not only the presence of a downhill bifurcation but also its absence in the target molecular skeleton.

These results show that the proposed method can determine the occurrence of perturbation-induced downhill bifurcations. Thus, the proposed method is expected to become a powerful tool for correctly predicting chemical reaction mechanisms in future chemical reaction design.

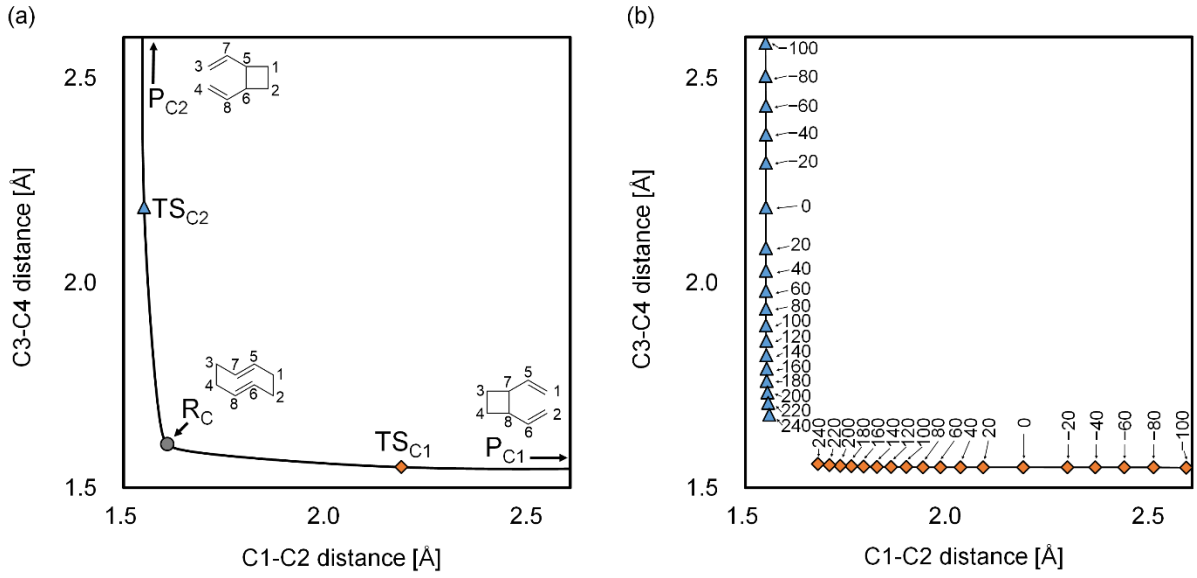

Figure 5.8. Variation of the C1–C2 and C3–C4 distances in (a) geometries along the intrinsic reaction coordinate (IRC) paths from transition states (TSs) TS_{C1} and TS_{C2} in the force-modified potential energy surface (FMPES) (η = 0.0 kJ mol^{-1}) and (b) TS_{C1} and TS_{C2} geometries in FMPES (η = −100.0−120.0 kJ mol^{-1}) of **Reaction-C**. The two pairs of carbon atoms (C1 and C2 and C3and C4) form bonds along the paths toward products P_{C1} and P_{C2}. In (b), the values of the artificial force η in kJ mol^{-1} are shown, and the orange diamonds and blue triangles indicate TS_{C1} and TS_{C2}, respectively.

5.5 Conclusion

In this study, I propose a method for investigating the occurrence of a downhill bifurcation for a given pair of chemical transformations in a molecular skeleton. The proposed method is based on the mechanism by which the addition of a linear potential along a reaction coordinate changes an uphill bifurcation to a downhill bifurcation, that is, a UDT. The method was used to investigate the occurrence of a UDT in three model pericyclic reactions, each of which has two possible [3,3]-sigmatropic rearrangements. TS optimization in a PES without any artificial forces yielded two

different TSs for the two different [3,3]-sigmatropic rearrangements for each reaction. This indicates that these three reactions do not exhibit a downhill bifurcation and cannot be discussed using conventional methods that start with an ambimodal TS search. When an artificial force was applied to the PES of **Reaction-A**, the two TSs merged, indicating the presence of a downhill bifurcation. Vibrational analysis of the IRC path supported my hypothesis regarding the occurrence of a UDT. In addition, the proposed method confirmed the occurrence of a previously reported downhill bifurcation.

The proposed method was then applied to **Reaction-B** and **Reaction-C**, for which no downhill bifurcations have been previously reported. The method revealed the occurrence of a UDT in **Reaction-B**. In addition, I identified the actual chemical modification causing the downhill bifurcation, that is, a new type of downhill bifurcation yielding two [3,3]-sigmatropic rearrangement products. On the other hand, the method showed the absence of a UDT in **Reaction-C**, which was explained by the difference in the directions of the IRC paths of the TSs emerging from the reactant minimum. From the viewpoint of the molecular structure, this appeared to correspond to the absence of a common bond formation or cleavage step in the two sigmatropic rearrangements. These applications demonstrate that downhill bifurcations can be caused by perturbations, even in pericyclic reactions. In the future, the proposed method is expected to be highly useful for mechanistic studies and reaction design.

5.6 Reference

1. Rehbein, J.; Carpenter, B. K. Do We Fully Understand What Controls Chemical Selectivity? *Phys. Chem. Chem. Phys.* **2011**, *13* (47), 20906–20922. https://doi.org/10.1039/c1cp22565k.

2. Ess, D. H.; Wheeler, S. E.; Iafe, R. G.; Xu, L.; Çelebi-Ölçüm, N.; Houk, K. N. Bifurcations on Potential Energy Surfaces of Organic Reactions. *Angew. Chem. Int. Ed. Engl.* **2008**, *47* (40), 7592–7601. https://doi.org/10.1002/anie.200800918.

3. Hare, S. R.; Tantillo, D. J. Post-Transition State Bifurcations Gain Momentum – Current State of the Field, *J. Pure Appl. Chem.* **2017**, *89* (6), 679-698. https://doi.org/10.1515/pac-2017-0104.

4. Pham, H. V.; Houk, K. N. Diels–Alder Reactions of Allene with Benzene and Butadiene: Concerted, Stepwise, and Ambimodal Transition States. *J. Org. Chem.* **2014**, *79* (19), 8968–8976. https://doi.org/10.1021/jo502041f.

5. Houk, K. N.; Xue, X.-S.; Liu, F.; Chen, Y.; Chen, X.; Jamieson, C. Computations on Pericyclic Reactions Reveal the Richness of Ambimodal Transition States and Pericyclases. *Isr. J. Chem.* **2021**, *61*. https://doi.org/10.1002/ijch.202100071.

6. Valtazanos, P.; Ruedenberg, K. Bifurcations and Transition States. *Theoret Chim. Acta* **1986**, *69* (4), 281–307. https://doi.org/10.1007/BF00527705.

7. Taketsugu, T.; Hirano, T. Mechanism of Bifurcation along the Reaction Path: An Application in the Case of Thioformaldehyde. *J. Chem. Phys.* **1993**, *99* (12), 9806–9814. https://doi.org/10.1063/1.465462.

8. Yamataka, H.; Aida, M.; Dupuis, M. One Transition State Leading to Two Product States: Ab Initio Molecular Dynamics Simulations of the Reaction of Formaldehyde Radical Anion and Methyl Chloride. *Chem. Phys. Lett.* **1999**, *300* (5–6), 583–587. https://doi.org/10.1016/S0009-

2614(98)01440-7.

9. Bakken, V.; Danovich, D.; Shaik, S.; Schlegel, H. B.; A Single Transition State Serves Two Mechanisms: An Ab Initio Classical Trajectory Study of the Electron Transfer and Substitution Mechanisms in Reactions of Ketyl Radical Anions with Alkyl Halides. *J. Am. Chem. Soc.* **2001**, *123* (1), 130–134. https://doi.org/10.1021/ja002799k.
10. Singleton, D. A.; Hang, C.; Szymanski, M. J.; Meyer, M. P.; Leach, A. G.; Kuwata, K. T.; Chen, J. S.; Greer, A.; Foote, C. S.; Houk, K. N. Mechanism of Ene Reactions of Singlet Oxygen. A Two-Step No-Intermediate Mechanism. *J. Am. Chem. Soc.* **2003**, *125* (5), 1319–1328. https://doi.org/10.1021/ja027225p.
11. Noey, E. L.; Wang, X.; Houk, K. N. Selective Gold(I)-Catalyzed Formation of Tetracyclic Indolines: A Single Transition Structure and Bifurcations Lead to Multiple Products. *J. Org. Chem.* **2011**, *76* (9), 3477–3483. https://doi.org/10.1021/jo200556f.
12. Bogle, X. S.; Singleton, D. A. Dynamic Origin of the Stereoselectivity of a Nucleophilic Substitution Reaction. *Org. Lett.* **2012**, *14* (10), 2528–2531. https://doi.org/10.1021/ol300817a.
13. Zhang, L.; Wang, Y.; Yao, Z. J.; Wang, S.; Yu, Z. X. Kinetic or Dynamic Control on a Bifurcating Potential Energy Surface? An Experimental and DFT Study of Gold-Catalyzed Ring Expansion and Spirocyclization of 2-Propargyl-β-Tetrahydrocarbolines. *J. Am. Chem. Soc.* **2015**, *137* (41), 13290–13300. https://doi.org/10.1021/jacs.5b05971.
14. Campos, R. B.; Tantillo, D. J. Designing Reactions with Post-Transition-State Bifurcations: Asynchronous Nitrene Insertions into C–C σ Bonds. *Chem* **2019**, *5* (1), 227–236.

https://doi.org/10.1016/j.chempr.2018.10.019.

15. Liu, F.; Chen, Y.; Houk, K. N. Huisgen's 1,3-Dipolar Cycloadditions to Fulvenes Proceed via Ambimodal [6+4]/[4+2] Transition States. *Angew. Chem. Int. Ed. Engl.* **2020**, *59* (30), 12412–12416. https://doi.org/10.1002/anie.202005265.

16. Zou, Y.; Houk, K. N. Mechanisms and Dynamics of Synthetic and Biosynthetic Formation of Delitschiapyrones: Solvent Control of Ambimodal Periselectivity. *J. Am. Chem. Soc.* **2021**, *143* (30), 11734–11740. https://doi.org/10.1021/jacs.1c05293.

17. Hong, Y. J.; Tantillo, D. J. Biosynthetic Consequences of Multiple Sequential Post-Transition-State Bifurcations. *Nat. Chem.* **2014**, *6* (2), 104–111. https://doi.org/10.1038/nchem.1843.

18. Harabuchi, Y.; Ono, Y.; Maeda, S.; Taketsugu, T. Analyses of Bifurcation of Reaction Pathways on a Global Reaction Route Map: A Case Study of Gold Cluster Au_5. *J. Chem. Phys.* **2015**, *143* (1), 014301. https://doi.org/10.1063/1.4923163.

19. Caramella, P.; Quadrelli, P.; Toma, L. An Unexpected Bispericyclic Transition Structure Leading to 4+2 and 2+4 Cycloadducts in the Endo Dimerization of Cyclopentadiene. *J. Am. Chem. Soc.* **2002**, *124* (7), 1130–1131. https://doi.org/10.1021/ja016622h.

20. Ussing, B. R.; Hang, C.; Singleton, D. A. Dynamic Effects on the Periselectivity, Rate, Isotope Effects, and Mechanism of Cycloadditions of Ketenes with Cyclopentadiene. *J. Am. Chem. Soc.* **2006**, *128* (23), 7594–7607. https://doi.org/10.1021/ja0606024.

21. Patel, A.; Chen, Z.; Yang, Z.; Gutiérrez, O.; Liu, H. W.; Houk, K. N.; Singleton, D. A.

Dynamically Complex [6+4] and [4+2] Cycloadditions in the Biosynthesis of Spinosyn A. *J. Am. Chem. Soc.* **2016**, *138* (11), 3631–3634. https://doi.org/10.1021/jacs.6b00017.

22. Yu, P.; Chen, T. Q.; Yang, Z.; He, C. Q.; Patel, A.; Lam, Y. H.; Liu, C. Y.; Houk, K. N. Mechanisms and Origins of Periselectivity of the Ambimodal [6 + 4] Cycloadditions of Tropone to Dimethylfulvene. *J. Am. Chem. Soc.* **2017**, *139* (24), 8251–8258. https://doi.org/10.1021/jacs.7b02966.

23. López, R. V.; Faza, O. N.; López, C. S. Dynamic Effects Responsible for High Selectivity in a [3,3] Sigmatropic Rearrangement Featuring a Bispericyclic Transition State. *J. Org. Chem.* **2017**, 82 (9), 4758–4765. https://doi.org/10.1021/acs.joc.7b00425.

24. Chen, S.; Yu, P.; Houk, K. N. Ambimodal Dipolar/Diels–Alder Cycloaddition Transition States Involving Proton Transfers. *J. Am. Chem. Soc.* **2018**, *140* (51), 18124–18131. https://doi.org/10.1021/jacs.8b11080.

25. Xue, X.; Jamieson, C. S.; Garcia-Borràs, M.; Dong, X.; Yang, X.; Houk, K. N. Ambimodal Trispericyclic Transition State and Dynamic Control of Periselectivity. *J. Am. Chem. Soc.* **2019**, *141* (3), 1217–1221. https://pubs.acs.org/doi/10.1021/jacs.8b12674.

26. Martin-Somer, Ana.; Xue, X.; Jamieson, C. S.; Zou, Y.; Houk, K. N. Computational Design of a Tetrapericyclic Cycloaddition and the Nature of Potential Energy Surfaces with Multiple

Bifurcations. *J. Am. Chem. Soc.* **2023**, *145* (7), 4221–4230. https://doi.org/10.1021/jacs.2c12871.

27. Ito, T.; Maeda, S.; Harabuchi, Y. Kinetic Analysis of a Reaction Path Network Including Ambimodal Transition States: A Case Study of an Intramolecular Diels−Alder Reaction. *J. Chem. Theory Comput.* **2022**, 18, 1663−1671. https://doi.org/10.1021/acs.jctc.1c01297.

28. Maeda, S.; Harabuchi, Y.; Ono, Y.; Taketsugu, T.; Morokuma, K. Intrinsic Reaction Coordinate: Calculation, Bifurcation, and Automated Search. *Int. J. Quantum Chem.* **2015**, 115 (5), 258−269. https://doi.org/10.1002/qua.24757.

29. Ito, T.; Harabuchi, Y.; Maeda, S. AFIR Explorations of Transition States of Extended Unsaturated Systems: Automatic Location of Ambimodal Transition States. *Phys. Chem. Chem. Phys.* **2020**, *22* (25), 13942–13950. https://doi.org/10.1039/D0CP02379E.

30. Wollenhaupt, M.; Schran, Christoph.; Krupička, M.; Marx, D. Force-Induced Catastrophes on Energy Landscapes: Mechanochemical Manipulation of Downhill and Uphill Bifurcations Explains the Ring-Opening Selectivity of Cyclopropanes. *ChemPhysChem*, 2018, **19**, 837–847. https://doi.org/10.1002/cphc.201701209.

31. Baker, J.; Gill, P. M. W. An Algorithm for the Location of Branching Points on Reaction Paths. *J. Comput. Chem.* **1988**, 9 (5), 465–475. https://doi.org/10.1002/jcc.540090505.

32. Qin, Z.; Tremblay, M.; Hong, X.; Yang, Z. J. Entropic Path Sampling: Computational Protocol to Evaluate Entropic Profile along a Reaction Path. *J. Phys. Chem. Lett.* **2021**, 12 (43), 10713–10719. https://doi.org/10.1021/acs.jpclett.1c03116.

33. Nam, J.; Jung, Y. Enhanced Sampling for Free Energy Profiles with Post-Transition-State Bifurcations. *J. Chem. Theory Comput.* **2023**, 19 (10), 2735−2743. https://doi.org/10.1021/acs.jctc.2c01271.

34. Jiang, J.; Kubota, K.; Jin, M.; Wang, Z.; Nakajima, T.; Ito, H.; Gong, J. P.; Maeda, S. Computational Exploration of Polymer Mechanochemistry: Quantitation of Activation Force and Systematic Discovery of Reaction Sites Utilizing Two Forces. 2023, ChemRxiv. 2022. https://doi.org/10.1021/10.26434/chemrxiv-2022-fr09l. (accessed Nov17, 2023).

35. Maeda, S.; Morokuma, K. Communications: A systematic method for locating transition structures of A+B→X type reactions. *J. Chem. Phys.* **2010**, 132, 241102. https://doi.org/10.1063/1.3457903.

36. Maeda, S.; Harabuchi, Y. Exploring paths of chemical transformations in molecular and periodic systems: An approach utilizing force. *Wiley Interdiscip. Rev. Comput. Mol. Sci.* **2021**, 11 (6), e1538. https://doi.org/10.1002/wcms.1538.

37. Cope, A. C.; Hardy, E. M.; The Introduction of Substituted Vinyl Groups. V. A Rearrangement Involving the Migration of an Allyl Group in a Three-Carbon System[1], *J. Am. Chem. Soc.* **1940**, 62 (2), 441–444. https://doi.org/10.1021/ja01859a055.

38. Bannwarth, C.; Caldeweyher, E.; Ehlert, S.; Hansen, A.; Pracht, P.; Seibert, J.; Spicher, S.; Grimme, S. Extended tight-binding quantum chemistry methods. *WIREs Comput. Mol. Sci.* **2021**, *11*, e1493. https://doi.org/10.1002/wcms.1493.

39. Bannwarth, C.; Ehlert, S.; Grimme, S. GFN2-xTB—An Accurate and Broadly Parametrized Self-Consistent Tight-Binding Quantum Chemical Method with Multipole Electrostatics and Density-Dependent Dispersion Contributions. *J. Chem. Theory Comput.* **2019**, 15 (3), 1652–1671. https://doi.org/10.1021/acs.jctc.8b01176.

40. Chai, J. D.; Head-Gordon, M. Long-range corrected hybrid density functionals with damped atom-atom dispersion corrections. *Phys. Chem. Chem. Phys.* **2008**, 10, 6615-6620. https://doi.org/10.1039/B810189B.

41. Neese, F.; Wennmohs, F.; Becker, U.; Riplinger, C. *J. Chem. Phys.* **2020**, 152, 224108. https://doi.org/10.1063/5.0004608.

42. Frisch, M. J.; Trucks, G. W.; Schlegel, H. B.; Scuseria, G. E.; Robb, M. A.; Cheeseman, J. R.; Scalmani, G.; Barone, V.; Petersson, G. A.; Nakatsuji, H.; Li, X.; Caricato, M.; Marenich, A. V.; Bloino, J.; Janesko, B. G.; Gomperts, R.; Mennucci, B.; Hratchian, H. P.; Ortiz, J. V.;

Izmaylov, A. F.; Sonnenberg, J. L.; Williams, Y. D.; Ding F.; Lipparini, F.; Egidi, F.; Goings, J.; Peng, B.; Petrone, A.; Henderson, T.; Ranasinghe, D.; Zakrzewski, V. G.; Gao, J.; Rega, N.; Zheng, G.; Liang, W.; Hada, M.; Ehara, M.; Toyota, K.; Fukuda, R.; Hasegawa, J.; Ishida, M.; Nakajima, T.; Honda, Y.; Kitao, O.; Nakai, H.; Vreven, T.; Throssell, K.; Montgomery Jr., J. A.; Peralta, J. E.; Ogliaro, F.; Bearpark, M. J.; Heyd, J. J.; Brothers, E. N.; Kudin, K. N.; Staroverov, V. N.; Keith, T. A.; Kobayashi, R.; Normand, J.; Raghavachari, K.; Rendell, A. P.; Burant, J. C.; Iyengar, S. S.; Tomasi, J.; Cossi, M.; Millam, J. M.; Klene, M.; Adamo, C.; Cammi, R.; Ochterski, J. W.; Martin, R. L.; Morokuma, K.; Farkas, O.; Foresman, J. B.; Fox, D. J. *Gaussian16 Rev. B.01*; Gaussian, Incorp.: Wallingford, CT, 2016.

43. Maeda, S.; Harabuchi, Y.; Sumiya, Y.; Takagi, M.; Suzuki, K.; Sugiyama, K.; Ono, Y.; Hatanaka, M.; Osada, Y.; Taketsugu, T.; Morokuma, K.; Ohno, K.; *GRRM (A Developmental Version)*; Hokkaido University, 2023.

6. General Conclusion

Through this thesis, I realized a comprehensive theoretical analysis of chemical reactions including dynamical bifurcations by developing an automated dynamical bifurcation search method, a method to perform kinetic analysis on a reaction path network including dynamical bifurcations, and a method to detect the possibility of dynamical bifurcations for a given system.

In **Chapter 2**, a method to search for dynamical bifurcations based on the artificial force induced reaction (AFIR) method was developed. This method judges a set of paths traced by the AFIR paths giving a common transition state (TS) as a dynamical bifurcation. The automated method was applied to a Diels-Alder reaction between 2-vinylfuran and 3-methoxycarbonylcyclopentadienone, and six dynamical bifurcations were successfully explored including the previously reported dynamical bifurcation.

In **Chapter 3**, a method to perform a kinetic analysis for a reaction path network including dynamical bifurcations was proposed. The method performs a kinetic analysis by combining three methods; the automated search method of dynamical bifurcations introduced in **Chapter 2**, the *ab initio* molecular dynamics (AIMD) simulations to compute branching ratios, and a method to compute rate constants including dynamical bifurcations. The method was applied to a rection path network for an intramolecular Diels-Alder reaction giving two products the (4+2) product and (2+2) product. It was found that dynamical bifurcations occurred from two TSs. The AIMD calculations from the two TSs showed that the (4+2) product was major in both of the two dynamical bifurcations. The kinetic simulation on the network considering dynamical bifurcations was performed and it was found

that the effect of dynamical bifurcations was necessary to reproduce the experimental selectivity qualitatively.

In **Chapter 4**, a machine learning model to predict branching ratios using the information of the potential energy surface (PES) was developed. When computing descriptors, four geometries characterizing a dynamical bifurcation; a TS in which the dynamical bifurcation occurs (TS_r), two minima on the PES (MIN_{P1} and MIN_{P2}) for two products P1 and P2, and a TS connecting MIN_{P1} and MIN_{P2} (TS_i), are projected into a two-dimensional space constructed by two imaginary vectors for TS_r and TS_i, and coordinates for them were used as descriptors. The ML model was applied to a kinetic analysis of a reaction path network analyzed in **Chapter 3**, which reproduced the result of the kinetic analysis based on the AIMD calculation. In addition, a scheme to perform an automated search for dynamical bifurcations and computation of branching ratios simultaneously was proposed and applied to a reaction path network for the retrosynthesis of difluoroglycine. It was found that dynamical bifurcations were important even in the network used in the recent experimental reaction design.

In **Chapter 5**, a method to detect dynamical bifurcations caused by perturbations such as mechanical forces or substitutions. At first, the mechanism for the occurrence of dynamical bifurcations by applying perturbations was explained, and a computational method using an artificial force to represent a perturbation was introduced. The method was applied to three model sigmatropic rearrangement reactions, and it was found dynamical bifurcations were caused by the perturbation in two out of the three reactions. It was found that whether dynamical bifurcations occurred or not

depended on the direction of the IRC paths when emerging from the reactant MINs.

In summary, I developed several methods to analyze chemical reactions including dynamical bifurcations. In the future, it is expected that the methods will reveal the importance of dynamical bifurcations in various chemical reactions such as organic reactions, catalytic reactions, and so on.

7. Acknowledgement

All the studies about dynamical bifurcations in my thesis have been conducted under Prof. Satoshi Maeda for six years. He took care of me, sometimes strictly, but carefully. I would like to thank him very much.

Prof. Harabuchi taught me everything about the research life. I would not have been able to complete my research without him. I appreciate his kind support very much.

I would also like to appreciate my peers. Mr. Kazuki Ueda, Mr. Taichi Shomura, Mr. Ryosuke Takeuchi, and Mr. Kota Matsumoto worked with me through the master’s course, and Mr. Hiroaki Okada and Mr. Hitoshi Nabata worked together in the bachelor's, master's, and doctoral courses, and they always encouraged me very much.

I would like to thank my seniors, Dr. Yosuke Sumiya, Dr. Makito Takagi, Dr. Kanami Sugiyama, Mr. Yoshiaki Tsunekawa, Ms. Junko Miyazaki, and Ms. Akari Uetani for kind advices and instruction about the research and basic knowledge of computers.

I would like to thank coworkers in Theoretical Chemistry Laboratory, especially, Mr. Kazuma Sawamoto, Mr. Yusuke Watanabe and Mr. Shinnosuke Sunazaki, who studied with me together under Prof. Harabuchi.

I am thankful to secretaries of TCL, Madoka Kurihara, Machiko Terashima, Homma Takako, Mami Aoki, Kazuhiro Namba, and Yoko Iwatani for kind help of my academic life.

I would like to thank all those involved in my research life.

Finally, I would like to thank my wife Risa Ito for her support in my research life.